ENN Encyclopedia of Nanoscience and Nanotechnology
www.aspbs.com/enn

Nanoindentation Examination of Crystalline Solid Surfaces

R. Nowak,[1,2] F. Yoshida,[2] D. Chrobak,[1,3] K. J. Kurzydlowski,[4] T. Takagi,[5] T. Sasaki[6]

[1]*Nordic Hysitron Laboratory, Faculty of Chemistry and Materials Sciences, Helsinki University of Technology, FI-02015 TKK, Finland*

[2]*Mechanical System Engineering, Hiroshima University, Higashi-Hiroshima 739-8527, Japan*

[3]*Institute of Materials Science, University of Silesia, 40-007 Katowice, Poland*

[4]*Materials Science and Engineering, Warsaw University of Technology, Woloska 141, 02-507 Warszawa, Poland*

[5]*Hiroshima University of Technology, Miyake, Saeki-ku, Hiroshima 731-5193, Japan*

[6]*Co-Creation Laboratory, International Centre for Materials Research, 6-14-9-202 Minami Aoyama, Minato-ku Tokyo 107-0062, Japan*

CONTENTS

1. GENERAL INTRODUCTION

With the recent developments in advanced materials and nanostructures, particularly in those designed for electronics, it is becoming increasingly evident that their successful application will depend not only on their electrical properties, but also on their mechanical characteristics (whose deficiency would lead to long-term reliability problems), as pointed out earlier by Hiraoka [1]. An examination of the mechanical properties of these so-called new materials is not an easy task, since their mass availability for experiments is normally very small, they appear in the form of thin films, multilayer systems, or tiny crystals used as a substrate for such complex structures as large-scale integrated systems (LSIs), laser diodes (LDs), and so on. Moreover, an evaluation of the mechanical properties of new ultrahard coatings (e.g., diamond, nitrides, or ion beam–modified surfaces) has become nowadays an issue of great importance, owing to the wide application of thin solid films in modern technologies. The indentation test appears naturally to be an invaluable and unique method for examining all these materials, as it requires a small volume of the solid and probes the surface layers of particular interest.

Hundred years ago, the hardness test was first considered the simplest and fastest technique for characterizing the mechanical properties of solids. Various standard hardness tests (see Table 1, for details refer to [2, 3]) have been extensively used to estimate the plastic properties of metals.

The physical significance of the hardness value is in the simple relationship between hardness and the yield stress σ_Y in ideally plastic solids. The Meyer hardness H, being equal to pressure p over a fully plastic indentation, is defined as the indentation load P_{max} divided by the projected area A_p of the indentation mark (for a spherical impression with a diameter size equal to d: $A_p = \pi d^2/4$):

$$H = \frac{P_{max}}{A_p} = \frac{4P_{max}}{\pi d^2} \tag{1.1}$$

ISBN: X-XXXXX-XXX-X

Encyclopedia of Nanoscience and Nanotechnology
Edited by H. S. Nalwa
Volume X: Pages (1–62)

Table 1. Static indentation tests.

Commercial name of the method	Nominal load (kgf)	Indenter	Hardness formula*
Brinell hardness test	500–3000	Spherical, steel	$H = \frac{2P}{\pi D\left[D - \left(D^2 - d^2\right)^{1/2}\right]}$
Vickers hardness test	Less than 120	Diamond pyramid with a square base (apex angle 136°)	$H_V = \frac{2P}{d^2} \cdot \sin\frac{\Theta}{2} = 1.8544 \cdot \frac{P}{d^2}$
Rockwell hardness test	Less than 150	Diamond cone with a spherical tip	$H = \frac{4P}{\pi d^2}$
Berkovich test (microhardness)	0.005–3	Diamond pyramid with a triangular base (angle between the vertical axis and the facet 65°)	$H = \frac{1570 \cdot P}{l^2}$
Knoop test (microhardness)	0.005–3	Diamond pyramid with a square base	$H_K = \frac{P}{7 \cdot 028 \times 10^{-3} \cdot d_1^2}$

* P, D, d, d_1, and l define applied load, sphere diameter, diameter of the impression, the lengths of the long diagonal of the indent, and the perpendicular distance from a corner to the opposite base of the triangular impression, respectively.

The $H-\sigma_Y$ dependence was discovered as early as 1948 by Tabor [4, 5], based on empirical results, while in 1989 theoretical work (finite element method (FEM) calculations) by Hill et al. [6], and Storåkers and Larsson [7] confirmed "Tabor's relationship," which reads:

$$H = p \approx 3\sigma_Y \quad . \tag{1.2}$$

Although the idea of Tabor [eqn (1.2)] in all its simplicity is still valid for metals, it does not hold for most ceramic materials, which are normally hard and brittle and exhibit considerable elastic recovery during indentation unloading. Further, the initiation of cracks during the indentation process performed either with sharp and blunt indenters compromises the measurements and makes it difficult to provide an accurate estimation of hardness of ceramics. This resulted in the development of microhardness testers with maximum indentation load range from 50 mN to 30 N (refer to Table 1).

However, conventional hardness measurement is often insufficient for estimating the plastic properties in the near-surface region, because of its limited accuracy, particularly for the ultralow load interval. This is owing to the limitations in the resolution and efficiency of the optical systems attached to the hardness testers of conventional type. Indeed, one can find it very difficult to measure small-size residual impressions, with a diameter of a few micrometers and less, by means of an optical microscope. Normally, the low-load hardness data exhibit significant scattering with a serious error. The results of measurements of hardness anisotropy of the $(10\bar{1}0)$ plane of sapphire (Fig. 1) serve as an example of the inefficiency of conventional low-load hardness test [8]; the anisotropy registered for the maximum indentation load of 2 N remains undetected if load P_{max} of 500 mN is used.

Further developments of the testing equipment enabled the users to monitor continuously the load experienced by the indenter during the indentation process and the depth of penetration. This not only made it possible to overcome the limitations of

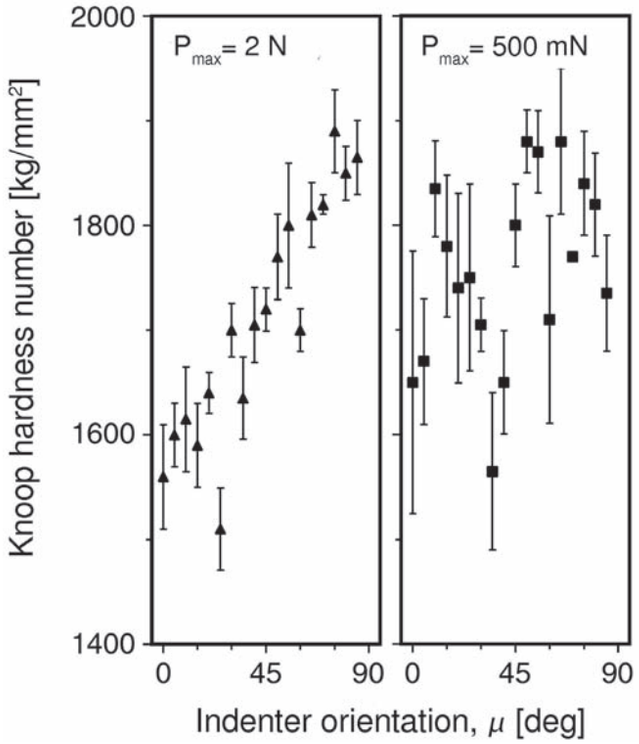

Figure 1. Hardness of the $(10\bar{1}0)$ plane of sapphire measured for various orientations of the Knoop indenter. The position of the penetrator was determined by the angle μ between its long diagonal and the $(1\bar{2}10)$ direction.

the optical system (the measurement of the size of an impression), but also allowed the researchers to derive new information on the complex mechanical behavior of materials deformed in a very shallow surface region. Thus, the depth-sensing indentation technique appears to be a unique method for studying the mechanical properties of solids close to their surfaces, and consequently is very useful for nanostructured materials.

The idea of depth-sensing indentation measurements, which allows the estimation of Young's modulus of tested materials, was first realized more than two decades ago [9, 10], while the first nanoindentation testers were designed 10 years later [11–13]. Furthermore, the pioneering results of nanoindentation tests reported by Pethica et al. [12] resulted in a rapid development of the new research area, the surface deformation of solids.

Certain examples of depth-sensing indentation early studies include in situ observations of the nucleation and propagation of indentation cracks in ceramics, together with the ability to measure the indentation load vs. depth curves [14, 15], application of the nanoindentation method to measurements of residual stress [16] and adhesion [17] of surface coatings, determination of Young's modulus and hardness of high-temperature superconductors [18], research of the electrical resistance of metallic contacts on semiconductors during phase transformation [19–23], observations of structural changes in nanoindented sapphire by means of electron microscopy [24–27] and Raman spectroscopy [28], and studies of deformation and fracture of ion-implanted ceramics [8, 29–32].

It is worth noting that these experiments achieved a "new level," owing to the concentration on the phenomena available for study because of the recent developments in research equipment. This has stimulated an urgent need for a general theory of indentation-induced deformation and fracture (particularly concerning hard brittle materials as well as thin films), which would yield a sound basis for interpreting various types of experimental results. Considerable effort has already been expended on analyzing data from depth-sensing tests and relating them to the observed phenomena [12, 33–35]. Unfortunately, all the above-mentioned approaches were deduced from conventional methods, and were thus based on previous experiments. Taking the residual plastic indentation depth remaining after indentation unloading as an example, the linear extrapolation of the upper part of the unloading curve in order to estimate the "true value of plastic indentation depth" proposed by Doerner and Nix [33] seems a somewhat approximate approach that has been criticized by Oliver and Pharr [36]. The latter provided a comprehensive analysis, while still using the contact area function that prevailed in conventional indentation science results nowadays in serious confusion [37, 38] owing to the widespread application of this method in virtually all the existing nanoindentation equipment.

Significant progress has been achieved in this area through numerical modeling based on the FEM [39, 40]. However, the critical issue of this approach lies in the formulation of the pertinent constitutive equations (a kind of elastic or pseudo-elastic approximation is normally applied) as well in the analysis of contact mechanics. The weakness of these approaches lies in the difficulty in estimating the elastic–plastic stress state near the contact zone. The only case solved analytically is the pure elastic contact of spherical (Hertzian indentation [41]) and axisymmetric sharp indenters (cone indentation: the Boussinesq stress field [42]).

With the ongoing development of nanoindentation equipment toward ultralow loads and high-measurement accuracy that reached recently 0.2 nm of vertical-depth resolution [43], the atomistic simulations became essential in interpretation of the nanoindentation data [22, 44–46] which will be shown in this review that presents the development of this specific field of research in its chronological order.

2. GENERAL REMARKS ON EXISTING MODELS AND CONVENTIONAL ANALYSES OF DEPTH-SENSING INDENTATION DATA

The recently developed nanoindentation technique (the maximum indentation load P_{max} of less than 100 mN, while recently the nanoindentation term is used for P_{max} <10 mN) allows one to determine the mechanical properties of materials on a very small scale and serves as a powerful tool for the mechanical characterization of thin films and solid surface layers. Among the routinely measured parameters are still traditionally hardness and elastic modulus. However, there are a number of alternative indentation techniques which enable one to draw conclusions about the strain rate sensitivity, submicron fracture behavior, or even thermally activated plastic flow (see, e.g. [47]).

Indentation methods and the associated theoretical analyses may be broadly classified according to the shape of the indenter used in experiments. Sharp indenters such as the Berkovich pyramid are frequently used to assess mechanical properties in the smallest possible region [47], while spherically tipped indenters allow one to obtain a complete quantification of elastic–plastic properties, particularly for brittle solids [48]. However, the contact area typical for nanoindentation experiments is very small, so that even the sharpest tip with a radius smaller than 100 nm should be considered blunt or rounded [43].

2.1. Determination of Elastic Modulus

2.1.1. The Analysis of Indentation Data Based on the Theory of a Punch Contact

Depth-sensing indentation allows one to register indentation load and depth as a function of time. Typical examples of load–displacement data obtained in the experiments are shown in Figure 2. They refer to metallic and ceramic crystalline materials, namely, zinc (Fig. 2(a)) and sapphire (Fig. 2(b)). Since the Hertzian theory [41] of contact between two nonrigid bodies yields the following relationship between their Young's moduli (E_1, E_2) and Poisson ratios (ν_1, ν_2):

$$\frac{1}{E_{eff}} = \frac{1-\nu_1^2}{E_1} + \frac{1-\nu_2^2}{E_2} \tag{2.1}$$

where E_{eff} is the effective elastic modulus which may be determined by means of load–depth indentation results (to be precise, from the unloading part of the curve, see Fig. 2,

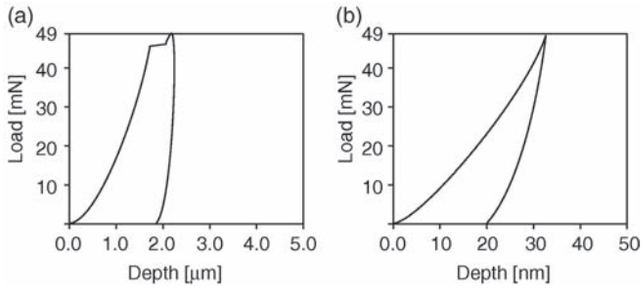

Figure 2. Typical load–displacement curves registered with moderately loaded Berkovich indenter penetrating into the basal plane of zinc (a) and sapphire (b) crystals.

one is able to determine the elastic modulus of the tested solid E_1). Although eqn (2.1) was derived for a spherical indenter, it can similarly be applied to sharp tips for reasons described in the preceding section.

The penetration of a sharp indenter into a solid surface inevitably involves elastic and plastic deformation followed frequently by cracking of the investigated material, which makes it difficult to model the indentation process and analyze the experimental data. Since an analytical solution of the elastic–plastic contact problem is not available [42], and the elastic contact between axisymmetric punches and isotropic and anisotropic halfspaces has been the subject of thorough theoretical investigations (see, e.g. [49–51]), most researchers assume that the solution obtained for elastic punch contact is suitable for modeling elastic–plastic surface deformation. Consequently, the existing approaches are normally based on the Boussinesq solution of 1885 [52, 53] (a linearly elastic Boussinesq problem is to find the solution to linearized equations for an elastically isotropic halfspace under a point load of magnitude P perpendicular to the boundary (see [50])) or on its modification proposed by Sneddon for punches of axisymmetric profile [54]. The latter approach allowed the author to draw conclusions about the shape of the elastically deformed surface and stress distribution under a loaded punch.

Further, the experimental work of Bulychew et al. [55] proved that the relationship between stiffness S, effective elastic modulus E_{eff}, and the projected area of the contact A:

$$S = \frac{dP}{dh} = \frac{2}{\sqrt{\pi}} E_{sff} \sqrt{A} \tag{2.2}$$

which was derived originally for elastic contact of a conical indenter, equally holds for cylindrical, conical, and spherical tips. The validity of eqn (2.2), for all indenter shapes being a body of revolution of smooth function was proved by King [56], who provided elastic analyses for punches of various shapes using the integral equations method (see also [34]).

Based on these pioneering considerations, Oliver and Pharr [36] proposed their method of analysis of sharp indentation data. The authors assumed entirely elastic deformation to occur during the unloading cycle of the penetration process, which enabled them to employ the relationships derived for elastic contact of axisymmetric punch to a case of sharp indentation. They additionally took advantage of earlier work carried out by Doerner and Nix [33], and Loubet et al. [57]. The analysis of indentation data performed by Oliver and Pharr [36] seems to be the most widely used method nowadays, while it is coming quite recently under serious criticism when applied in nanodeformation region [37, 38, 58].

2.1.2. The Conventional Approach by Doerner–Nix and the Classical Oliver–Pharr Model

The approaches of Doerner and Nix [33] or Oliver and Pharr [34, 36] are based on the analysis of data recorded during the unloading cycle of an indentation experiment. Consequently, these procedures disregard the information registered while loading the indenter, which recently created confusion in nanoindentation database [38, 58]. The methods are based essentially on the assumption that a considerable part of the unloading $P-h$ curve possesses a linear character, which suggests that plastic deformation of the material does not occur when unloading. Furthermore, the authors believed that elastic modulus of the tested sample does not change with the indentation depth making it possible to apply Sneddon's solution to the unloading process, that is, the solution for the elastic punch contact proposed by Sneddon [54]. Thus, eqns (2.1) and (2.2) derived for axisymmetric punch problem hold for the unloading part of $P-h$ curve obtained by sharp indentation.

The assumptions made by Doerner and Nix [33], followed by those of Pharr and Oliver [36], have physical meaning, and cause discrepancies between the results of the proposed analysis and experimentally determined values. The crucial point of the approach lies in the assumption that the linearity of an unloading curve points toward a constant contact area, which remains unchanged during the indentation cycle. This seems to be appropriate for metals, essentially plastic materials (see, e.g. [12]), in contrast to solids with a high value of hardness to the modulus ratio H/E, that is, most ceramic materials, which exhibit significant elastic recovery within the contact zone. Hence, the essence of the discussed approach lies in the assumption that elastic recovery occurs exclusively outside the contact with an indenter, as opposed to plastic flow, which is thought to be restricted to the contact region.

Doerner and Nix [33] argue that the final residual indentation depth h_r (see Fig. 3) is affected by elastic recovery within the contact and it should not be used to determine the contact area. Furthermore, in order to estimate the size of the plastic contact region and to determine the residual plastic depth of indentation h_p, they suggest subtraction of elastic contribution from the maximum indentation depth $h_{\max}$:

$$h_p = h_{\max} - \frac{P_{\max}}{S}, \tag{2.3}$$

where S stands for the original slope of the unloading cycle ($S = \mathrm{d}P/\mathrm{d}h$), while $P_{\max}$ defines the maximum indentation load. According to Doerner and Nix [33], the above-mentioned operation (subtraction) may be accomplished geometrically by linear extrapolation of one third of the unloading curve to zero

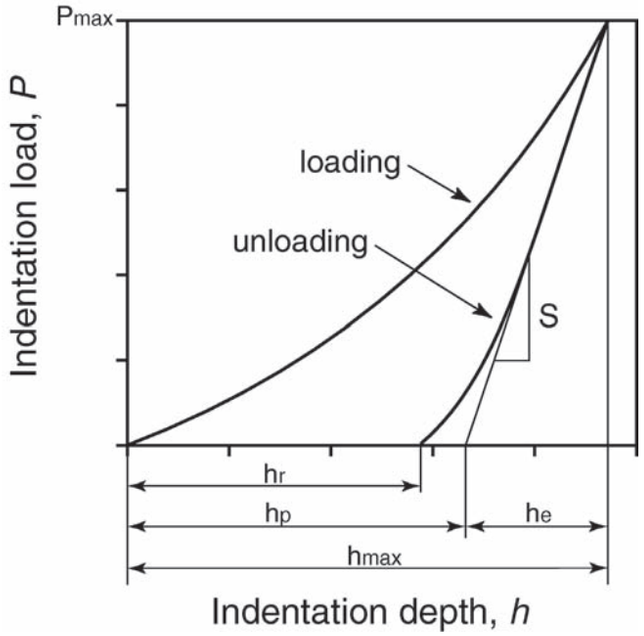

Figure 3. Schematic of the indentation load–displacement curve with the parameters used in the Doerner and Nix analysis [33].

load (refer to Fig. 3). Consequently, the elastically recovered depth can be obtained from eqn (2.3), which yields:

$$h_e = h_{\max} - h_p = \frac{P_{\max}}{S}, \tag{2.4}$$

while elastic modulus of the examined solid E_1 [eqn (2.1)] may be obtained by combining eqns (2.1), (2.2), and (2.3), which consequently provides:

$$\frac{1-\nu_1^2}{E_1} = \frac{1}{E_{eff}} - \frac{1-\nu_2^2}{E_2} = \frac{2}{S\sqrt{\pi}}\sqrt{A} - \frac{1-\nu_2^2}{E_2}, \tag{2.5}$$

where the contact area A may be estimated from the indentation plastic depth [eqn (2.3)].

The Oliver–Pharr analysis of depth-sensing indentation is based on the approximation of the unloading curve by a power-law relationship [34, 36]. The key parameters used in their method comprise initial stiffness S, the maximum load $P_{\max}$, and the maximum penetration depth $h_{\max}$. The authors found that the load–displacement dependence derived by Sneddon for perfectly elastic contact [54] leads to the relationship:

$$P = \alpha h^m, \tag{2.6}$$

where α is constant and m takes values between 1 and 2 for various indenter shapes (for example, when a flat punch is considered $m = 1$, and in the case of the rotated parabola tip profile, $m = 2$). Taking into account the plastic deformation that occurs prior to the elastic unloading, Oliver and Pharr [36] conclude that the unloading curve should fit the power-law relation:

$$P = B\left(h - h_f\right)^m, \tag{2.7}$$

where h_f is the residual displacement after complete unloading determined by the curve fitting with B and m values used as fitting parameters.

In order to calculate the contact depth h_c (refer to Fig. 4), the authors exploited the dependence of h_c on the tip shape, taking advantage of the ε-coefficient from the Sneddon theory of the elastic punch contact problem [54]. Moreover, Oliver and Pharr found that the depth h_c (Fig. 4) appears to be dependent on the initial unloading slope S as well as the maximum displacement exercised by the sharp indenter $h_{\max}$ [36], which yields the simple relationship for the h_c parameter:

$$h_c = h_{\max} - \varepsilon\frac{P_{\max}}{S}, \tag{2.8}$$

where ε equals 1, 0.75, and 0.73 for a flat punch, the Berkovich tip, and the cone-shaped indenter, respectively. The differentiation of the eqn (2.7) allowed Oliver and Pharr to determine the stiffness S at maximum penetration depth:

$$S = \frac{dP}{dh}\Big|_{h=h_{\max}} = B\left(h_{\max} - h_f\right)^{m-1}. \tag{2.9}$$

The principal focus of the Oliver and Pharr analysis [36] is the evaluation of the shape function $A = f(dc)$, which defines the shape of the indenter through the relationship between the projected contact area A and its distance d_c from the indenter tip. In order to conclude on hardness, it is necessary to determine the value of f function at the contact

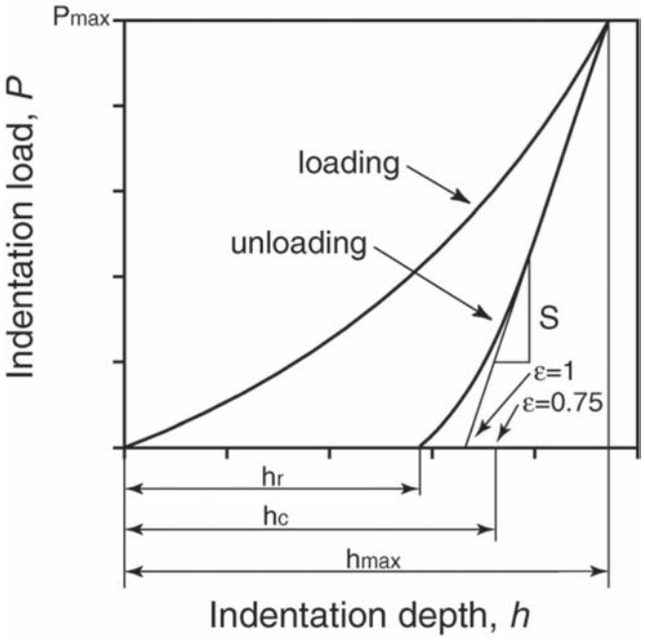

Figure 4. Schematic of the indentation load–displacement curve with the parameters used in the Oliver and Pharr analysis [36].

depth h_c. Therefore, Oliver and Pharr developed a simple empirical calibration procedure that resolves accurately the f function, despite avoiding the imaging of indents. It requires, however, that the $P-h$ data are obtained for a model specimen (normally fused quartz). Furthermore, Oliver and Pharr [36] determined the contact area A using eqn (2.2) and assumed Young's modulus to be independent of indentation depth. Therefore, they estimated the value of effective elastic modulus Eeff:,

$$E_{eff} = \frac{\sqrt{\pi}}{2\beta}\frac{S}{\sqrt{A}}, \tag{2.10}$$

where β depends on the geometry of the indenter and equals 1.034 for the Berkovich tip.

The results of the measurement of Young's modulus of glass and metals according to the method proposed by Oliver and Pharr [36] accord with the conventionally determined values of elastic constants. However, the estimation of elastic modulus of highly anisotropic materials, for example, sapphire or silicon wafers that the method provides – appears to be less accurate or simply erroneous [38, 58].

2.1.3. Stepwise Indentation with Partial Unloading of a Spherical Indenter

An alternative measurement of Young's modulus was proposed by Field and Swain [59–61], who used a spherically tipped indenter for a stepwise indentation with multiple partial unloading. This is expected to produce a well-defined and regular stress field approximating to deformed solid surface [59–66] in contrast to the sharp tips [67], as advocated by Swain and coworkers in their numerous reports. The authors argue that, in the case of spherically tipped indenters, (i) the initial penetration at contact is better estimated, (ii) the radius of the tip may be selected to control the depth of penetration in a particular material, and (iii) the use of such a penetrator enables one to follow the transition from elastic to elastic–plastic response of the indented solid. Moreover, the indentation with multiple partial unloading allowed Field and Swain [59–61] to separate the elastic and plastic components of indentation (Fig. 5), and as a consequence, to estimate the elastic modulus at each step of the penetration process.

In order to achieve the main goal, that is, to evaluate effective elastic modulus, Field and Swain analyzed the geometry of the contact between an elastic rigid sphere (the model of a spherical indenter) and the surface of an elastic and elastic–plastic half-space (the model probed material), during an elastic unloading cycle [60, 61] – as illustrated in Figure 6. They took advantage of the basic relationship between the force P and the depth of elastic penetration of a spherical indenter δ (see Fig. 6(a)), derived originally by Hertz [41] and recently reviewed by Johnson [42]:

$$\delta = \left(\frac{3P}{4E_{eff}\sqrt{R}}\right)^{\frac{2}{3}}, \tag{2.11}$$

where an effective Young's modulus E_{eff} is defined by eqn (2.1), and R stands for the radius of the spherical tip. Further, Field and Swain used the simple formula that holds for shallow spherical indentations with a contact radius of a [42]:

$$\delta = \frac{a^2}{R}, \tag{2.12}$$

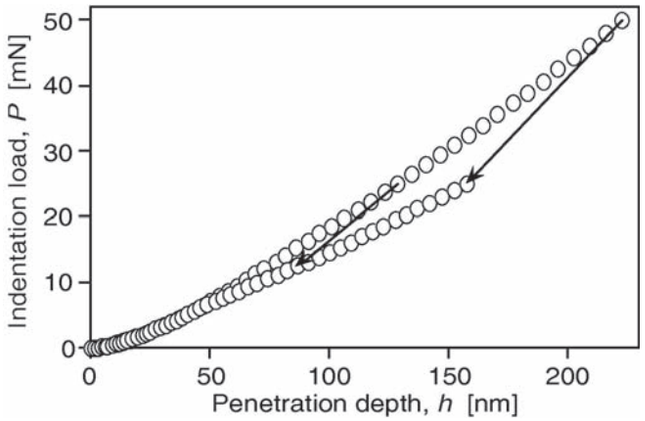

Figure 5. Typical load–partial unload force–displacement data obtained for an elastic–plastic material (data for GaN crystal [196]). Reprinted with permission from [196], R. Nowak et al., *Appl. Phys. Lett.* 75, 2070 (1999). © 1999, American Institute of Physics.

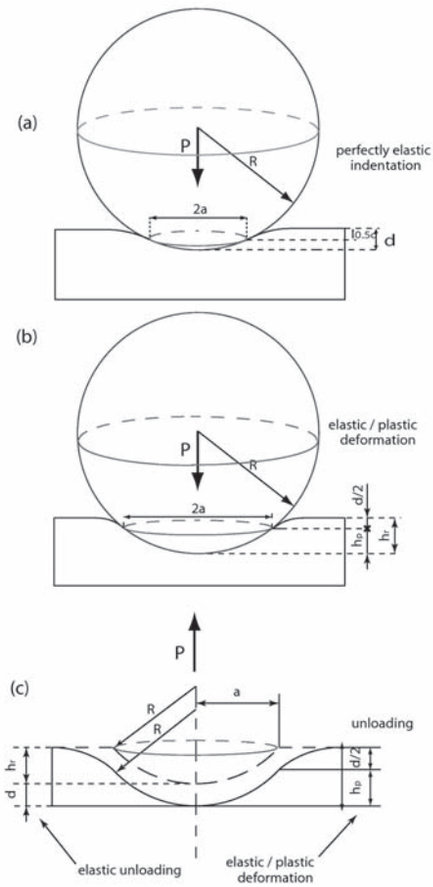

Figure 6. The geometry of penetration of spherical indenter with the radius R into an infinite solid surface being a target of the analysis by Field and Swain [60, 61] for perfectly elastic contact (a), elastic–plastic deformation (b), and elastic unloading process (c).

which provided them with a near-continuous assessment of the effective Young's modulus E_{eff} with the depth of penetration [60]. Such a result was obtained from application of stepwise indentation with partial unloading, in which the E_{eff} value is readily obtained from the simple relationship:

$$E_{eff} = \frac{0.75P}{a(h_t - h_r)}, \tag{2.13}$$

where $h_t - h_r$ denotes the elastic depth recovery (refer to Figs. 6(a) and 6(b)). It is worth emphasizing that the procedure proposed by Field and Swain [60] allows one to determine the E_{eff} value, when one defines merely two different points in the partial unloading curve, sufficient to evaluate the residual indentation depth h_r.

The indentation with a partial unloading enables separation of the elastic and plastic components of the indentation deformation at each loading–unloading cycle. This is of great significance for the application of the method, since it appears to be essential for extracting information relating to material properties [61]. The elastic component is obtained by measuring the recovery, as the indenter is already unloaded. Thus, stepwise indentation with a spherical tip facilitates the quasi-continuous measurement of the changes in the effective elastic modulus E_{eff} for various penetration depths. The approach of Oliver and Pharr [36] discussed in the previous section was modified in such a way as to make it possible to monitor variations of Young's modulus with indenter displacement [47], while it was recently found to be incorrect for determination of Young's modulus in a case of nanoscale deformation [38].

2.1.4. Other Methods for Determining the Elastic Modulus

The determination of the elastic modulus by indentation experiments has frequently been addressed in the literature since 1881, when Hertz discovered the relationship [eqns (2.1) and (2.11)] between Young's modulus and the geometry of the solids that remain in elastic contact [41]. The methods of Oliver and Pharr [36, 47] or Field and Swain [48, 60], however, are widely quoted since they are included in the software package of the commercially available indentation testers (Oliver and Pharr figure among the inventors of the commercially most popular Nanoindenter (Nano Instruments Inc., Knoxville, Tennessee, USA), while Field and Swain were involved in the production of UMIS 2000 (CSIRO, Lindfield, Australia)). Therefore, the interesting procedure proposed in 1998 by Gerberich and coworkers [68] is still less frequently used than the above-mentioned two methods. Consequently, the present review would not be complete without presenting several alternative approaches that permit one to estimate the elastic modulus of the tested surfaces.

The Analysis of Söderlund, Rowcliffe, and Coworkers. In order to separate the machine compliance from the response of the investigated surface, Söderlund and Macmillan propose [69] an advanced analysis of sharp indentation results based on mathematical modeling of the combined behavior of the material–indenter system. They determined elastic contact stiffness as a continuous function of the effective displacement of the indenter by employing differential technique. This permitted them to evaluate Young's modulus of the investigated material when the appropriate contact model was in use.

The particularly important remark by Söderlund and Macmillan concerns the occurrence of plastic deformation (almost inevitable with sharp indenters), which might considerably affect the unloading behavior. This problem, studied thoroughly by Rowcliffe, Söderlund, and coworkers [70–72], was commonly dismissed in other approaches (refer to the preceding sections). Furthermore, their study concerning strain hardening, which occurs during indentation process, proved that a tip of Berkovich type is quite useful when either plastic or elastic properties of a solid surface are investigated [71].

The Method of Hainsworth et al. The original method that enables one to evaluate Young's modulus of the examined material using the loading, rather than unloading, part of an indentation cycle, is proposed by Hainsworth et al. [73]. The authors of the procedure claim that for a range of materials, including stiff, hard materials, inhomogenous systems, and thin hard films (HFs), the unloading indentation curve that is normally used to determine the elastic modulus exhibits unsatisfactory behavior. Hainsworth et al. found that unloading cycle scarcely fits the existing models by Oliver and Pharr [36, 47] or Field and Swain [48, 60]. Consequently, they concluded that the pertinent information on elastic and plastic properties of an indented solid might be extracted from the loading curve. The latter was found to follow the power-law (quadratic) relationship, for sharp tips [73].

Hainsworth et al. [73] accepted the simplified assumption that the tested material is rigid plastic and its hardness H remains constant (hardness parameter does not represent a material constant. The measured conventional hardness H markedly increases with decreasing maximum load $P_{\max}$, an effect clarified by Begley and Hutchinson [74]) with decreasing indentation load P. In such a case, the relationship between the contact radius a, indentation load, and the hardness reads:

$$a = \sqrt{\frac{P}{H}}. \tag{2.14}$$

Following the approach of Loubet et al. [75] for sharp indenters, the plastic h_p and elastic h_e components of the indentation depth h depend on the contact radius:

$$h = h_p + h_e = \eta a + \xi \frac{P}{Ea} = \eta \sqrt{\frac{P}{H}} + \xi \frac{P}{E} \sqrt{\frac{H}{P}}, \tag{2.15}$$

where η and ξ which depend on the indenter geometry, were empirically determined by Hainsworth et al. [61], while E stands for Young's modulus of the investigated material. eqn (2.15) yields the power-law dependence between the indentation load and the depth:

$$P = K_m h^2, \tag{2.16}$$

where

$$K_m = E\left(\eta \sqrt{\frac{E}{H}} + \xi \sqrt{\frac{H}{E}}\right)^{-2}. \tag{2.17}$$

Hainsworth et al. [73] empirically verified eqn (2.16) for a number of materials with widely varying E/H ratio. The tests were performed for various metals (steel, bronze, copper, and iron), silicon crystals, and for TiN and CNx thin films. The authors found that the P–h^2 relationship holds when the constant parameters take particular values of $\eta = 0.194$ and $\xi = 0930$.

In summary, Hainsworth et al. [73] claimed to be able to predict the shape of the loading indentation curves, which allows one to determine the commensurate value of Young's modulus E of the indented material in cases when hardness H is known. Further, their model enabled them to foresee the indentation response of the material when its elastic modulus and hardness are already determined.

Determination of the Elastic Modulus Supported by FEM Analysis. A simple relationship between the elastic modulus of the indented surface and the P–h unloading data was derived by Taljat et al. [76] who investigated the ball-indentation process by combining the FEM simulation and the so-called "surface response approach" (SR). The latter concerns the stress–strain curve of the indented material used as an independent variable (input) in FEM calculations. Taljat et al. [76] define Young's modulus of the indented solid as a functional dependence on a normalized unloading slope S_u and the estimate of deformation d/D (ratio of the diameter of the impression and the indenter):

$$E = f\left(S_u, \frac{d}{D}\right) = \left[C_1\left(\frac{d}{D}\right)^{C'}\right] S_u, \qquad (2.18)$$

where C_1 and C' were determined using finite element analysis of the indentation process. The unloading slope S_u was evaluated by SR procedure (details in [76]), that is, the authors estimated the indenter deformation employing an analytical solution for the displacement of the center of the contact circle. The obtained value was subtracted from the total indenter compliance, a correction that plays a major role in the calculation of elastic modulus. Importantly, Taljat et al. [76] confirmed the validity of their proposal by performing experiments on three materials with quite different Young's moduli, namely, aluminum, copper, and steel.

The Method of Elastic Loading and Elastic–Plastic Unloading. The complete analysis of elastic loading and elastic–plastic unloading of a spherical indenter was devised by Gerberich et al. [68] who propose a novel method deriving Young's modulus evaluation suitable for nanoindentation experiments (ultralow loads). The essence of the approach lies in the original analysis of elastic displacement above (h_1) and below (h_2) the contact line (refer to Fig. 7). The method proposed by Gerberich proved to be equally suitable for metals and ceramics (see examples in [68]).

The authors considered both loading and unloading indentation cycles, and studied penetration accompanied by pileup of the material adjacent to the impression, as well as when such a pileup is absent (see Fig. 8). The pileup affects the value of Young's modulus estimated from the indentation data, since its presence causes difference in elastic displacement above and below the contact line ($h_1 \cong h_2$, refer to Figs. 7 and 8). Such an approach contrasts with the

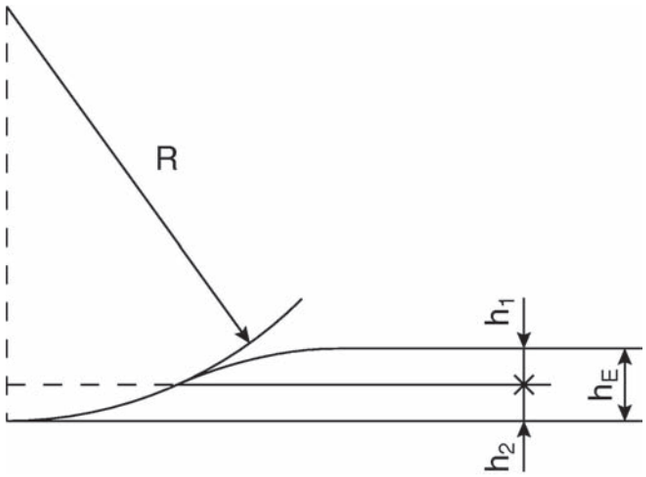

Figure 7. The geometry of elastic penetration of spherical indenter into a solid surface – model by Gerberich et al. [68].

elastic analysis of Field and Swain [61], who assume the displacements above and below the contact line to be equal ($h_1 = h_2$). Furthermore, Gerberich et al. [68] were aware of the fact that elastic displacement above the contact line h_1 is proportional to the total elastic displacement of a spherical tip h_E into an elastic–plastic material (refer to Fig. 8), which yields:

$$h_1 = \alpha \frac{h_E^{\max}}{h_t} h_E + \beta \ , \qquad (2.19)$$

where $h_E^{\max}$ ($h_E^{\max} = h_t - h_r$) is the elastic displacement during unloading, while h_t represents the maximum indentation displacement ($h_t = h_{\max}$). The constants α and β may be evaluated by considering the respective boundary conditions for an elastic contact:

$$h_2 = h_E / 2, \quad h_2 = h_E / 2, \quad h_t^{\max} = h_E^{\max}, \qquad (2.20)$$

or for a rigid-plastic contact:

$$h_f = 0, \ h_2 = 0, \ h_t^{\max} = h_p = h_t. \qquad (2.21)$$

The solution of elastic and rigid-plastic contact problems with the imposed boundary conditions allowed the authors to determine elastic displacements (h_1 and h_2) and contact radius (a) for a particular indentation load (P):

$$h_1 = \frac{h_E}{2}\left(\frac{h_E^{\max}}{h_t^{\max}}\right),$$

$$h_2 = h_E - h_1 = \left(1 - \frac{h_E^{\max}}{2h_t^{\max}}\right) h_E,$$

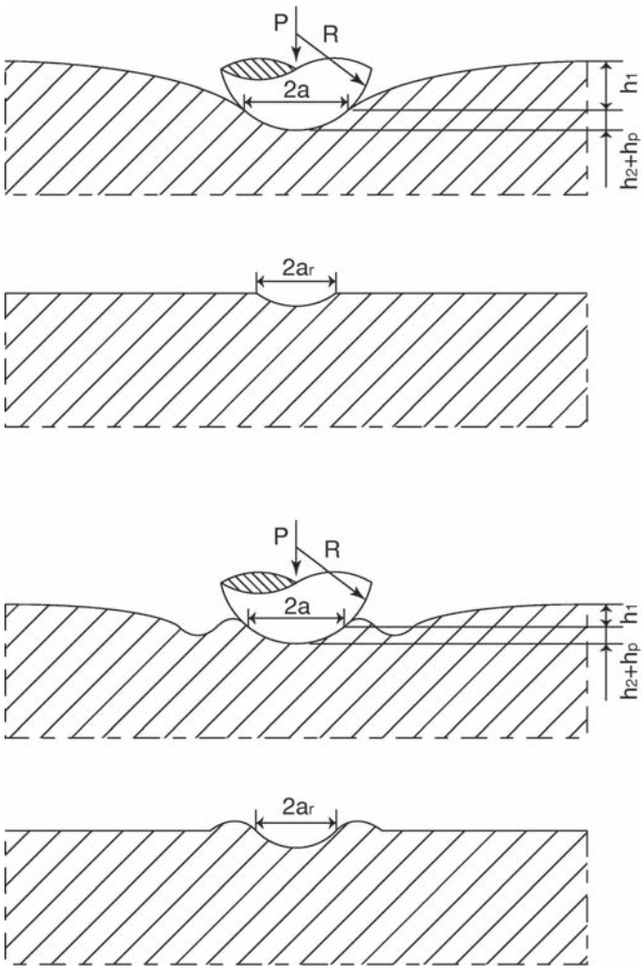

Figure 8. The schematic of elastic–plastic contact of spherical indenter discussed by Field and Swain [60, 61] – the case with and without pileup of material.

$$a = \left[\left(2 - \frac{h_E^{\max}}{h_t^{\max}}\right) R h_E - \left(1 - \frac{h_E^{\max}}{2h_t^{\max}}\right) h_E^2\right]^{\frac{1}{2}},$$

$$P = \frac{4Ea^3}{3R\left(1-\nu^2\right)}, \qquad (2.22)$$

where R is the radius of the tip. Further manipulation with eqn (2.22) led to a formula proper for the entire unloading curve, which allowed Gerberich et al. [68] to evaluate exactly the effective elastic modulus E_{eff}:

$$E_{eff} = \frac{3RP}{4\left[\left(2 - \frac{h_E^{\max}}{h_t^{\max}}\right) R h_E - \left(1 - \frac{h_E^{\max}}{2h_t^{\max}}\right) h_E^2\right]^{\frac{1}{2}}} \qquad (2.23)$$

The authors emphasize that their approach describes accurately the unloading curve, and consequently they are able to estimate the elastic modulus at each point of the unloading cycle. Moreover, Gerberich et al. [68] compare their results with the data obtained when applying the Doerner and Nix [33] or Field and Swain [60] method to fused quartz, polycrystalline aluminum, and a single crystal of tungsten. Their estimation of Young's modulus and hardness of the tested materials appears to be precise as far as the relatively high loads are considered.

2.1.5. Elastic Modulus Derived from a Nanoscale Deformation: A Dilemma in Nanoindentation

The nanoindentation experiments coupled with a complete and anisotropic 3D finite element simulation provide the first exposure of a consistent difference in nanomechanical response of the various crystallographic planes of sapphire loaded with spherical indenters [38, 77]. The available analytical solutions for the elastic contact between rigid diamond indenter and sapphire were negatively verified by the indicated tests, in contrast to the finite element calculation with deformable tip. The main conclusion of these findings [38] is that although nanoindentation is frequently claimed to be a nondestructive testing method, it is – in fact – not. The authors found that the accuracy of the experiments available today is compromised by the structural changes induced during loading. The result is an erroneous estimation α using the commonly accepted Oliver–Pharr method [34] of the elastic characteristics of the sapphire surfaces (refer to Fig. 9).

Indeed, their precise nanoindentation experiments supported by FEM simulation of the elastic contact between the spherical tip and the anisotropic Al_2O_3 crystal prove that the elastic modulus and its anisotropy cannot be correctly determined using the unloading cycle of the elasto-plastic indentation curve [38], as routinely exercised within the

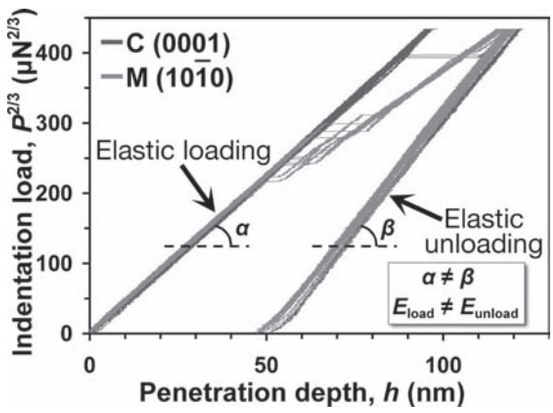

Figure 9. The nanoindentation $P^{2/3}$–h curves recorded for sapphire (Nowak et al., unpublished) that display the difference between Young's moduli determined by Hertzian relationship [41] and Oliver and Pharr [36] method. The latter approach provides erroneous evaluation of elastic parameter.

widely accepted procedure by Oliver and Pharr [34]. This paper recommends determination of elastic properties from the perfectly elastic nanoindentation cycle recorded prior to the point at which the pop-in event occurs, using simple Hertzian calculations, FEM inverse analysis, or something like a three-parameter constitutive low approach [78]. The unloading response of the crystal volume that was partly transformed during pop-in event would be, in general, different than elastic recovery of the virgin sapphire surface.

2.2. Determination of Hardness

As was mentioned in Section 1, the physical importance of hardness *H,* denoted according to Meyer's concept eqn (1.1), lies in the relationship between the *H* value and the fundamental physical parameters such as yield strength σ_Y [eqn (1.2)] or Young's modulus *E*. While hardness is widely used by engineers, it appears to be ill defined and neither represents material constant nor describes a single material property. The latter concern was expressed in the comprehensive review by Söderlund and Rowcliffe [70], who point out that the measured hardness *H* is affected by indentation-induced cracking, densification, strain hardening, and creep of the tested solid. Consequently, *H* is a function of Young's modulus *E*, yield strength σ_Y, toughness K_{IC}, work hardening exponent *n*, or stress-dependent creep rate $\dot{\varepsilon}^c$.

Hence, hardness appears as an engineering parameter that depends even on the applied maximum indentation load P_{max} (refer to the footnote in page 18), that is, its value should not be viewed exclusively as a material characteristic. Furthermore, Pethica et al. [12] report a particularly significant increase in hardness when the indentation size drops below 1 μm, which they related to alteration of the acting yield mechanism for ultralow load deformation. The above-mentioned examples persuade one to conclude that hardness should not be considered in the same way as other material properties such as strength, yielding limit, resistance to crack propagation, or electrical resistivity.

With the advent of depth-sensing indentation instruments, confusion arose as to how to determine the hardness parameter from the monitored displacement of the indenter. Should it be deduced, for example, from the maximum depth h_{max} (refer to Fig. 3) or calculated using the residual penetration depth h_r? Starting with the pioneering work by Oliver et al. [79], efforts were made to determine the characteristic contact area *A*' at each step of the penetration and consequently, to obtain Meyer's hardness using eqn (1.1):

$$H = P/A', \tag{2.24}$$

Therefore, the estimation of the depth-hardness profile became the standard procedure recommended to users of commercially available depth-sensing testers (the methods are discussed in the following sections).

It is worth emphasizing that an alternative definition of hardness H_T, which appears as a load-independent parameter, was introduced by Sakai and Nowak [44–46]. In contrast to the other approaches, H_T is a physical parameter defined according to the energy consumed for an irreversible deformation of an indented material. The formula for H_T was derived from constitutive equations for the ideal geometry of axisymmetric contact [44].

2.2.1. Hardness under Load: A Concept of Doerner and Nix

Doerner and Nix [33] consider hardness, defined according to eqn (2.24), to be equal to the average pressure under the acting indenter ($\langle p \rangle = H$). They suggest that the elastic contribution h_e to the entire indentation depth *h* should be subtracted, in order to evaluate the level of hardness associated essentially with plastic deformation. According to these authors, plastic indentation depth h_p may be determined (refer to Section 2.1.2) by extrapolating to zero load the line that is fit tangent to the unloading $P-h$ curve (see Fig. 3). Doerner and Nix [33] assumed ideal indenter geometry (Vickers and Berkovich pyramids) that remains unchanged during the penetration process, and estimated the projected contact area A_p that quantifies the permanent deformation (plastic) of the tested solid. The hardness determined according to the plastic part of the penetration depth h_p (Fig. 10) was expected to approach the conventional *H* value defined by eqn (1.1).

Doerner and Nix were aware of the drawbacks that stem from their assumption of a perfectly rigid indenter [33]. In order to determine precisely the profile of the loaded penetrator, they used two-stage carbon replica imaging of the deformed surface, the approach originally proposed by Pethica et al. [12]. Thus, the low-load impressions were observed by means of transmission electron microscopy, and the calibration of an indenter shape was achieved by empirical determination of the relationship between the cross-section area A'_{exp} and indentation depth *h* for Vickers and Berkovich diamond tips. Doerner and Nix [33] argue that, during a single indentation cycle, tip-shape correction allows one to determine precisely the hardness-depth dependence for bulk and thin-film crystalline materials. They concede, however, that the estimation of the influence of strain rate on the obtained results is beyond the resolution of the proposed method.

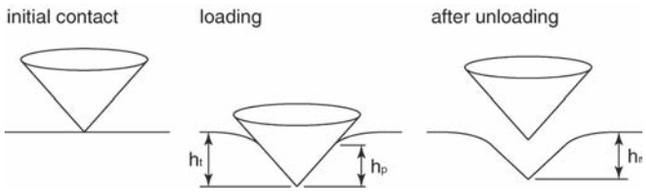

Figure 10. The schematic of the analysis by Doerner and Nix [33], where h_r, h_t, and h_p represent final, total, and plastic indentation depth, respectively (see Fig. 3).

2.2.2. Estimation of Hardness According to Pharr and Oliver

Since depth-sensing indentation equipment allows one to monitor the load experienced by a diamond tip during the penetration process, the principal difficulty associated with evaluation of hardness lies in the estimation of the projected area A' of permanent indentation according to eqn (2.24). Pharr, Oliver, and coworkers advocate determination of their shape function $A = f(d_c)$, that is, the empirically assessed shape of the indenter at the contact depth h_c [34, 36], an issue discussed earlier in Section 2.1.2. The $f(d_c)$ function denotes the relationship between the cross-sectional contact area A and the distance d_c from the indenter tip, which locates the cross section, as shown in Figure 11. The $A - d_c$ dependence can be assessed from the depth-sensing indentation data, which allow one to evaluate readily the relationship between the area A and the contact depth h_c (refer to Fig. 11).

Pharr et al. were aware that hardness results, particularly those obtained under ultralow load, contain systematic error owing to deviation of the shape of the tip from ideal Berkovich geometry [47]. Indeed, the tip rounding of a triangular penetrator was discovered as early as 1983, when Pethica et al. estimated the tip radius to equal 15 nm [12]. Four years later, the corrected value of 50 nm was reported for the radius of the Berkovich tip [80], while the work of Doerner and Nix [33], and Pharr et al. [14, 34, 36, 47] provided the basis for believing that the value in question ranges from 10 to 100 nm. A thorough study of the effect of tip radius on nanoindentation results was carried out by Shih et al. [81], and more recently by Bei et al. [82], who presented a finite element simulation of the indentation process based on continuum solid mechanics.

Oliver and Pharr [34] used the $f(d_c)$ shape function derived for perfect Berkovich tip geometry, which reads:

$$f(d_c) = 24.56 d_c^2 \ , \tag{2.25}$$

for an initial estimation of the contact area. To determine a realistic shape of the sharp indenter, Pharr et al. used a standard specimen, that is, they carried out indentation experiments under various loads P_{max} in fused quartz or silica, the materials with well-defined isotropic properties [34, 36, 47]. Finally, the function $f(d_c)$ was calculated according to the formula [34]:

$$f(d_c) = 24.56 d_c^2 + C_1 d_c^1 + C_2 d_c^{1/2} + C_3 d_c^{1/4} + ... + C_8 d_c^{1/128} \ , \tag{2.26}$$

where $C_1 - C_8$ denote constants.

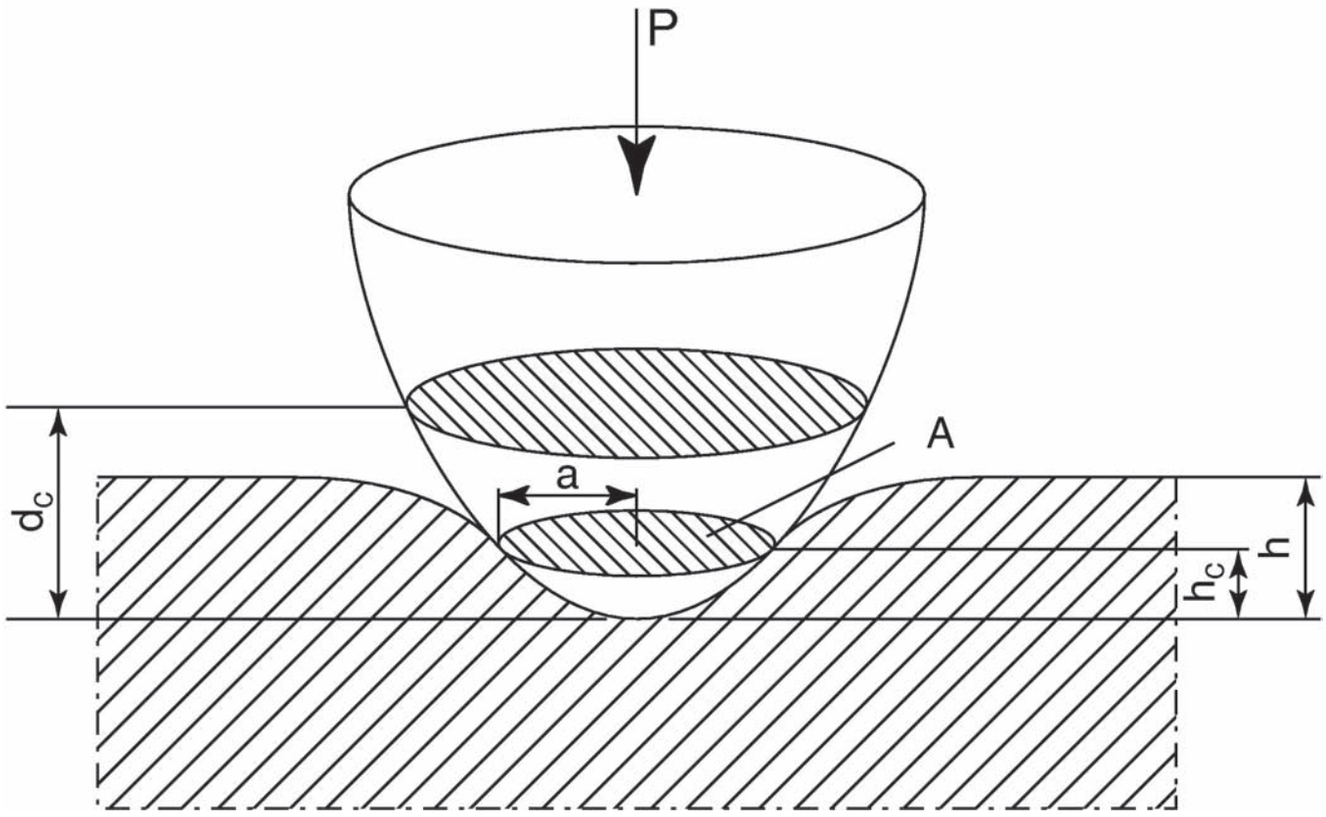

Figure 11. The parameters used in evaluation of the indenter shape function by Pharr and Oliver [34, 36]. The parameters h, h_c, d_c, P, and a stand for indentation depth, depth to the contact, distance of cross section from the indenter tip, indentation load, and a radius of the contact area, respectively.

The function f was determined from the $P-h$ data, assuming that Young's modulus of the standard sample does not vary with indentation depth. The above restriction imposed on the model does not undermine the validity of the approach employed by Oliver and Pharr unless we do not deal with nanoscale deformation [38]. The former authors proved that a single area function determined according to their method fits the experimental results obtained for aluminum, quartz, soda-lime glass, sapphire, fused silica, and tungsten [34, 36, 47]. eqn (2.26) is not a final output of the analysis proposed in studies by Pharr et al. [36], since the procedure of multiple fitting was exercised within the iteration method to achieve satisfactory accuracy. Once the $f(d_c)$ function was determined, it was possible to evaluate the hardness from the indentation results according to eqn (2.24).

In order to provide a fresh insight into hardness analysis, Pharr and coworkers [83] investigated the influence of material pileup on hardness of the indented solid, using finite element simulation of the axisymmetric contact between the rigid indenter and elastic–plastic material with constant Young's modulus (70 GPa) and yield strength ranging from 0.114 to 26.62 GPa [47, 83]. The authors registered a pronounced pile-up effect on the hardness level when the ratio of residual to the maximum indentation depth exceeded 70% ($h/h_{max} > 0.7$), and the solid did not work-harden significantly. In such a case, the error in estimating the hardness value might be as great as 50%. Consequently, the procedure developed by Oliver, Pharr, and coworkers [34, 36, 47] allows one high-accuracy evaluation of hardness for materials that obey the empirical criterion ($h/h_{max} < 0.7$), that is, those that do not produce significant pileup during indentation.

2.2.3. Evaluation of Hardness Aided by Finite Element Calculations

Numerical simulation of the indentation process frequently provides results that could not be obtained directly from experiments, as mentioned earlier in Sections 2.1.1 and 2.2.2 of the present review. Indeed, once the penetration is simulated, there is no obstacle to estimate the contact area (the parameter essential for the calculation of hardness, which cannot be assessed experimentally) at any possible stage of the indentation process. This argues for the capability of the finite element approach to explore the theoretical foundation of hardness. Moreover, numerical simulation of indentation allows one, nowadays, to draw conclusions about a variety of mechanical characteristics of the tested solid, such as contact stiffness, the effective elastic modulus (see Section 2.1.4.3), and yield strength. Alternatively, it may be used to predict the surface profile (the pileup or sink-in effects, refer to Fig. 8) around the contact with the indenter, and the shape of the plastic zone created directly under an acting tip.

Recent interest in finite element analysis of indentation data stems from the advantages of such an approach and from the fact that high-speed computational capabilities are readily available nowadays. It is becoming increasingly popular among users of nanoindentation systems to employ the FEM method to estimate the mechanical characteristics of advanced and new materials, and clarify their indentation behavior. In the case when one goes into nanoscale deformation, even the FEM approach is insufficient and the analysis based on atomistic simulation must be used, while a few years ago this subject was exercised exclusively by specialists. A concise, yet complete, historical review of the computer simulation of the indentation process is given in following sections of the present review.

Finite Element Simulation of a Spherical (Brinell) Indentation. The first attempts to resolve deformation and stresses during spherical indentation of an elastic–plastic halfspace using FEM calculations were made by Hardy et al. [84], and independently by Lee et al. [85]. The latter calculated load–displacement ($P-h$) response for frictionless indentation and drew conclusions about pressure distribution and the shape of the plastic zone created under the acting tip. The numerical results concerning $P-h$ data for a steel specimen were verified by the authors using the tester of their original design, equipped with a WC ball (radius of 10 mm). Consequently, Lee et al. [85] found that the representative strains (the parameter used in Tabor [4, 5]) coincide with the mean effective strains in the plastic zone created directly under the indenter, which supports Tabor's concept of H–σ_Y relationship, as in eqn (1.2). It should be emphasized that the report by Lee et al. [85] was published in 1972, that is, long before the idea of depth-sensing hardness measurements had become generally accepted.

The spherical and frictionless indentation in an elastic–plastic halfspace was further studied by Follansbee et al. [86]. The authors calculated stresses, strains, and displacements generated at different load levels as well as surface displacement profiles using the theory of incremental elasto-plasticity for homogenous, isotropic, and elastic–incompressible–plastic solids that comply with the von Mises yield criterion, and in consequence, satisfied the conditions of strain rate–displacement rate relations for small strains. The calculations led to the quantification of residual tensile stresses induced during the penetration process and enabled the authors to determine the expected size of the residual impressions. Hence, Follansbee et al. [86] were able to evaluate the Brinell hardness of stainless steel by using the FEM method and verify their results using experimental data. They also provided a theoretical confirmation of Tabor's relationship [eqn (1.2)] for work-hardened materials.

Thorough theoretical studies of Brinell hardness were undertaken by Hill, Storåkers, and coworkers [6, 87], who derived general expressions for the influence of the tip shape on the load and surface deformation by solving a class of boundary value problems in elasticity. The authors applied the new FEM procedure to the deformation theory of plasticity. Their numerical simulations were performed for the elasto-plastic homogenous halfspace with all-around isotropy, while indented to a fixed depth by a smooth rigid ball [6, 7, 88]. The solid was deformed according to the power-law hardening rigid-plastic model. The proposed analysis dealt with small-strain linear kinematics of frictionless indentation process.

Hill et al. [6] report nonproportionality of strain evolution in the vicinity of a contact boundary. They determined the distribution of contact pressure, the profile of the deformed surface, and the contours of representative strain, which allowed them to verify the commonly accepted Tabor's relationship [eqn (1.2)]. Further, Storåkers and Larsson [7] analyzed the indentation into materials with time-dependent properties reproduced by power-law creep [4, 5, 89]. This led to the derivation of a universal relationship for hardness at creep, applicable for Boussinesq and Brinell indentation, which reads:

$$\frac{P}{\pi a^2} = \alpha\sigma_c \left\{ \left(\frac{\beta}{(2n+1)D} \right)^2 \left(\frac{P}{\pi\alpha\sigma_c} \right) t^{-2} \right\}^{\frac{i}{2n+1}}, \quad (2.27)$$

where a is the contact radius under the ball indenter of diameter D, t denotes the time, and σ_c and n are the material parameters defined by the stress–strain ($\sigma-\varepsilon$) creep law given by Norton [90]:

$$\frac{d\varepsilon}{dt} = \left(\frac{\sigma}{\sigma_c} \right)^n \quad (2.28)$$

The findings of Storåkers, Hill, and Larsson [6, 87] accord with Tabor's experimental results obtained for the Brinell hardness test [4, 5], and it was realized that the Tabor formula has complement at creep [eqn (2.27) and Ref. [7]]. Further, Biwa and Storåkers [88] accomplished explicit solutions for plastic solids with hardening, that is, for those that asymptotically approach a fully plastic state during the penetration process. Their analysis deals with power-law hardening of materials that obey the Levy–Mises flow rule.

The specially designed finite element procedure employed mixed, nine-node quadrilateral elements, and purpose-built meshes (refer to the examples shown in Fig. 12) which provided 24,000 degrees of freedom. The studies of the indentation in the low-strain hardening materials performed by Storåkers, Hill, Larsson, and coworkers [6, 7, 87, 88] suggest that the bulk of deformation occurs in material located very close to the indenter tip. This prompted the authors to use smaller size mesh during subsequent stages of the simulation.

For the sake of completeness of this review, the early research that employed classic slip line field theory to the analysis of surface deformation of plastic–elastic materials should be mentioned at this stage, although such an approach is no longer in use. The numerical simulation of spherical indentation provided by Shaw and DeSalvo [91], who studied the plastic flow beneath a blunt axisymmetric indenter, serves as an example of these kinds of works.

Finite Element Simulation of a Sharp Indentation: An Axisymmetric Approach. Since the commercially available nanoindentation depth-sensing instruments are normally equipped with a sharp penetrator of a Berkovich or Vickers type,

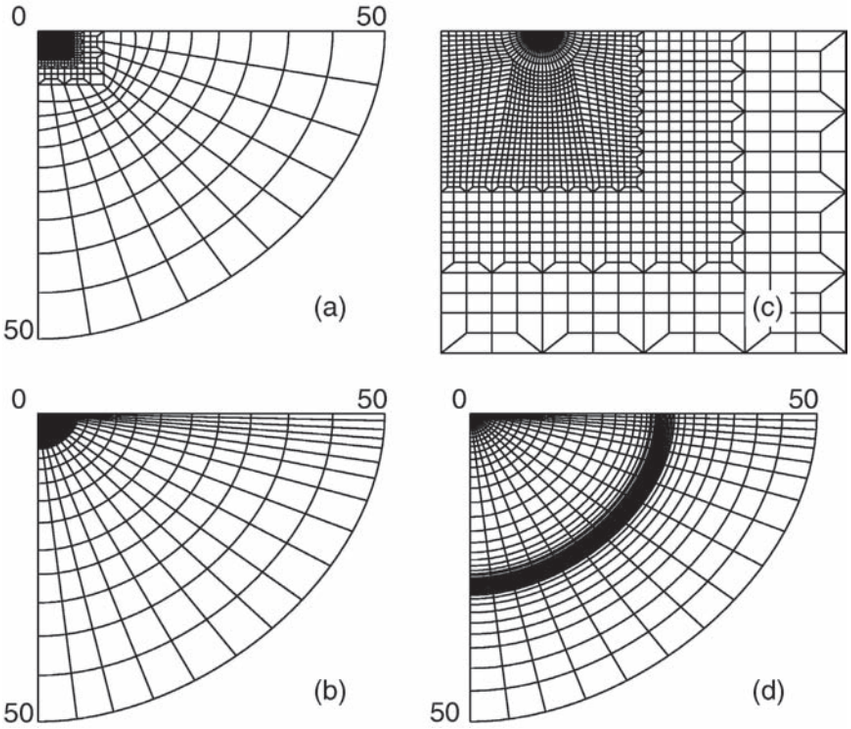

Figure 12. The examples of different FEM meshes for elasto-plastic indentation (a, b) and their details (c, d) in the contact region. The displayed combination comes from Brinell indentation by Hill et al. [6] (a, c), and indentation of creeping solids by Storåkers and Larsson [7] (b, d). The similar configuration was employed by Biwa and Storåkers [88] to analyze the perfectly plastic spherical contact.

the modeling of pointed indentation into solids under ultralow loads has drawn much attention. Consequently, finite element analysis of submicrometer sharp indentation was proposed in 1988 by Bhattacharya and Nix [39], and subsequently by Lursen and Simo [40] in 1992. The former used incremental elasto-plasticity in their computer-simulation studies of the frictionless penetration process of perfectly rigid indenter, as well as completely adhesive indentation contact. In order to maintain the computer time within reasonable limits, Bhattacharya and Nix [39] restricted their calculations to an axisymmetric cone with volume equal to a pyramid-shape indenter, arguing that such an approximation does not undermine the applicability of the obtained results. Indeed, the proposed simplification may be acceptable from the point of view of continuum plasticity, which was used throughout, despite its neglect of the elastic singularities that appear near the edges of a pyramidal indenter.

Three different materials: silicon, polycrystalline aluminum, and nickel, were used in the calculations of Bhattacharya and Nix [39], followed by an experimental verification of the simulated results. The applied constitutive equations were of an elastic–plastic von Mises type with lack of strain hardening (the elastic/fully plastic case), or alternatively, with linear, isotropic strain hardening. Since the simulation targeted ultralow load indentations, the authors constructed extrafine FEM mesh (Fig. 13). The grids were quite tiny near the indenter, which enabled the authors to estimate accurately the deformation and stress gradients, but became progressively coarser further from the contact area (refer to Fig. 1). The pint-sized mesh was applied directly below the contact (four node elements, 0.02 μm thick), which made it possible to estimate accurately the radius of the contact area.

An important advantage of the study by Bhattacharya and Nix [39] was the comparison of the values of hardness and elastic modulus estimated according to the three methods: the punch approximation of Loubet et al. [57, 75], the extrapolated depth model of Doerner and Nix [33], and their own FEM results. The authors found that their findings support the concept of the extrapolated depth [33] as the most reliable measure of plastic indentation depth.

Significantly, Bhattacharya and Nix demonstrated that the $P-h$ curves obtained by means of ultralow load indentation experiments could be effectively simulated, using the FEM with simple constitutive data. They clarify how the relevant mechanical parameters such as hardness and elastic modulus might be extracted from the numerical results and how the hardness of solids varies with the depth of penetration. Further, they obtained a satisfactory agreement between the calculated and the measured data [39], which prompted further development of FEM analysis of nanoindentation experiments. It is worth noting that the same authors extend their considerations to the indentation of various combinations of hard–soft thin films and substrates [92], and provide the evaluation of film hardness based on a concept of collective deformation of thin film–substrate composite.

Following the research of Bhattacharya and Nix [39, 92], Lursen and Simo [40] present a detailed numerical simulation of surface deformation of elastic–power-law plastic materials. They address axisymmetric cone indentation into bulk aluminum and silicon, as well as thin films of various degrees of thickness, namely, aluminum on a silicon substrate and silicon on an aluminum substrate. The emphasis is on the numerical evaluation of the contact area and the surface profile near an indentation impression.

Despite the numerous simplifications used by Lursen and Simo [40], their studies are firmly based on solid mechanics, and they point toward the necessity of simultaneous consideration of the inelastic and elastic behavior of the indented

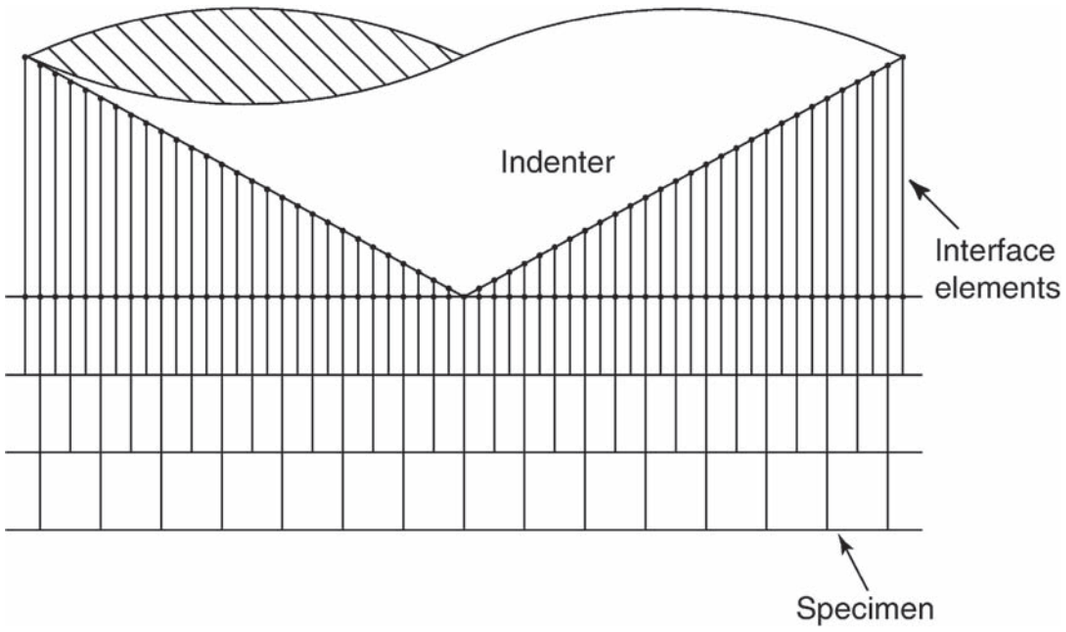

Figure 13. The schematic of the FEM mesh near the axisymmetric conical indenter used in [39].

solid. Consequently, the indented material was modeled in their study, using the constitutive theory of large elasto-plastic deformation that was earlier developed by one of these authors [93]. The solution to the boundary value problem is applied to traction, displacement conditions, and unilateral constraint. The indented solids were idealized using J_2 flow theory (J_2, second invariant of the stress deviator) with linearly isotropic hardening.

In spite of several coinciding assumptions, the arrangement of the FEM computation process by Lursen and Simo [40] differed from the one proposed earlier by Bhattacharya and Nix [39]. Indeed, a rigid conical indenter with an apical angle of 136° was used in both the works, while the FEM mesh designed by Lursen and Simo (refer to Fig. 14) contrasts with the meshes in Bhattacharya and Nix (Fig. 13). The new mesh (Fig. 14) contained 2419 nodes and 2285 elements with a very fine structure near the indenter (similarly to Bhattacharya and Nix [39, 92]), while it possessed very fine zones at the material surface directly below the indenter and in the case of the layered structure – at the film–substrate interface (this contrasts Refs. [39, 92]). Furthermore, the indentations were assumed to reach the penetration depth of 1 μm, while roller boundary conditions were applied to the outer and bottom surfaces of the mesh, and far-field boundary conditions were satisfied by the use of a coarse mesh (see Fig. 14).

The resolution achieved using their method enabled Lursen and Simo [40] to evaluate the contact area during the penetration process, and, thus determine the hardness depth profile for the investigated solids. The authors additionally took into account the pileup and sinking-in effect (The pile-up effect and its influence on hardness measurements have been thoroughly studied by Gerberich [68] (see Fig. 8 and Sections 2.1.4.4 and 2.2.2). However, it is worth noting that a consideration of the pileup–sinking-in by Lursen and Simo appeared as early as 1992.), while evaluating the hardness of the bulk and the thin film materials. They found that the inaccurate determination of the contact area from plastic depth (see, e.g. [33, 39]) is owing to the neglect of the pile-up phenomenon [40]. Hence, Lursen and Simo [40] emphasize that the computer-simulation experiments made it possible to estimate the parameters that cannot be obtained experimentally, such as the contact area, yield zone, or the distribution of stress under the tip.

More recently, Nowak et al. [94] applied the FEM simulation of the penetration by an axisymmetric indenter into a HF–soft substrate system to clarify the surprising difference in hardness of virgin and ion-bombarded HfN thin films deposited on silicon wafer. Their finite element calculations led to the identification of an amorphous silicon interlayer that was formed directly beneath the upper HfN film because of the bombardment of the material with highly energetic ions.

Three-Dimensional Finite Element Simulation of a Sharp Indentation. Axisymmetric approximation of the pyramidal shape of the Vickers- or Berkovich-type indenter undertaken by numerous scholars [39, 40, 92, 94] is scarcely acceptable in the case of an anisotropic material. Such a simplification affects the precision of the prediction provided by a numerical simulation, although it considerably improves the speed of the calculations. Hence, an accurate and three-dimensional (3D) finite element analysis of a sharp indentation has become required from the practical standpoint. Moreover, the 3D approach offers better

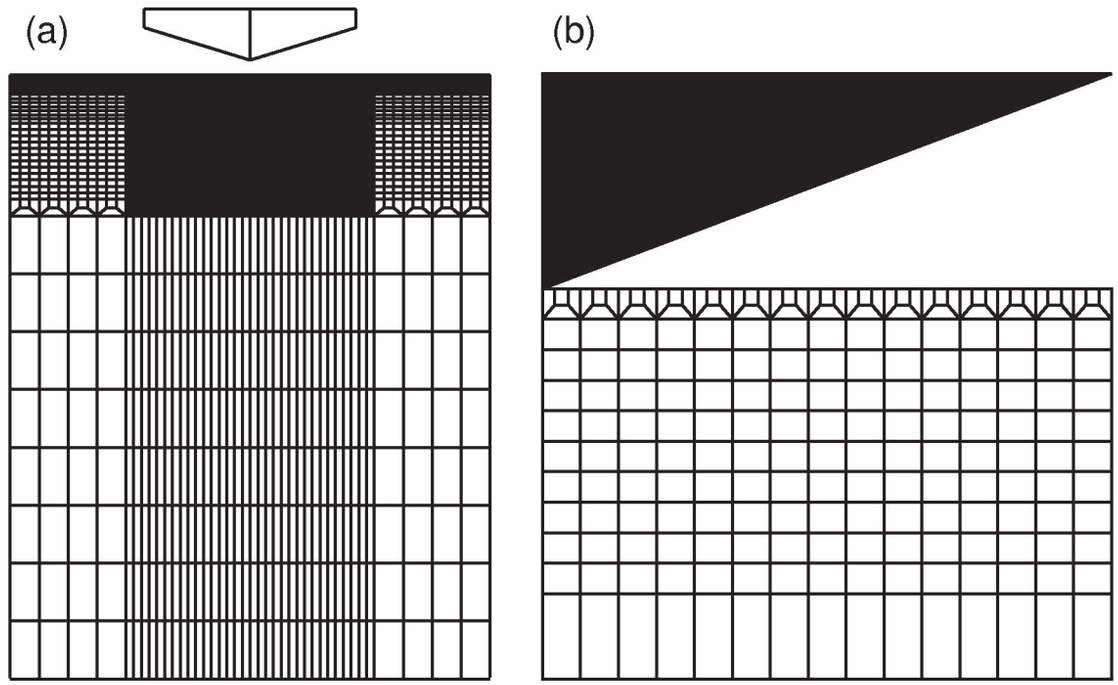

Figure 14. The schematic view of the FEM mesh (a) and fine meshing near the conical indenter (b) used in [40].

understanding of the mechanics involved in nanoindentation experiments.

The first attempt to perform a 3D finite element simulation of indentation by Wang and Bangert [95] was soon followed by a complete analysis of the Vickers indentation carried out by Giannakopoulos et al. [96], who attempt to solve the problem of penetration of a rigid indenter into homogenous, rate-independent, and semi-infinite body – a frictionless, quasi-static, and isothermal process.

The calculations performed according to both the small and the large-strain formulations were accomplished for a solid with incrementally elasto-plastic and rate-independent constitutive behavior with isotropic hardening. Hooke's law and the Prandl–Reuss equations governed the elastic and elasto-plastic deformation of the material, respectively. The required accuracy and efficiency (reasonable computer time of numerical calculations) was achieved through appropriate meshing applied by Giannakopoulos et al. [96], who took advantage of the eightfold symmetry of the problem and limited the considerations to one-eighth of the material volume (Fig. 15). The authors tested extensively various kinds of meshes to engulf the existing analytical solutions to the elastic contract problem proposed by Boussinesq [52] and Sneddon [54], whose final mesh was composed of 8524 eight-nodded isoparametric elements and 9914 nodes. Giannakopoulos et al. [96] point toward the importance of the mesh details, arguing that the differences between the numerical results obtained by Lursen and Simo [40] and Bhattacharya and Nix [39, 92] were caused by the noncoincident meshing used in these reports.

The small-strain formulation and elastic analysis of Giannakopoulos et al. [96] allowed them to draw conclusions about the parabolic relationship between the indentation load P and depth h at the loading cycle:

$$P = 2.0746\left(1-0.1655\nu-0.1737\nu^2-0.1862\nu^3\right)\frac{E}{1-\nu^2}h^2, \quad (2.29)$$

which holds equally well when a large-strain hypoelastic analysis is performed. The numerically determined average contact pressure p_{av} is independent of load and depth, since the contact area scales with h^2:

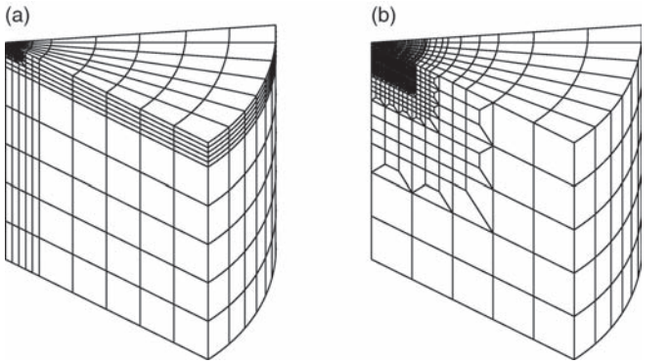

Figure 15. The schematic view of the FEM mesh used by Giannakopoulos et al. [96] (a) and its details at the contact area (b).

$$p_{av} = 0.2108\left(1-0.1655\nu-0.1862\nu^2-0.1862\nu^3\right)\frac{E}{1-\nu^2}, \quad (2.30)$$

while the deformation was found to be directly related to the indentation depth. Furthermore, the logarithmic nature of the stress singularity at the edge of the Vickers pyramid was clarified, and the deformation pattern close to the indented area was resolved [96].

The simulation of elasto-plastic penetration allowed the authors to estimate the influence of pile-up and yield stress levels on the Vickers hardness H_V, considered in terms of average contact pressure ($p_{av} = H_V$), and resulted in the universal formula for the Vickers hardness:

$$p_{av} = C\sigma_u\left(1+\frac{\sigma_Y}{\sigma_u}\right)\left(1+\ln\frac{E\tan 22^\circ}{3\sigma_Y}\right)\left(1-\frac{u_{2\max}}{h}\right), \quad (2.31)$$

where C is a constant, u_{2max} defines the maximum positive surface displacement caused by material pileup, while σ_u and σ_Y represent the ultimate stress and yield stress, respectively. They were also able to assess the $P-h$ relationship for elasto-plastic deformation [96]:

$$p = 1.06h^2\left(\tan 22^\circ\right)^{-2}\sigma_u\left(1+\frac{\sigma_Y}{\sigma_u}\right)\left(1+\ln\frac{E\tan 22^\circ}{3\sigma_Y}\right), \quad (2.32)$$

which appeared to be of a parabolic type, similar to the result obtained from purely elastic considerations [see eqn (2.29)].

Further, the calculations of steady-state hydrostatic stress and von Mises effective stress profiles performed by Giannakopoulos et al. [96] for materials with and without strain hardening suggest that strain hardening tends to suppress pileup at the contact boundary. The maximum tensile principal stress at loading, predicted in the vicinity of indenter tip, helped the authors to locate the region in which the fracture is likely to be initiated. The results by Giannakopoulos et al. [96], which relate to the surface deformation and generation of the indentation cracks, were restricted mainly to metals, and were compared with the experimental data obtained by Pharr and Cook [97] for the Vickers depth-sensing indentation in aluminum as well as by Zielinski et al. [98] for Fe–3 wt.% Si crystals. However, the application of the continuum theory of deformation to highly anisotropic single crystals has severe limitations and appears to be successful in exceptional cases (see the introductory part of Ref. [99]).

The results of Giannakopoulos et al. [96] inspired Zeng and Rowcliffe [100], who propose a new method of measuring residual stress induced near the surface by indentation. Hence, the theoretically predicted distribution of von Mises and hydrostatic stress induced in soda-lime glass, and induced by Vickers indentation, was experimentally verified [100]. This agreement appears a remarkable achievement and points toward advantages of nanoindentation, since glass belongs to brittle solids with mechanical characteristics that cannot be obtained from tensile test (a problem that falls beyond the objective of the proposed analysis).

It should be noted that Zeng et al. [100] modified the original FEM model of Giannakopoulos et al. [96], using "true contact area function" which allowed them to simulate the $P-h$ data for glass. Consequently, the authors were able to estimate the level of yield stress, strain hardening, and elastic modulus of soda-lime glass from the numerical analysis of experimental indentation data. Further, the determined stress and displacement fields enabled them to predict directions of crack propagation [100], which were confirmed by the observations of indentation fracture in glass by Zeng et al. [101] and the thorough study of Salomonson et al. [102], who concentrate on the decay of residual stress during slow crack growth in soda-lime glass.

Pursuing their FEM studies of Vickers indentation [96, 100], both the teams (Zeng et al. and Giannakopoulos et al.) provide common analysis of the deformation induced around a triangular indenter [71]. The approach was similar to that proposed for Vickers hardness [96, 100], with corresponding assumptions and equivalent constitutive modeling of the deformed material. The generalized Hooke's law that governed elastic response of a deformed solid, considered according to small-strain formulation:

$$\sigma_{ij} = \frac{E}{1+\nu}\left(\delta_{ik}\,\delta_{jl} + \frac{\nu}{1-2\nu}\,\delta_{ij}\delta_{kl}\right)\varepsilon_{kl}, \qquad (2.33)$$

was replaced by Larsson et al. [71] with Prandtl–Reuss equations for the elasto-plastic behavior:

$$\sigma_{ij} = \frac{E}{1+\nu}\left[\delta_{ik}\,\delta_{jl} + \frac{\nu}{1-2\nu}\,\delta_{ij}\delta_{kl} - \frac{3\sigma'_{ij}\,\sigma'_{kl}\,\dfrac{E}{1+\nu}}{2\sigma_e^2\left(\dfrac{2}{3}\dfrac{d\sigma}{d\varepsilon_p} + \dfrac{E}{1+\nu}\right)}\right]\varepsilon_{ki,} \qquad (2.34)$$

where σ stands for uniaxial nominal stress, ε_p denotes the engineering nominal strain $\varepsilon_p = \varepsilon - \dfrac{\sigma}{E}$, while $\sigma'_{ij} = \sigma_{ij} - \dfrac{\sigma_{kk}\delta_{ij}}{3}$ and $\sigma_e = \dfrac{3}{2}\,\sigma'_{ij}\,\sigma'_{ij}$ are the deviatoric and the effective Mises stress, respectively.

The difference between the analyses of Vickers [96] and Berkovich [71] indentations stems from geometry. Sixfold symmetry allowed Larsson et al. [71] to restrict modeling for Berkovich tip to one sixth of the volume of the solid, while the applied FEM mesh contained considerably more elements (10,850 isoparametric block elements and 12,400 nodes) than that used for a Vickers penetration (compare Figs. 15 and 16). Larsson et al. [71] performed simulations of indentation into the materials modeled previously by Giannakopoulos et al. [96], namely, two types of aluminum with different kinds of hardening, the samples which were subsequently used to verify experimentally the calculated results. The authors found that the *P–h* relationship for a triangular tip is parabolic when the indentation is simulated using either the elastic [eqn (2.35)] or elasto-plastic [eqn (2.36)] approach:

$$P = 2.1891\left(1 - 0.21\nu - 0.01\nu^2 - 0.41\nu^3\right)\frac{E}{1-\nu^2}h^2, \qquad (2.35)$$

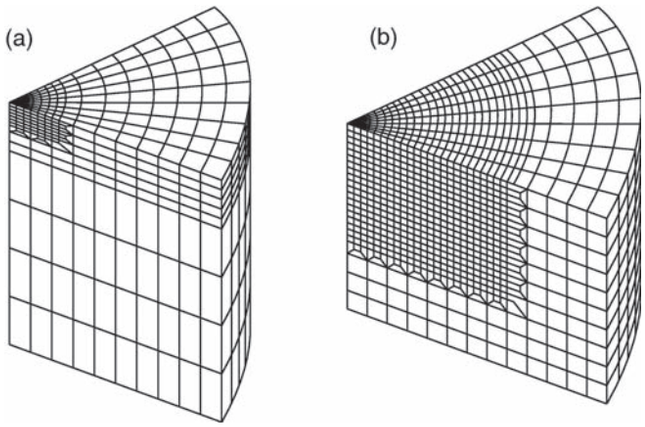

Figure 16. The schematic view of the FEM mesh by Larsson et al. [71] (a) and its details near the contact area (b).

$$P = 1.273h^2\left(\tan 24.7^\circ\right)^{-2}\,\sigma_u\left(1 + \frac{\sigma_Y}{\sigma_u}\right)\left(1 + \ln\frac{E\tan 24.7^\circ}{3\sigma_Y}\right), \qquad (2.36)$$

similarly to the results obtained by Giannakopoulos et al. [94] for the Vickers indenter [compare eqns (2.35) and (2.36) with eqns (2.29) and (2.32)]. As one might readily expect, the resemblance occurs as well for equations denoting the average contact pressure under the Berkovich indenter, derived for elastic [eqn (2.37)] and elasto-plastic [eqn (2.38)] solutions [71]:

$$p_{av} = 0.2201\left(1 - 0.21\nu - 0.01\nu^2 - 0.41\nu^2\right)\frac{E}{1-\nu^2}, \qquad (2.37)$$

$$p_{av} = 0.245\sigma_y\left(1 + \frac{\sigma_u}{\sigma_Y}\right)\left(1 + \ln\frac{E\tan 24.7^\circ}{3\sigma_Y}\right), \qquad (2.38)$$

which correspond to eqns (2.37) and (2.38) of universal formulation concerning Vickers hardness [96]. Eqns (2.37) and (2.38) account for the pile-up effect and constitute the universal notation for Berkovich hardness. Interestingly, Larsson et al. [71] concluded that in the case of Berkovich indentation, pile-up and sinking-in effects counteract each other, and found that the plastic zone below the triangular indenter appears to be of spherical shape.

In summary, the results obtained by Giannakopoulos et al. [96] and Larsson et al. [71] established foundations for the FEM simulation of deformation and fracture induced by sharp indenters, and contributed significantly to our understanding of the mechanics of the penetration process. The approach remains legitimate for materials with pressure-independent properties, which means that it has limited validity for ceramics, as previously discussed – the problem addressed in detail by Söderlund and Rowcliffe [70].

Zeng et al. [72] introduce the general method of analyzing the experimental $P-h$ indentation data obtained by means of pointed indenters, based on the FEM procedures [71, 96] reviewed in the precedent paragraph. They

suggest separate inspection of the loading and unloading indentation cycles, and emphasize that during penetration the surface displacement occurs both inside and outside the contact boundary. According to Zeng et al. [72], the sinking-in observed during loading takes place outside the contact boundary, while the unloading is associated with curving observed inside the contact boundary. To apply the formalism of Giannakopoulos et al. [96] and Larsson et al. [71] to hard and brittle materials such as ceramics, which cannot be regarded as "Mises materials," Zeng et al. [72] introduced a surface-displacement factor ζ:

$$\varsigma = \frac{A_{ideal}}{A_{true}}, \tag{2.39}$$

where A_{ideal} and A_{true} represent the ideal (calculated) and true (real size, not available for measurement) projected contact area, respectively. The positive or negative values of the ζ factor indicate that sinking-in ($\zeta > 1$) or pileup ($\zeta < 1$) has occurred. Using the ζ factor, Zeng et al. [72] rescale the Mises elasto-plastic solution to make it applicable to ceramic materials and verify their approach for 11 different kinds of glass and ceramics. Furthermore, Zeng and Rowcliffe [103] demonstrate that their analysis applies to nanoindentation in glass, alumina, B_4C, TiB_2, WC–Co, SiC, ZrO_2, and Si_3N_4. Unfortunately, the method required several oversimplified assumptions to be used for ceramics.

A complete and 3D finite element simulation of sharp indentation in pressure-sensitive materials is offered by Giannakopoulos and Larsson [104], in 1997. The method follows the earlier procedures by the same authors [71, 96], while pressure sensitivity (a property of hard metals and ceramics) was introduced according to the classic model of pressure-sensitive flow proposed by Drucker and Prager [105]. The authors used an incremental elasto-plastic law, and obtained a solution for complete load–unload cycle, determined the contact area, average contact pressure, and estimated local mechanical fields (Misses effective stress) with their singularities near the edges of the indenter. They employed the large plastic and small elastic strain approach, as well as high and low linearly isotropic strain hardening to model the material behavior. The results of their simulation were verified for hard metals, glasses, and ceramics [104].

Giannakopoulos and Larsson [104] found that the indentation depth recovery does not result necessarily from elastic rebound, and a similar effect might be caused by phase transformation. Further, they confirmed that the initial slope of the $P-h$ indentation curve is related to the elastic properties (E, v) of the material, which are influenced by pressure sensitivity, while unaffected by strain hardening. The authors discovered that the projected true contact area at loading depends more on strain hardening than on pressure sensitivity, while the sinking-in effect increases with strain hardening and decreases with pressure sensitivity. They also proved that the $P-h$ relationship is parabolic [eqn (2.40)] for pressure-sensitive materials, similarly to earlier findings for metals by Giannakopoulos and Larsson [71, 96]:

$$P = -\int \sigma_{2j} N_j dA_c = Ch^2, \tag{2.40}$$

where A_c denotes the actual contact area, $\boldsymbol{N}_j$ stands for an inward vector normal to the surface within the contact area, and C is a constant. The authors conclude that the total energy U_r expended for indentation depends on the maximum indentation load $P_{\max}^{3/2}$:

$$U_r = \int_0^{h_{\max}} Pdh = \frac{P_{\max}^{3/2}}{3C^{1/2}}, \tag{2.41}$$

while the general formula for the average contact pressure p_{av} (equivalent to the Meyer's hardness) for pressure-sensitive materials reads:

$$p_{av} = 0.77\frac{3(1+q)(\sigma_Y + qp_0)}{3+q}\left(\frac{(3+q)E}{3(1+\nu)(\sigma_Y + qp_0)}\right)^{\frac{2q}{3(1+q)}} - (\sigma_Y + qp_0), \tag{2.42}$$

where a_0 is the material constant that represents pressure sensitivity ($q = \frac{3a_o}{3-a_o}$), and p_o is a far-field hydrostatic compression.

Furthermore, Giannakopoulos and Larsson [104] indicate that the so-called "inverse problem" for ceramics indentation (determination of the material properties based on indentation data and FEM simulation) entails serious difficulties because of the combination of strain hardening and pressure-sensitivity effects, in contrast to the less-complicated case of metal indentation. An interesting example of the solution to the indentation inverse problem was presented by Nowak et al. [94] who performed a finite element simulation of indentation in ultrahard HfN thin films deposited on a silicon substrate, and were able to determine mechanical characteristics of the top film (HfN), substrate (silicon wafer), as well as the amorphous silicon interlayer formed after bombardment of the HfN–silicon system with energetic Au ions.

Furthermore, their FEM analysis of indentation into specific crystallographic planes of resulted in solution of the long-standing dilemma concerning mechanism of surface deformation of the Al_2O_3 crystal and oxide ceramics [95]. The latter work [95] dealt with full 3D FEM modeling of the anisotropic spherical elastic contact.

Recent Applications of the FEM Procedure to the Hardness Test. There has been a recent increase in the number of studies that apply FEM simulation to indentation problems (refer to the reviews of bibliography by Mackerle [106–108]). Such approaches contribute significantly to the clarification of the effect of tip roundness or truncation on nanoindentation data [35, 109, 110]. They also make it possible to determine the initial yield pressure, surface displacements outside the indentations, the indentation stress–strain relationship, as well as to identify the shear component of the stress field as the driving force for the deformation of ceramics [111]. Furthermore, the FEM procedure enables the resolution of the indentation depth at which plastic deformation starts [112]. It provides the correction that successfully annihilates the overestimation of hardness and the

elastic modulus when pile-up effect appears to be an important factor [71, 113].

A new insight into the process of the plastic zone formation in FCC crystals during surface deformation was achieved using a simulation of hardness experiments combined with TEM observations [114, 115]. Tadmor et al. [116] provide an impressive study of large-scale atomic resolution calculations concerning indentation. On the basis of the FEM calculations, they were able to estimate the Peierls stress and the density of mobile dislocations within the crystal.

Finally, the FEM simulation by Suresh, Giannakopoulos, and coworkers [117–119] resulted in a general theory of indentation of piezoelectric solids and clarified the evolution of the surface residual stress and deformation field in compositionally graded materials. Based on these studies, Nakamura et al. [120] proposed a new measurement procedure using inverse analysis of nanoindentation in nonlinear functionally graded or layered materials. All this indicates that nowadays the finite element calculations prove quite useful in the analysis of nanoindentation data, both from the scientific and practical point of view, with a recent development of *nano*indentation procedure.

2.2.4. Additional Recommended Methods of Hardness Evaluation

Swain and coworkers [48, 59–66] argue that the measurement of hardness with small radius R spherical indenters is the most convenient and effective method. The authors emphasize the simplicity of estimating the mean pressure p_{av} under the spherical indenter, using the distance of elastic approach δ [eqn (2.11)] and its relationship to the contact area [eqn (2.12)]. Thus, according to Swain et al. [59, 60], hardness H, which equals mean contact pressure (p_{av}), might be readily assessed:

$$H = p_{av} = \frac{P}{\pi a^2} = \frac{P}{\pi \delta R}\ , \tag{2.43}$$

while the contact radius a, in the case of elastic–plastic deformation under a spherical indenter, reads [48]:

$$a = \sqrt{2Rh_p - h_p^2} \tag{2.44}$$

where h_p stands for plastic penetration depth.

Swain et al. [60] attempt to estimate the pile-up effect and propose a procedure for correcting hardness data. In cases when pile-up aftermath is negligible, substitution of the value of a from eqn (2.44) into eqn (2.43) provides an adequate estimation of the contact pressure.

An alternative method of hardness evaluation was proposed by Page and associates [73, 121, 122], who explore the $P-S^2$ and $P-h^2$ relationships that hold for the measured load P, depth h, and contact stiffness S. Taking advantage of eqn (2.2), the authors determined the P/S^2 ratio, and subsequently, the hardness value H [121]:

$$\frac{P}{S^2} = \frac{\pi}{4E_{eff}^2}\frac{P}{A} = \frac{\pi}{4E_{eff}^2}H\,. \tag{2.45}$$

Alternatively, hardness can be evaluated from eqns (2.16) and (2.17) when the effective Young's modulus of the examined material is known [70]. Page et al. [122, 123] claim that the combined analysis of the $P-h$, $P-S^2$, and $P-h^2$ data appears very efficient for bulk materials and hard coatings. This prompts the authors to suggest that their approach might be considered an alternative to the FEM simulation–based methods.

The original approach to nanohardness measurements was provided by Gerberich et al. [68] (refer to Section 2.1.4.4), who base in large part on their own experience of the deformation of metallic crystals under milinewton contacts [98, 124–126], examination of thin films by wedge indentation [127], and dislocation mechanisms involved in nanoindentation process [128, 129]. The elastic–plastic formulation used by the authors enabled them to determine contact displacements and radius of the zone [eqn (2.22)], and thereby to estimate nanohardness. The proposed algorithm applicable to very shallow sharp indentations was treated in terms of a spherical contact owing to the significant rounding of any sharp tip.

Gerberich et al. [68, 128–131] demonstrate the way in which their model clarifies nonlinear deformation mechanisms associated with sudden depth excursions observed during nanoindentation of metals, or an effect of surface roughness on ultrashallow indentation measurements [68]. Furthermore, the latter model by Gerberich et al. [128–130], based on the activation of dislocation multiplication sources, enabled them to explain the dilemma in materials science: the yield initiation during indentation process. Despite its universality claimed by Bahr and Gerberich [130, 131], the latter model is not suitable when twinning or phase transformation occurs in early stages of deformation, an issue pointed out by Nowak et al. [132] already in 1999 and accepted recently as a major shift in the approach to incipient plasticity [22, 23, 38].

Moreover, Tymiak et al. [133] provide theoretical considerations followed by measurements of plastic strain and strain gradients for shallow indentations and discuss indentation size effect in metallic crystals in terms of gradient plasticity, the research that is an extension of the approach by Gerberich et al. [128–131].

3. ATOMISTIC SIMULATION OF THE NANOINDENTATION PROCESS

The recent development in nanoindentation technique targets the continuous decrease in indentation depths and diminishing contact area, and consequently, this method became an exclusive tool to examine the mechanical properties of materials in nanolevel [134]. Since none of the experimental techniques is universal, they usually require verification by supplementary approaches. In the case of nanoindentation experiments, the combination with transition electron microscopy [135] or simultaneous measurements of the contact resistance [23, 136] proved to be successful and resulted in deeper understanding of the phenomena which occur under the acting tip. Very tiny contacts realized by extremely sharp indenters – such as cube-corner tip frequently used for nanostructures – preclude the possibility of the nanoindentation modeling by means of an FEM procedure (refer to Sections 2.1.4.4, and 2.2.3.4 in

this review). The proper approach to this kind of problems stems from the atomistic considerations: either quantum (*ab initio*) or classical MD calculations. Indeed, the simulations that employ molecular dynamics (MD) proved to be efficient in these cases and provide a new insight into a variety of physical phenomena including incipient plasticity or indentation-induced phase transformations. Interestingly, MD calculations gained recently common recognition in materials science, which inevitably tends toward nanotechnology and nanostructured materials. The recent research concerning adhesion and fracture of gold monocrystal [137] or generation of initial defects and pile-up formation during indentation of fcc-silver and bcc-iron crystals [138] serves as the perfect example of the recent trend.

3.1. MD Simulation of Nanoindentation-Induced Phenomena

In the atomistic simulations the physical properties of the system – understood as a consistent cluster of atoms – appear naturally as a consequence of interatomic interactions, modeled in such a way that they mimic reality. Newton's equations of motion for multiparticle system [139] form a common background of the so-called "classical MD". However, this procedure requires the particular numerical algorithm (a simplectic integrator) that makes it possible to determine, stepwise, the atomic positions until the entire cluster is settled on.

Several integration methods nowadays are in use, see, for example, leap-frog routine in a Verlet scheme [140] and its modifications. In order to keep our cluster within precisely defined conditions, the thermodynamic ensemble should be applied, for example – the isothermal-isobaric ensemble with simultaneous scaling of atom's velocities and coordinates [141, 142].

The physical properties of the simulated system are modeled using the forces (F) acting between the atoms, and derived from the potential energy function V according to a well-known procedure:

$$\vec{F} = -\nabla V\left(\vec{r}\right). \tag{3.1}$$

In classical type simulations, atoms are treated as point-like centers that interact through many-body potential. Generally, the pairwise potentials do not work well for solid state. The Lenard-Jones potential, for example, imposes Cauchy relationship between the elastic constants ($C_{12} = C_{44}$), which is not correct for most of the metals and semiconductors. The distinct directionality of covalent bonding in semiconducting crystals can be well reproduced using three-body Stilinger–Weber [143] or bond-order potentials introduced by Tersoff [144] and Brenner [145]. Moreover, the variety of many-body potentials including the one by Finnis–Sinclare [146] as well as this based on embedded atom method (EAM) [147] is nowadays in use for metals.

The recent development of indentation technique toward very low loads and the penetration depth forced researchers to apply MD calculations to analyze, clarify, and predict the surface nanoscale deformation. However, the usage of the MD method for simulations of nanoindentation has serious limitations associated with the required extensive computer calculation time. The running time in the simulated system does not usually exceed a few picoseconds [148], and consequently, the speed of the modeled penetration process is very high, for example, in the case of silicon nitride surface deformation, the simulated tip velocity was of 100 m s^{-1} in contrast to the rate of 25 μm s^{-1} used in the experiments [149]. Despite the obvious discrepancy, the MD simulations provide reasonable results, since the simulated indentation speed is still lower than the sound velocity, which ensures that the system can dissipate reflected acoustic waves that accompany indenter motion (the sound velocity in Si_3N_4 ~7000 ms^{-1} [149]).

The other limitation of simulations is associated with the cluster size that can be considered during the MD calculations. One has to impose the artificial boundary conditions in the case of small clusters, something what may result in confusing data that would lead to errorneous claims concerning physical phenomena that occur in the stressed zone [150].

3.2. Incipient Plasticity of Crystals

MD simulation of nanoindentation in crystal structure recently became frequently explored to study the onset of irreversible deformation that terminates elastic behavior called the "incipient plasticity"[151]. The origin of such a phenomenon is vigorously investigated [151–160] owing to its interesting nature that constitutes one of the principal problems in Materials Science. Furthermore, the above-mentioned issue has bearings on technological aspects related to the quality of the contemporary electronic and optoelectronic heterostructures.

As early as in 1997, it has already been recognized that the $P-h$ curves registered during initial stages of nanoindentation in metals display the singularity – the pop-in event, which reflects sudden depth excursion of the loaded tip into the investigated crystal surface (refer to Fig. 17). This effect was explained so far in terms of the dislocation nucleation and their subsequent movement in the crystal volume affected by the indenter [129, 134].

The continuum theory of elasticity predicts that a maximum-resolved shear stress – the empirical criterion for dislocation nucleation in the perfect crystalline volume – should appear right under the tip on the indenter axis as well on specific slip planes inclined 45°. In contrast to this scenario, the MD simulations of the nanoindentation of the Au(1 1 1) by rigid-sphere indenter challenge prediction of the elastic theory by demonstrating that two partial dislocation loops with mirror symmetry beneath the surface located on the {1 1 1} planes are homogenously generated during the initial part of the nanoindentation [161].

The stress threshold necessary to start the plastic deformation is affected (decreased) by the presence of the existence of surface imperfections, namely, surface steps [162]. This phenomenon has successfully been modeled by Zimmerman et al. [163] using the MD approach (refer to Fig. 18).

It is worth noting that Burgers vector of dislocations was determined in the way proposed in Zimmerman's slip-vector method [163]. Indeed, the introduced new parameter "the slip vector" is calculated for every atom within the considered cluster and it generally possesses a large magnitude for any inhomogenous deformation. The slip-vector analysis appears to be quite universal and consistent compared

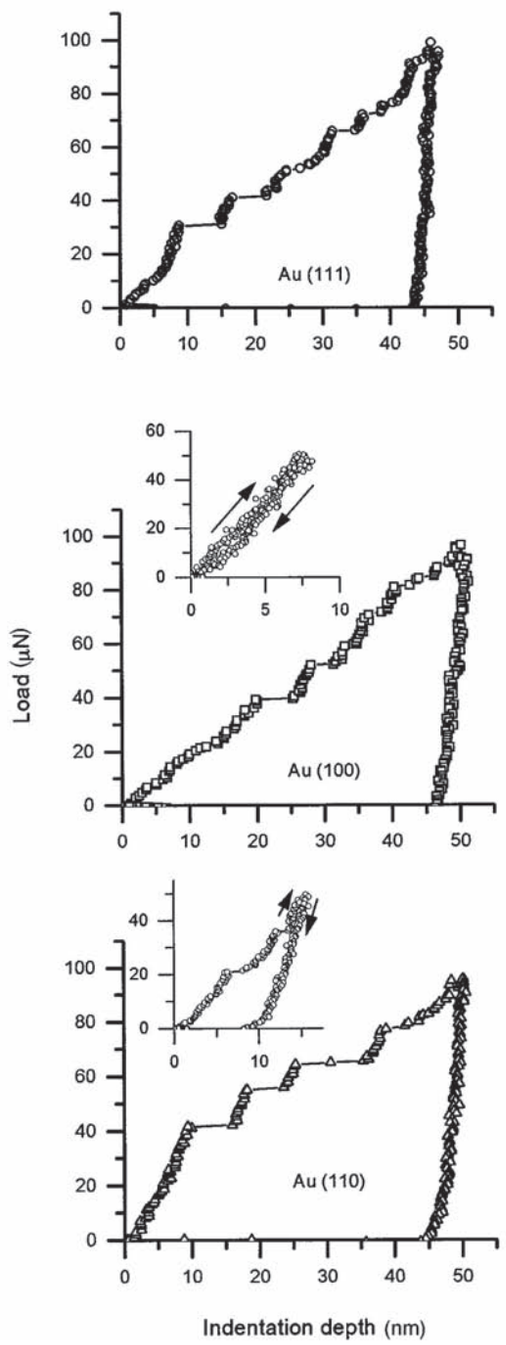

Figure 17. Typical load–displacement curves for Au single crystals (1 1 1), (1 0 0), and (1 1 0). The inset of Au(1 0 0) is a load–displacement curve for Au(1 0 0) showing elastic loading and unloading just prior to the first displacement excursion. The inset of Au(1 1 0) is a load–displacement curve for Au(1 1 0) showing elastic loading and unloading just prior to the next displacement excursion. Reprinted with permission from [151], S. G. Corcoran et al., *Phys. Rev. B 55*, R16057 (1997). © 1997, American Physical Society.

to the other known procedures of dislocation detection in a deformed atomistic structure, for example, the centrosymmetry parameter method [161] restricted merely to the crystals with the center of symmetry. The search for the structure defects can also be accomplished by employing a

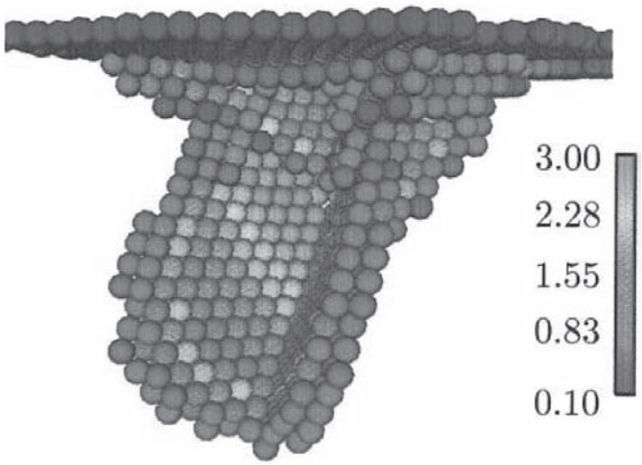

Figure 18. Dislocation loops nucleated during MD-simulated nanoindentation-induced surface deformation of Au(1 1 1) crystal in the region located far from the existing surface steps. The color of the atoms is defined by the magnitude of the slip vector. Reprinted with permission from [163], J. A. Zimmerman et al., *Phys. Rev. Lett*. 87, 165507 (2001). © 2001, American Physical Society.

shortest-path ring statistics as demonstrated by Szlufarska et al. for ceramic crystal of SiC [164].

The illustration of the variation of atomistic structure at the early stages of irreversible deformation was provided by van Vliet et al. [165] whose nanoscale experiments agreed qualitatively with the output of the MD simulations. The authors concentrated on indentation in various fcc metals with initially low-defect density and concluded that the stress level prior to the first discontinuity on the *P-h* curve is sufficient to induce homogenous nucleation of dislocations. This was supported by MD simulations performed for Cu and Al. In contrast to these early works [150, 152, 154, 161, 165], Schuh et al. [155] presented more recently the statistical approach to the nanoindentation experiments, which advocates the freshly revised scenario, namely, the onset of metal plasticity owing to heterogeneous defect nucleation.

Hence, it becomes increasingly clear that the indentation experiments and their results depend on the dimensions of the studied materials. This was demonstrated for thin film and patterned lines of aluminum deposited on silicon substrates [166]. Both the experimental results and the output of the MD simulations proved that the elastic response of materials is usually size independent, which contrasts with the plastic behavior. The plastic deformation is associated with the size effect that depends on the geometrical constrains, for example, thin films are usually harder than the patterned lines [166]. This phenomenon is governed by the subtle interaction between the stress field imposed by the indenter and the stress field caused by the presence of dislocations.

In sum, one can conclude that at the present stage of the development of the field of nanoindentation, MD results point toward homogenous nucleation of dislocations to be responsible for the pop-in effect, while the experiments indicate the heterogeneous one.

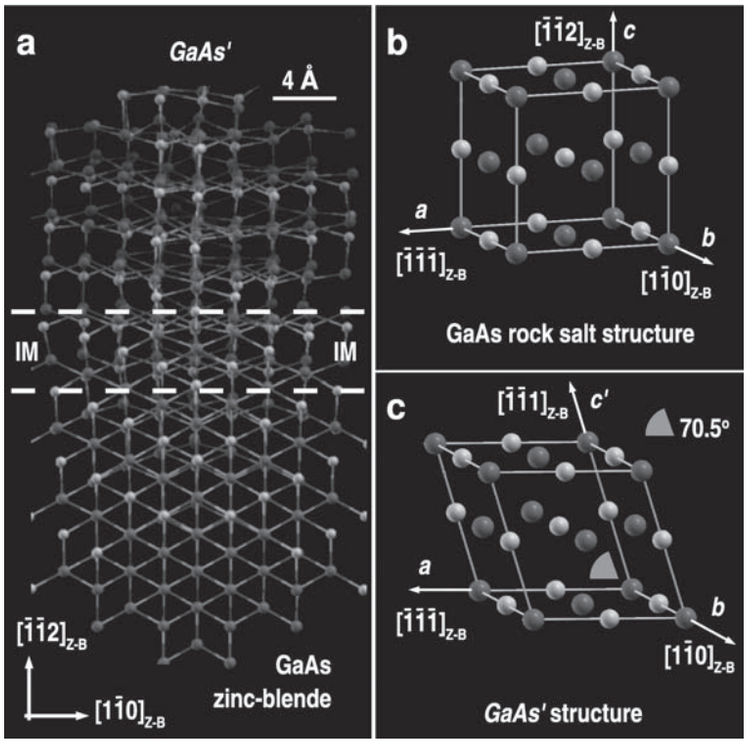

Figure 19. Direct visualization of the atomic positions determined for a nanoindented GaAs crystal viewed along the [1 1 1] direction (a), the orientation of the GaAs rocksalt unit cell with respect to the zinc-blende lattice (b), and the GaAs rocksalt-like structure generated under the acting indenter (c). IM defines an intermediate region with a mixed arrangement of Ga (magenta) and As (yellow) atoms [22]. Reprinted with permission from [22], D. Chrobak et al., *Phys. Rev. Lett.* 98, 045502 (2007). © 2007, American Physical Society.

3.3. Pressure-Induced Phase Transformation in Nanoscale Deformation Experiments

Despite the dislocation–nucleation scenario becoming already widely accepted clarification of the pop-in event origin both for the metals [151–155] as well as for ceramic [156, 164] and semiconducting [167–170] crystals, the fresh results of the atomistic simulation of the processes that occur in very high pressure induced by an indenter as well as recent high-precision experiments lead us to a conclusion that it must not always be true. In other words – there is certainly a large group of materials for which the incipient plasticity (understood as the termination of elastic behavior) is not associated with the dislocations at all. The confusion started with the MD simulation of surface deformation of the (1 0 0)GaAs crystal by Chrobak, Nordlund, and Nowak [22, 171] who claim that in this particular crystal the incipient plasticity reflects nondislocation process, namely, the indentation-induced phase transformation from zinc blende to rocksalt GaAs structure (Fig. 19). The above-described state of affairs has been recently verified experimentally by in situ electrical measurements that provide the indirect proof of the discovered phase transition [23], while nondislocation incipient plasticity was also noticed in silicon nanoparticles by Valentini et al. [172].

In the case of GaAs semiconductor compound, the stress required for dislocation nucleation t_R equals 6 GPa [167], which yields mean hydrostatic pressure under tip p_m ($p_m = t_R/0.465 =$ 12.9 GPa) that is sufficient to start transformation in GaAs zinc-blende structure. Indeed, it is well known from earlier anvil-cell experiments [173] that zinc-blende phase transforms into orthorhombic rocksalt under the hydrostatic pressure of ~13 GPa.

The reversible character of the discovered phase transformation explains why this phenomenon was never reported concerning nanoindentation in GaAs so far. However, one should notice that the results of indentation tests reported by Li et al. [174] revealed the traces of amorphous GaAs left after unloading indentation cycle. These amorphous remains seem to be closely linked to the transition we discuss here. According to the earlier anvil-cell experiments – during high-speed decompression the orthorhombic rocksalt-like GaAs becomes amorphous [173], which resembles the situation during nanoindentation unloading cycle. Hence, one may consider the detected amorphization as an indirect proof of the nanoindentation-induced phase transformation from GaAs zinc blend to rocksalt-like structure, which coincides with our recent in situ resistivity measurements in nanoindented GaAs [23].

Our MD-based considerations demonstrate the indicated transformation (GaAs zinc blende → GaAs rocksalt-like structure) results in a singularity in the load–depth $P-h$ curve commonly defined as initial pop-in [171], which calls for the revision of the widely exercised so far dislocation–nucleation concept of incipient plasticity of crystalline solids.

The phase transformations during nanoindentation were observed in many occasions for crystalline silicon, although in that case the loading part of $P-h$ curve does not exhibit pop-in events. For instance, the ex situ TEM (transition electron microscopy) examinations of residual impression show the existence of the metallic beta-Sn (Si-II) phase of silicon [19, 175]. More recently

the metalization of nanoindented silicon was observed by in situ electrical measurements [176]. In contrast to metals, the silicon exhibits during nanoindentation the singularity ("pop out") in the unloading cycle of the $P-h$ curve associated with a sudden volume increase related – according to Domnich et al. [177] – to the formation of metastable Si-XII and Si-III silicon phases.

It is worth emphasizing that the indentation-induced phase transformations in silicon are well documented [176–178] and intensely studied with the aid of MD [178]. The transition from diamond structure (Si-I) to body-centered tetragonal form (Si-II) that occurs during loading cycle was simulated by Cheong et al. [178], who attributed this event to the flattening of the tetrahedron structure in diamond-cubic silicon. Further, it was found that the high-pressure phase of silicon becomes amorphous during unloading [178], while the interesting combination of MD and FEM methods provided completely new insight into the effect of the indenter shape on the silicon-mechanical response [179]. The latter supports the experimentally derived conclusion concerning the marked stress dependence of the microstructure of silicon crystal [180].

Besides the discussed crystalline-to-crystalline phase transformation, the amorphous silicon appears sometimes during loading cycle. Kim et al. [181] investigated the effect of crystal orientation on the microscopic aspects of the phase transformation in silicon, while the instability of the amorphous Si was studied by Izumi et al. [182], and both the teams concluded with Si amorphization. They estimated critical nucleus shape as nearly spherical and size to about 30-50 atoms, which is in agreement with the experimental data [183].

In contrast to the above-referred studies, Szlufarska et al. [164] proposed the original atomistic mechanisms responsible for nanoindentation-induced amorphization in silicon carbide. They, however, did not concentrate on the phase transition as a reason of incipient plasticity, similarly to Chrobak, Nordlund, and Nowak [22, 171]. Instead, their plastic deformation of the SiC ceramic crystal was understood as a combination of two processes, namely, the nucleation of dislocations loops and the transition from crystalline to amorphous phase attributed to the coalescence of earlier generated linear defects (dislocation loops) [164].

In conclusion, it is worthy to emphasize that the problem of incipient plasticity and, especially, phase transformation–induced onset of irreversible deformation is very fresh and awaits final experimental verification. The latter is not an easy task, since the volume of the material transformed under tip is so small that it precludes any diffraction investigations. The examination such as in situ electrical measurements [23] or fresh nanoRaman experiments [28] rise hope that this problem would also be solved in the near future.

4. NANOINDENTATION OF CERAMICS, SEMICONDUCTORS, AND SUPERCONDUCTORS

4.1. Controversial Issues Concerning Nanoindentation

The controversial issues in nanoindentation concern both Young's modulus and hardness determination. The measurements of the former parameter are compromised by the structural changes induced under the acting tip, which virtually make impossible to derive elastic characteristics from unloading cycle as proposed in commonly accepted methods of Oliver and Pharr [36] or Field and Swain [60, 61]. Our recent finding [38] that nanoindentation is regarded as nondestructive testing method, while it is not so, represents a critical step in reconciling the dominant experimental, analytical, and FEM-based analysis methods with the results of optimized experiments in which both a deformable indenter and pop-in events are present.

Although hardness was found related to the flow stress σ_Y of the investigated material [see eqns (1.2), (2.31), (2.38), and (2.42)], which is commonly used in engineering, the definition of hardness lacks physical bases. A critical review of Meyer's hardness as a measure of plasticity was offered by Sakai [116], who discovered that hardness value is affected by both plastic and elastic properties of the indented material. This new conclusion was supported by the results of the numerical simulations [eqns (2.31), (2.38), and (2.42)], which indicated that the average contact pressure ($p_{av} = H$) depends on the plastic and elastic characteristics of the tested solid.

Despite the drawbacks related to the definition of hardness, researchers have attempted to formulate an accurate evaluation of the hardness value from the measured $P-h$ data (see Section 2), rather than searching for a new pertinent parameter that may in truth represent the indentation resistance of the tested solid. An exception is the study by Sakai and Nowak [44, 46] and the considerations by Rother and coworkers [185–191]. In spite of different philosophies and methodologies proposed by these two research teams, both approaches take account of indentation energy consumed by the deformed solid surface, which contrasts with the analyses of indentation data by other authors (see Section 2).

Sakai and Nowak proposed a new concept of hardness, based on the amount of the energy irreversibly consumed to create a unit volume of indentation impression in a perfectly plastic material, in 1992 [44], while its complete version was published by Sakai in 1993 [45]. As emphasized by Söderlund and Rowcliffe [70], the energy-based approach (energy principle of indentation, EPI), where both loading and unloading indentation cycles are analyzed, is a promising way of evaluating nanoindentation data.

Thus, the present chapter is devoted to the EPI method [44–46], followed by the examples of indentation deformation of a variety of solids including highly anisotropic crystals, nanocrystalline thin films, and solid surfaces modified by energetic ion bombardment. It begins, however, with a short review of the alternative indentation energy approach proposed by Rother and Dietrich [185], which targets the indentation deformation of film–substrate systems. These considerations were independent of EPI, since the authors were not aware of the earlier studies by Sakai and Nowak [44–46] when they prepared their manuscript.

4.2. The Energy-Related Differential Load Feed Analysis of Hardness Measurements

Rother and Dietrich [185] analyzed the total deformation energy consumed for formation and propagation of the

deformation zone created in a solid directly under an acting rigid indenter. Hence, they assumed that the total deformation energy U_T is expended for densification of the indented material (U_1), shear displacements within the boundary of the deformation zone (U_2), and interface formation caused by grain boundary cracking (U_3):

$$U_T = U_1 + U_2 + U_3 = k_1 u_1 h^3 + k_2 u_2 h^2 + k_3 u_3 h^2 N = \tilde{E}_1 h^3 + \tilde{E}_2 h^2 + \tilde{E}_3 h^2 N \quad , \qquad (4.1)$$

where k_i (i = *1*, *2,* 3) are shape factors characteristic of a particular indenter geometry, u_1 denotes mean energy densities in the deformation zone, while E_1 defines specific energies and N stands for the number of cracked grain boundaries. Based on an assumption that increase of N appears to be proportional to the relative stress in the indented material, the authors derived the final formula for U_T [185]:

$$U_T = \tilde{E}_1 h^3 + \tilde{E}_2 h^2 \Big|_{h \to \Delta \tilde{h}_1} + \tilde{E}_2 h^2 \Big|_{h \to \Delta \tilde{h}_2} + \tilde{E}_3 h^2 \left(1 + \alpha \ln \frac{h}{h_o} \right) \Big|_{h \to \Delta \tilde{h}_3} \quad , \qquad (4.2)$$

and consequently:

$$\frac{d^2 U_T}{dh^2} = 6E_1 h + 2E_2 \Big|_{h \to \Delta h_1} + 2E_2 \Big|_{h \to \Delta h_2} + 2E_3 \left(1 + \alpha \ln \frac{h}{h_o} \right) \Big|_{h \to \Delta h_3} + 3E_3 \alpha \quad , \qquad (4.3)$$

where h_o defines the initial penetration depth, ∇ is a constant, while h_1, h_2, and h_3 are the components of the indentation depth associated with densification, shear displacement, and boundary cracking, respectively.

Furthermore, Rother and Dietrich [185] considered the total energy U provided by the penetrating indenter to be expended for deformation (U_T) and friction energy U_F that appears to be proportional to the indenter shift h, friction coefficient ρ, and normal force F_n:

$$U = \int P dh = U_T + U_F = U_T + \rho F_n h \qquad (4.4)$$

They found that the second derivative of U_T could be readily determined from indentation *P–h* data according to the simple relationship:

$$\frac{d^2 U}{dh^2} = \frac{d^2 U_T}{dh^2} = \frac{dP}{dh} \quad , \qquad (4.5)$$

which in turn makes it possible to explore the linear ranges of the dependences $\frac{d^2 U_T}{dh^2} - h$ and $\frac{d^2 U_T}{dh^2} - \ln h$ in eqn (4.3). Such an analysis of $\frac{dP}{dh} - h$ plots allows one to calculate the specific energies E_i (i = 1, 2, 3) of the different deformation processes and direct correlation to conventional hardness data. The "load feed analysis method" by Rother and Dietrich was scrutinized for depth-sensing Vickers indentation of silicon, glass, glazed Al_2O_3, hardened high-speed steel [185], TiN [186], acryl glass, color paint, India rubber [187], as well as polypropylene coatings [188].

Furthermore, Rother et al. [186, 188–191] claimed that their approach allows one to quantify the adhesion of a coating and permits the separation of coating from substrate properties. Consequently, their analysis of the first derivative of the experimentally recorded indentation load, d*P*/d*h,* proved successful in clarifying the indentation process in complicated structures.

4.3. The EPI: A New Concept of Hardness

Starting with the idea of hardness being a measure of material's resistance against plastic deformation induced by a rigid indenter, the EPI approach is based on the assumption that hardness should be directly related to the energy *U*r expended for irreversible deformation of the tested solid [44, 45]. Since the energy U_r is represented by the area bounded by the loading and unloading curves, it can be readily determined from the *P–h* indentation data (see Fig. 20). For a perfectly elastic contact, the energy *U*r equals zero (see Fig. 20(a)), while it attains a maximum for an indentation in perfectly plastic material (Fig. 20(b)). The latter *P–h* curve is typical for most metals for which elastic recovery is negligible:

$$h_r \approx h_p \text{ , and } h_e << h_r \quad (h_e \approx 0 \text{ }), \qquad (4.6)$$

while Figures 20(a) and 20(c) are illustrative of ceramics that exhibit appreciable elastic recovery of the indent (h_e). Usually, one deals with a combined elasto-plastic response (Fig. 20(c)) , while perfectly elastic behavior (Fig. 20(a)) is observed for hard surfaces, particularly if spherical indenters are used (see, e.g. Ref. [27]).

To calculate the energy *U*r expended for the irreversible surface deformation, one should determine the shape of the *P–h* curve for both the loading and the unloading cycle. The simple geometrical considerations presented by Sakai and Nowak [44] for a cone tip with the semiapex angle ψ yield the current indentation depth h and the mean contact pressure p at the contact area with the radius of a (see Fig. 21):

$$h = \gamma a \cot \psi \quad , \qquad (4.7)$$

$$p = \frac{P}{\alpha_o a^2} \quad , \qquad (4.8)$$

where the geometrical factors γ and α_0 account for surface deflection and shape of the indenter, respectively. The combination of eqns (4.7) and (4.8) yields the parabolic $P-h$ relationship in the case of a perfectly plastic contact:

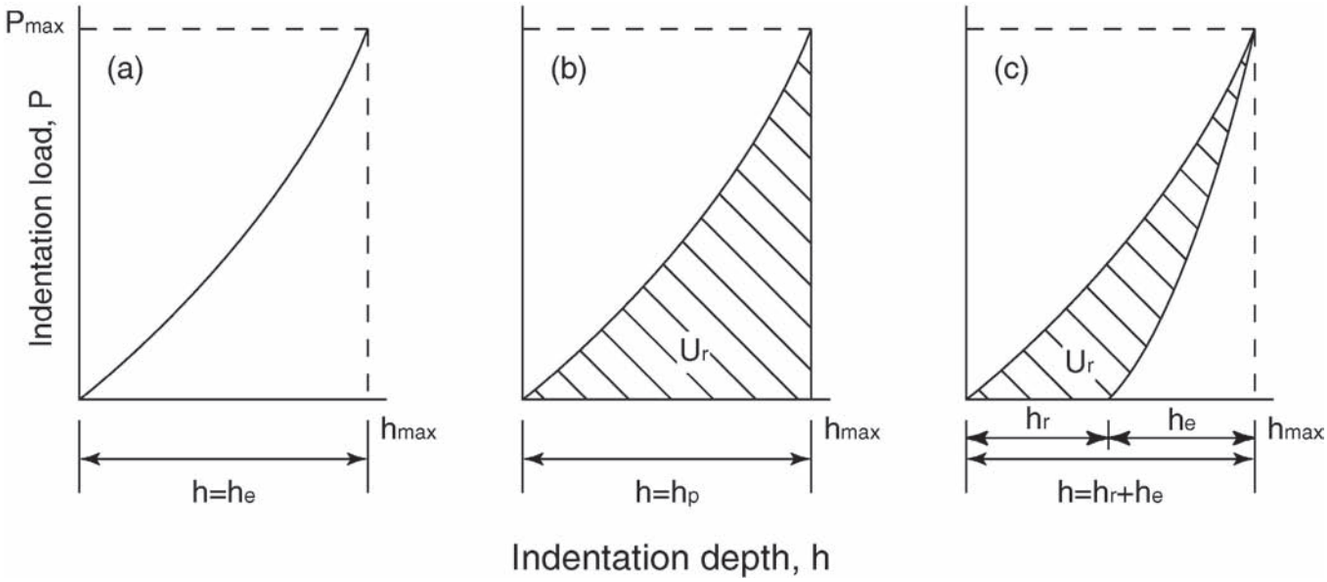

Figure 20. Typical *P–h* indentation curves for the perfectly elastic (a), fully plastic (b), and elasto-plastic material with appreciable elastic recovery (c).

$$P = A_p h_p^2 \text{ , where } A_p = H\frac{\alpha_o}{\gamma_p^2}\tan^2\psi, \tag{4.9}$$

as well as for perfectly elastic indentation, while the Sneddon's solution [54] used to the elastic contact problem yields:

$$P = A_e h_e^2 \text{ , where } .A_e = \frac{E}{2\left(1-\nu^2\right)}\frac{\alpha_o}{\gamma_e^2}\tan^2\psi \tag{4.10}$$

The simple constitutive equation for the elastic–plastic surface deformation [44]:

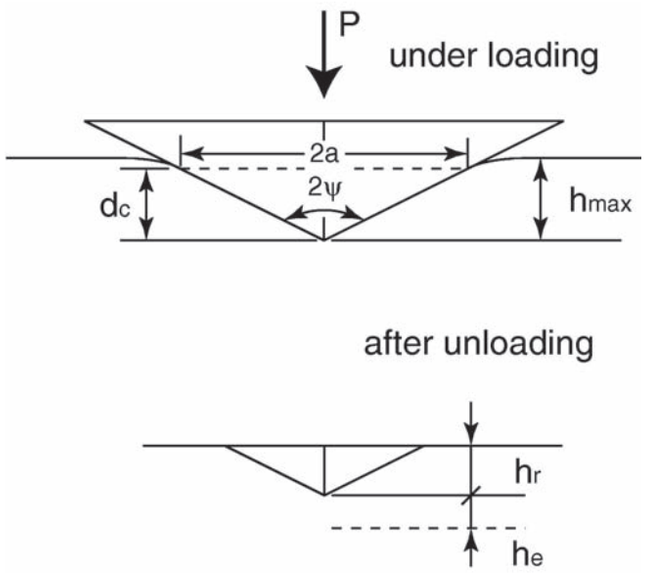

Figure 21. The schematic of the axisymmetric, sharp, and elasto-plastic indentation contact used in the EPI theory [44–46].

$$h = h_e + h_p\,, \tag{4.11}$$

combined with eqns (4.9) and (4.10) yields again the P–h^2 relationship in the case of elastic–plastic contact:

$$P = A_H h^2$$

where

$$A_H = \hat{H}\frac{\alpha_o}{\gamma_H^2}\tan^2\psi \quad , \quad \hat{H} = H_T\left(\gamma_H^{-1} + k\sqrt{\frac{H_T\left(1-\nu^2\right)}{E}}\right)^{-2} \text{ , and}$$

$$k^2 = \frac{2\gamma_e^2}{\gamma_H^2}\tan^2\psi\,. \tag{4.12}$$

The *P–h* dependence for the unloading cycle has parabolic form, as shown by Sakai and Nowak [44], who explored the compatibility of two half cycles, that is, the loading and unloading penetration depth attains the same value at the maximum load (see Fig. 20(c)):

$$A_H h^2 = A_e\left(h-h_p\right)^2 \Rightarrow P = A_e\left(h-h_r\right)^2. \tag{4.13}$$

Despite the *P−h2* formula being frequently criticized [192], Sakai and Nowak [44] found the parabolic *P−h* relationship [refer to eqns (4.9), (4.10), (4.12), and (4.13)] to hold for numerous materials [45, 46]. The authors [44, 45] calculated energy *U*r expended for irreversible deformation of the ideally plastic material (see Fig. 20(b)), by integrating eqn (4.9). Consequently, "true hardness" H_T was defined as the energy required to produce the impression with a unit volume:

$$U_r = \int_0^{h_{\max}=h_r} A_p h^2 dh = H_T V\,, \tag{4.14}$$

where $V = (1/3)\alpha_0 a^3 \cot\psi$ denotes the volume of indenter tip under the contact perimeter. A similar procedure for elastic–plastic indentation (see Fig. 20(c)) provided the U_r energy:

$$U_r = \int_0^{h_{max}} A_H h^2 dh - \int_{h_r}^{h_{max}} A_e (h - h_r)^2 dh = \Gamma_I V \ , \quad (4.15)$$

where

$$\Gamma_I = H_T \left(1 + k\sqrt{\frac{H_T\left(1-\nu^2\right)}{E}} \right)^{-3} , \quad (4.16)$$

represents the work of indentation equal to the irreversible energy necessary to create a unit volume of indentation at the maximum load P_{max}.

In spite of its simplicity, it is difficult to evaluate the hardness H_T from eqns (4.15), (4.16), or (4.12). In particular, it is hard to determine the surface deflection characterized by the geometrical factor γ in eqns (4.7), (4.9), (4.10), (4.12), and (4.16). Therefore, Sakai and Nowak [44] combined eqns (4.7), (4.12), and (4.15) to determine the relationship between U_r and the applied maximum load P_{max}:

$$U_r = \left(3\sqrt{\ }_0 \tan\psi\right)^{-1} H_T^{-\frac{1}{2}} P_{max}^{\frac{3}{2}} = C P_{max}^{\frac{3}{2}} , \quad (4.17)$$

and calculate hardness H_T from the plots U_r–$P_{max}^{3/2}$. Consequently, H_T appears as a load-independent parameter, in contrast to the conventionally measured hardness H (refer to the footnote in the page 18).

Hence, EPI provides the physically based definition of hardness H_T, which is a measure of plastic deformation in the elastic–plastic indentation process, and represents a convenient method for its evaluation. The relationships derived in 1992 within EPI coincide with the results of FEM simulation of the elasto-plastic indentation process obtained in 1996 by Giannakopoulos and Larsson [96], who confirmed the U_r–$P_{max}^{3/2}$ relationship [refer to eqn (2.41)].

Furthermore, the EPI theory was scrutinized by Sakai [45] for a number of polycrystalline materials including pure metals, namely, aluminum and copper as well as brittle ceramics: MgO, SiC, Si3N4, and glassy carbon. The experiments by Sakai cover the maximum load range from 4.9 to 98.1 N (4.9 N $\le P_{max} \le$ 9.81 N), where the data match the predicted P–h^2 relationship [eqns (4.9), (4.10), and (4.12)].

The reported agreement between the experimental indentation data and the EPI predictions prompted the present author and coworkers to apply the theory to sapphire [46, 193], superconducting $YBa_2Cu_3O_{7-\delta}$ crystals of small (approximately 500 μm) size [194], as well as the semiconducting InGaN and GaN crystals essential for optoelectronics [195–197]. Despite complicated anisotropic structures (hexagonal–rhombohedral) and complexity of the deformation phenomena in these materials, the EPI analysis appeared to represent a useful step toward clarifying their mechanical behavior.

4.4. Application of the EPI Theory to the Deformation of Crystals

4.4.1. Sharp Indentation of Single Crystals: Experimental Procedure

It has been known for a century that the hardness of crystal surfaces denoted by different crystallographic indices varies considerably [198]. Moreover, one might record hardness anisotropy on a single crystallographic plane by means of a variously oriented nonaxisymmetric indenter [199]. Hence, the nanoindentation experiments with the Berkovich tip (typical for commercially available nanoindentation depth-sensing testers) on crystal surfaces depend on the orientation of the threefold symmetry pyramid on a selected crystallographic plane. This drawback turns to an advantage, however, if the anisotropy of mechanical properties is of interest. In such a case, a precise determination of the mutual orientation of the crystal surface and the indenter is indispensable.

An example of a procedure for indentation experiments that are appropriate for single crystalline samples was described in [46, 193]. The authors mounted their sapphire crystal on a fixture that permitted rotation about the vertical axis to any desired position. Three different low-index crystallographic planes: $M = (10\bar{1}0)$, $A = (1\bar{2}10)$, and $C = (0001)$ were indented in such a way that one of the sides of triangular impression was parallel to the $\langle 1\bar{2}10 \rangle$ or $(10\bar{1}0)$ direction in the reverse (R) and normal (N) position, as shown in Figure 22. The indentation measurements by Nowak and Sakai [46, 193] were carried out on a depth-sensing tester, the Shimadzu DUH-200, with continuous monitoring of the load P and the depth h during the penetration process. The electromagnetic loading ranged from approximately 10 to 2000 mN, while the depth-measuring unit with an effective range of 0−10 μm and precision exceeding 0.1 μm used a differential transformer positioned near the indenter.

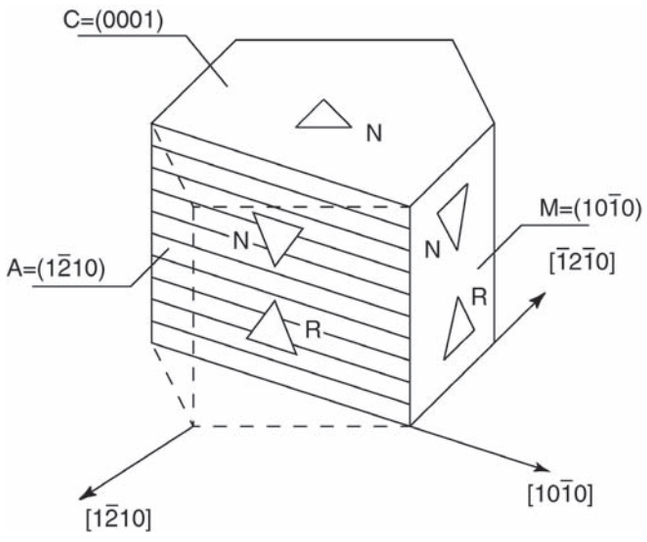

Figure 22. Orientation of the indentations in the crystallographic planes of sapphire crystal [46]. Reprinted with permission from [46], R. Nowak et al., *J. Mater. Res.* 8, 1068 (1993). © 1993, Materials Research Society.

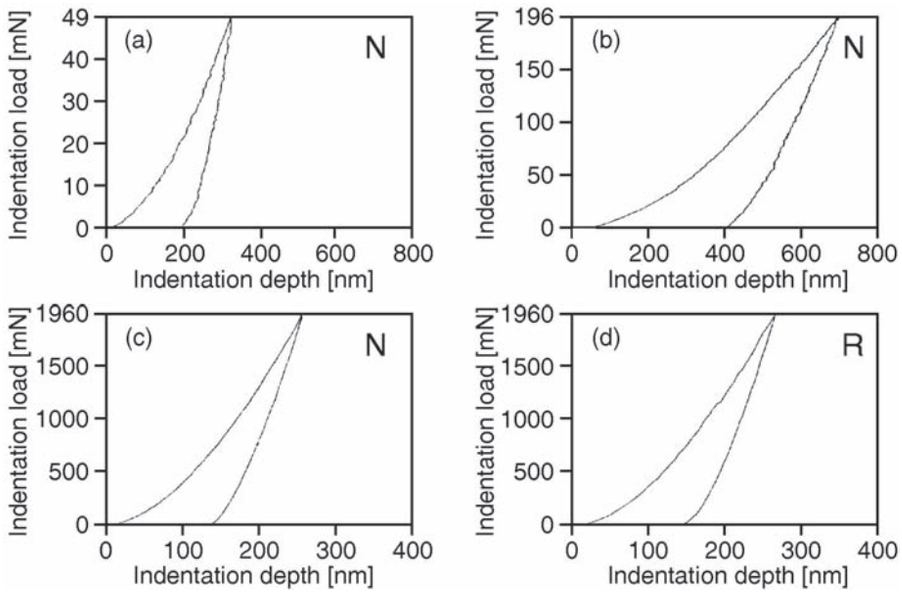

Figure 23. Typical *P–h* curves for the $(10\bar{1}0)$ plane of sapphire, obtained under the low (a), medium (b), and high (c, d) indentation loads. The indenter orientation (N, R) is marked at each figure. Reprinted with permission from [46], R. Nowak et al., J. Mater. Res. 8, 1068 (1993). © 1993, Materials Research Society.

The temperature and humidity inside the indenter wind brake were maintained rigorously constant.

In addition to the depth measurement, Nowak and Sakai [46] determined the size of the residual impression using an optical unit attached to the Shimadzu tester. Additional observations of the indents were performed by means of a microscope with Nomarski phase contrast while using special illumination of the crystal (the optical system designed to make visible the details of subsurface features) [193].

4.4.2. Hardness of Variously Oriented Sapphire Surfaces

Nowak and Sakai [46, 193] registered the *P–h* curves for the studied *A*, *C*, and *M* surfaces of sapphire crystal. Typical results obtained for the prismatic $M = \langle 10\bar{1}0 \rangle$ plane are shown by the way of example in Figure 23. The test revealed that, in spite of the apparent twofold symmetry of the $(10\bar{1}0)$ plane of sapphire, the "N"- and "R"-oriented indentations are not equivalent (compare Figs. 23(c) and 23(d)) since the characteristic discontinuities in the loading cycle of the $P-h$ data are visible only for particularly oriented (R) indenter (see Fig. 23(d)). Such an effect was observed in the case of the studied *C* and *M* orientations [193].

Furthermore, the variations of hardness H_d determined from the maximum indentation depth h_{max} (Fig. 24(a)) differed significantly from the changes in conventional hardness H_B based on the projected area of the microscopically observed impression mark (Fig. 24(b)). The confusing comparison between the H_d and H_B values (refer to Fig. 24) led the authors to believe that hardness determined in a conventional manner should not be considered a pertinent parameter for describing

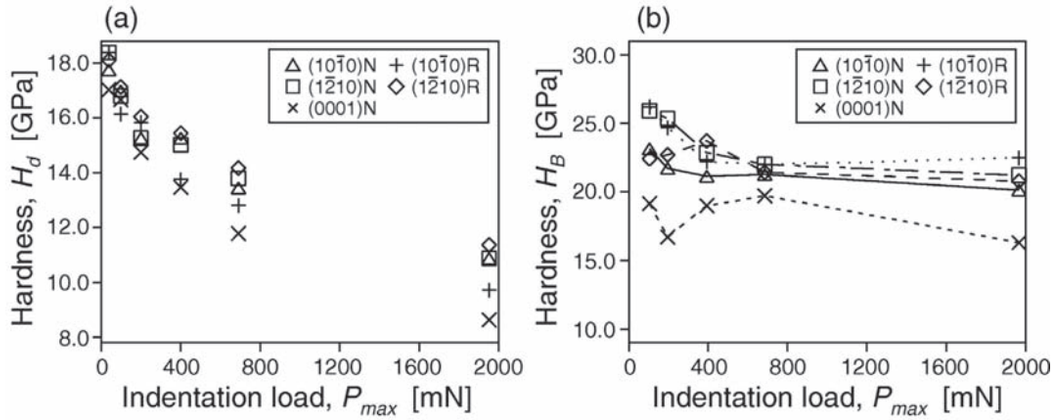

Figure 24. Conventional hardness under load H_d (a) and Berkovich hardness H_B (b) determined for various orientations of the indenter (N, R) and sapphire surface (A, C, and M). Reprinted with permission from [46], R. Nowak et al., *J. Mater. Res*. 8, 1068 (1993). © 1993, Materials Research Society.

Table 2. The true hardness H_T of various sapphire surfaces (Reprinted with permission from [46], R. Nowak et al., *J. Mater. Res.* 8, 1068 (1993). © 1993, Materials Research Society).

Indented surface	Indenter orientation	Correlation factor($\mu J\ N^{-3/2}$)	True hardness H_T(GPa)
$(1\bar{2}10)$	N	0.9991	146
$(1\bar{2}10)$	R	0.9986	147
$(10\bar{1}0)$	N	0.9984	143
$(10\bar{1}0)$	R	0.9976	126
(0001)	N	0.9960	99

the elastic–plastic behavior of a sapphire surface. Indeed, the order of H_d values from the softest to hardest found by Nowak and Sakai [46] is in the sequence of (0 0 0 1)N,$(10\bar{1}0)$ R,$(10\bar{1}0)$ N, $(1\bar{2}10)$ N, and $(1\bar{2}10)$ R, while the H_B values – Berkovich hardness based on dimension of the residual impressions – follow a different string: (0001)N, $(10\bar{1}0)$ N, $(1\bar{2}10)$ R, $(1\bar{2}10)$ N, and $(10\bar{1}0)$ R. This ambiguous situation prompted the authors to perform an independent analysis of the indentation results by using the EPI approach.

The $P-h$ data registered for sapphire crystal (Fig. 23) show negligible deviation from the linear $P-h^2$ relationship for low loads (details in [46]). This proves that within the used load interval, sapphire behaves as assumed in the energy principle of indentation [see eqns (4.12) and (4.13)]. In order to estimate the true hardness H_T of alumina crystal, Nowak and Sakai [46] plotted the relationship between the indentation energy U_r and the maximum indentation load $P_{max}^{3/2}$ for each combination of the orientations of the plane and indenter (refer to high- and low-load plots in Fig. 25). The values of H_T were calculated from the inverse slope of the linear dependence in Figure 25 and are listed in Table 2.

The significant differences between the indentation behavior for different crystal planes and the position of the Berkovich indenter are among the most important results obtained from the EPI. Surprisingly, the H_T hardness

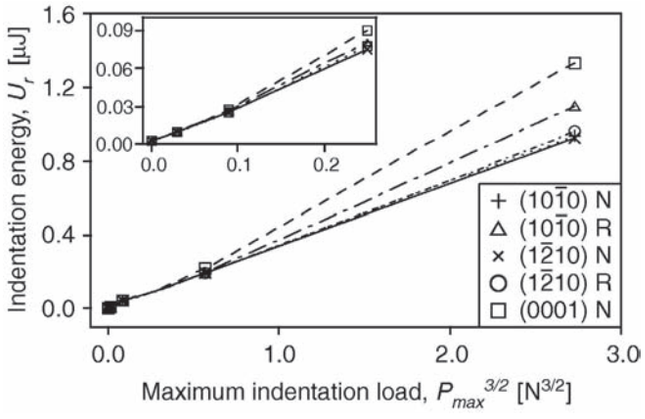

Figure 25. The U_r–$P_{max}^{3/2}$ relationship for the $M = (10\bar{1}0)$, $A = (1\bar{2}10)$, and $C = (0\,0\,0\,1)$ planes of sapphire deformed with variously oriented (N, R) Berkovich tip. Reprinted with permission from [46], R. Nowak et al., J. Mater. Res. 8, 1068 (1993). © 1993, Materials Research Society.

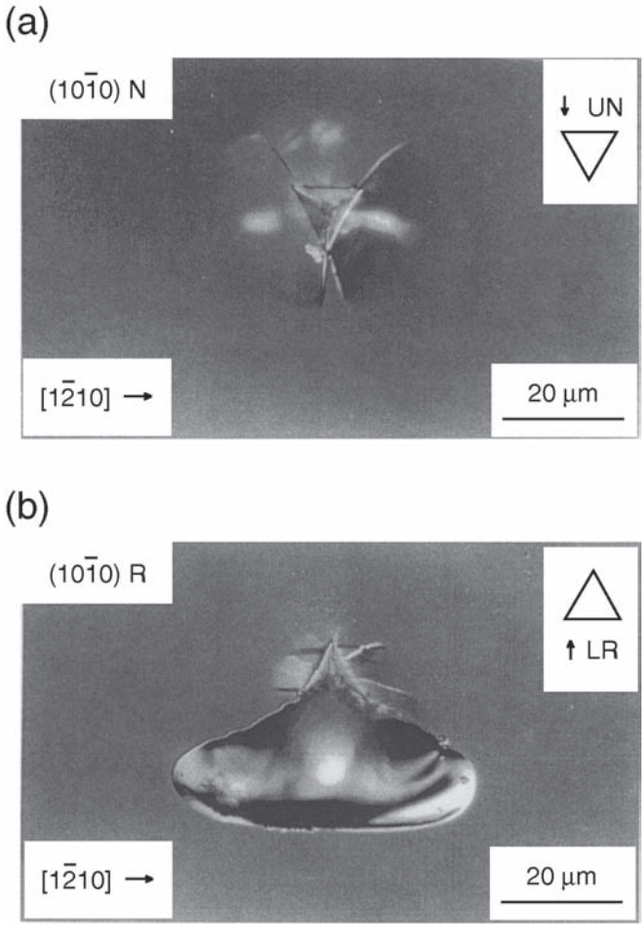

Figure 26. The surface features in the vicinity of the indentation impression with N (a) and R (b) orientations, observed on the $(10\bar{1}0)$ plane of sapphire. Reprinted with permission from [46], R. Nowak et al., *J. Mater. Res*. 8, 1068 (1993). © 1993, Materials Research Society.

measured on the plane of sapphire (see Fig. 22) is identical for both N and R orientations, while it differs significantly for N and R positions of the Berkovich tip, when probed on the plane (see Table 2 and Fig. 25). The basal plane of Al_2O_3 crystal was found softer than the surfaces with other crystallographic orientations. Finally, the applied analysis left the authors with the conclusion that the deviation from the U_r–$P_{max}^{3/2}$ linearity observed for high-indentation loads (see Fig. 25) is associated with the change of the micromechanism responsible for the indentation deformation of the crystal when higher-indentation loads are applied.

These results prompted Nowak and Sakai [46] to investigate the micromechanisms of surface deformation in order to clarify the observed anomalies. Inspection of the impressions on the plane revealed surface features around the "R indent" that were markedly different from those observed for the "N orientation" (compare Figs. 26(a) nd (b)). The deformation in the vicinity of the N impression seems to be largely elastic (Fig. 26(a)), in contrast to the R indent, which is accompanied by a complicated defect pattern which contains a large lateral crack extended near the particular facet (LR – the lower facet of the R orientation, see Fig. 22(b)).

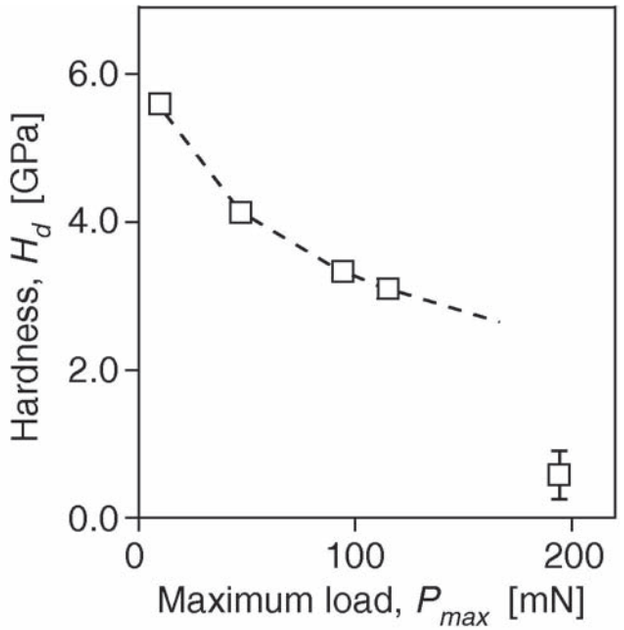

Figure 27. Conventional hardness of the (0 0 1) plane of the $YBa_2Cu_3O_{7-\delta}$ crystal. Reprinted with permission from [194], R. Nowak et al., in "Third Euro-Ceramics" (F. Duran and J. F. Fernandez, Eds.), Vol. 2, p. 571, 1993.

Nowak and Sakai [46] explained the anisotropy on the plane in terms of dislocation activity, that is, considering slip and twinning systems that may contribute to the deformation. According to Daniels and Dunn [199], the ease of slip system activation under the indenter can be estimated through the calculation of the effective resolved shear stress (ERSS) values. This kind of approach to hardness anisotropy was further developed by Brookes et al. [200], Pospiech and Gryziecki [201], Armstrong and Raghuram [202], as well as by the present author [203, 204]. The calculations by Nowak and Sakai [46] indicated the maximum shear stress attained near the LR facet of indenter (Fig. 26(b)), that is, in the region where a large lateral crack is detected, implying a lower H_T for the R orientation (Table 2). This correct prediction triggered further studies of crystal deformation under Berkovich [193] and spherical [99, 132, 205–207] indenters, which are reviewed in the following sections.

4.4.3. Deformation of Superconducting $YBa_2Cu_3O_{7-\delta}$ Crystals

The mechanical properties of high-temperature superconductors are essential for their potential applications. The examination of these materials is a difficult task, since the crystals of $YBa_2Cu_3O_{7-\delta}$ are frequently available as thin films or tiny crystals. In such a case, the indentation technique appears to be the only method that allows us to examine the mechanical behavior of the material. The fracture toughness of the $YBa_2Cu_3O_x$ crystal was studied by Cook et al. [208], who used the conventional Vickers indentation. Raynes et al. [209] reported on fracture toughness and twinning of $YBa_2Cu_3O_{6-\delta}$ crystal, while the first depth-sensing experiments with $YBa_2Cu_3O_{7-\delta}$ crystals were performed by the present author and coworkers [194]. Nowak, Sakamoto, and Maruno [194] grew the crystals from the flux of mixed powders of the Y_2O_3, $BaCO_3$, and CuO. To perform the indentation examination, 500 μm crystals were mounted on thermoplastic wax on the surface of a silicon wafer, at an arbitrary position, that is, the angle between the diagonal of Vickers impression and the [1 0 0] direction was always of 45°.

The deformation of the $YBa_2Cu_3O_{7-\delta}$ crystal exhibited an unexpected anomaly – for maximum indentation loads not exceeding 118 mN, the conventional hardness-load dependence appears quite typical (see Fig. 24(a) for sapphire), while it decays suddenly to low H_d values for higher ($P_{max} \geq 196$ mN) indentation loads (Fig. 27). This observation suggests a change of deformation mechanism in the crystal at higher-indentation loads.

The influence of the indentation load on the deformation process of the (0 0 1) plane of the $YBa_2Cu_3O_{7-\delta}$ crystal was confirmed by an analysis of the $P-h$ curves and the indentation depth time $h-t$ relationship (Fig. 28), based on the EPI theory. It was found that the loading path for $P_{max} \geq 196$ mN differs significantly from the curves obtained with loads not exceeding 118 mN (compare Figs. 28(a)–28(c) and 28(d)). The observed inconsistency is additionally illustrated in detail in the accompanying h–t plots. The plateau which occurred for the indentation load of approximately 140 mN (Fig. 28(d)) indicates a sudden increase in irreversible deformation (Fig. 29), which makes it impossible to determine the true hardness H_T within the whole load interval.

According to EPI analysis, the $YBa_2Cu_3O_{7-\delta}$ crystal exhibits regular indentation behavior within the low-load regime, following perfectly the predicted linear relationship (Fig. 29). For the particular load of 196 mN, the scatter in U_r energy is much larger than for measurements under the other loads. This suggests that the detected anomalous behavior is caused by the fracture process, since the singularities associated with the pressure-induced phase transformation are usually precisely located in the P–h curves [63]. A microscopic inspection of the residual impressions by Nowak et al. [194] revealed marked differences between the surface features formed under the higher ($P_{max} \geq 196$ mN) and lower ($P_{max} \leq 118$ mN) indentation loads (Fig. 30). The central cracks around the low-load impression (Fig. 30(a)) appeared to be well developed. However, they did not resemble the pattern reported by Cook et al. [208] for the same kind of material, since the central–radial cracks did not originate along the indenter edges. It should be emphasized that it is the only case in the experience of the present author in which the radial cracks did not originate in the area where the significant concentration of stress occurred.

While the plastic zone around the indents was clearly visible (Fig. 30(a)), and the crack traces followed the [1 0 0] and [0 1 0] directions, the observed patterns were repeatedly irregular, making it impossible to estimate the fracture toughness of $YBa_2Cu_3O_{7-\delta}$. This differs from the conclusions of Cook et al. [208] and Raynes et al. [209], who claimed to measure the toughness of superconducting crystal using the indentation method. Furthermore, the impressions obtained under higher load (Figs. 30(b) and 30(c)) prove that the fracture that occurred during penetration is relatively anomalous. The widespread crushing of the (0 0 1) surface of $YBa_2Cu_3O_{7-\delta}$ is responsible for the irregularity in the P–h path (Fig. 28(d)), the decrease in hardness (Fig. 27), and the enhanced expense of indentation energy during high-load tests (Fig. 29).

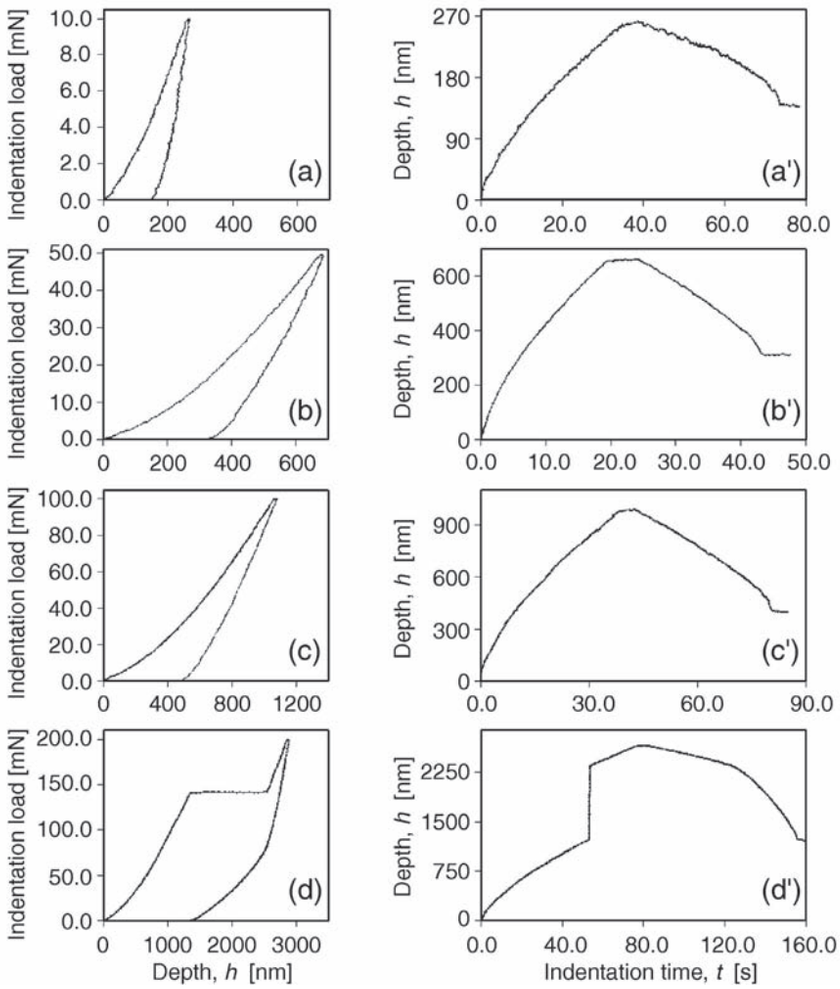

Figure 28. Typical *P–h* curves for the (0 0 1) plane of the $YBa_2Cu_3O_{7-\delta}$ crystal deformed under lower (a–c) and higher (d) maximum indentation loads. The *h–t* plots illustrate variations of indentation depth vs. time for each case.

Hence, the example of indentation examination of $YBa_2Cu_3O_{7-\delta}$ clearly shows that the EPI analysis is useful for testing small crystals that exhibit anomalous mechanical behavior. It should be stated that the very fresh indentation examination of the superconductors target nowadays hardness measurement at cryogenic temperatures [210, 211].

4.4.4. Nanoindentation Examination of Semiconducting InGaN and GaN Crystals

High-Accuracy, Low-Load Indentation Experiments. Ultramicroindentation devices that allow us to use loads as low as fractions of milinewtons have recently been developed in response to an increasing demand for the mechanical testing of thin films designed for electronics. Commercially available examples of such equipment include the nanoindentation systems NANOINDENTER and HYSITRON TRIBOSCOPE (Nano Instruments Inc., Knoxville, TN, USA) and the ultramicro indentation system UMIS-2000 (CSIRO, Lindfield, Australia) (Fig. 31). The latter equipment was used by Nowak et al. [195, 196] to evaluate the mechanical properties of InGaN, while the recent high-accuracy research on GaN was accomplished by Fujikane et al. [197] with Hysitron TriboIndenter.

The successful determination of the mechanical characteristics of new semiconductors, reported in the present section, is partly owing to the application of the UMIS and Hysitron TriboIndenter testers. Indeed, the precision of measurements is of primary importance when one deals with advanced materials that have not yet been characterized. A considerable scattering of the experimental data may lead to erroneous conclusions and confusing claims that a novel effect has been discovered. Such unfortunate incidents occasionally occur in the case of materials with unrecognized properties, when tested with nonstandardized methods.

The mechanical characteristics of GaN and InGaN are nowadays in great demand, since their evaluation is essential for further theoretical and experimental study that should pave the way to solving the problem of large-defect density in heteroepitaxial nitride layers [212]. Suffice it to say that the difficulties with the production and maintenance of

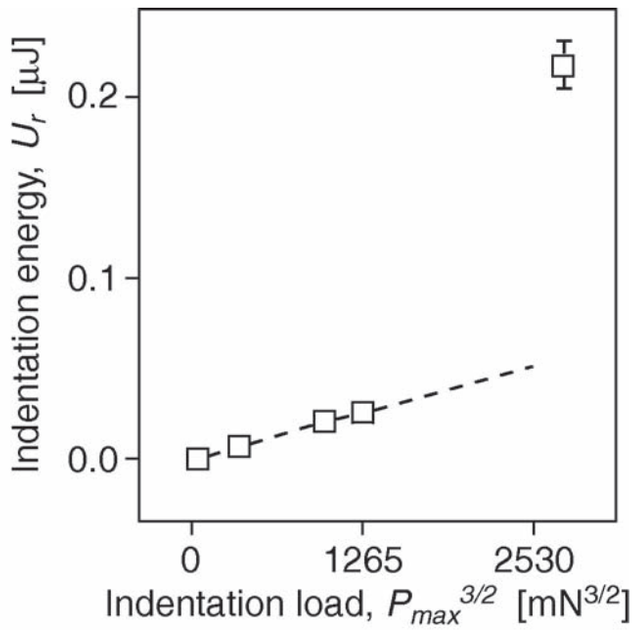

Figure 29. The U_r–$P_{max}^{3/2}$ relationship determined for the superconducting $YBa_2Cu_3O_{7-\delta}$ crystal.

crack-free nitride layers were critical for Nakamura's construction of his first "blue-laser" diode [213]. It was accomplished by introducing into a sandwich-like device a soft buffer layer of InGaN designed to act as a cushion, relaxing the stresses that appear at the interface of the films, and which in turn leads inevitably to fracture in GaN.

The knowledge of mechanical parameters is similarly essential for studying residual stresses that arise owing to the difference in lattice parameters and coefficients of thermal expansion of the film and the substrate [214]. The mismatch stress is a dilemma for GaN optoelectronic devices since the residual strain affects the threshold power density in stimulated emission [215]. It is becoming increasingly evident that successful applications of new semiconductors will depend not only on their optoelectronic characteristics, but also on their mechanical properties.

The EPI Analysis of InGaN Epitaxial Layers. The studies of GaN-based materials concentrated chiefly on the methods and conditions for developing higher-quality semiconductors, doping the crystals, and electrical and optical properties of the films while disregarding their mechanical properties. Considerable effort has been made to evaluate elastic properties of GaN and InGaN by means of first-principle calculations [216]. Since the theoretically obtained values of Young's modulus were not verified experimentally, Nowak et al. [195, 196] attempted to evaluate the mechanical characteristics of these optoelectronic materials using indentation experiments (the resent revision in Ref. [197]).

In order to evaluate the hardness of InGaN, Nowak et al. [195] investigated the 1000 nm thin InGaN films MOCVD grown on the (0 0 0 1) plane of sapphire. The (0 0 0 1) surfaces of the undoped layers and those doped with Mg were tested using the UMIS system equipped with a triangular diamond indenter oriented in such a way as to form an angle of 0° or 90° between the side of the impression and the $[1\bar{2}10]$ direction. The combination of relatively low indentation loads (P_{max} = 2−500 mN) and high thickness of InGaN films allowed the authors to disregard the problem of the substrate effect [195].

The registered *P–h* curves were smooth and regular (examples shown in Fig. 32(a)), and the data obtained for the Mg-doped films revealed no influence of the dopant on the deformation of InGaN (Fig. 32(b)). The differences observed

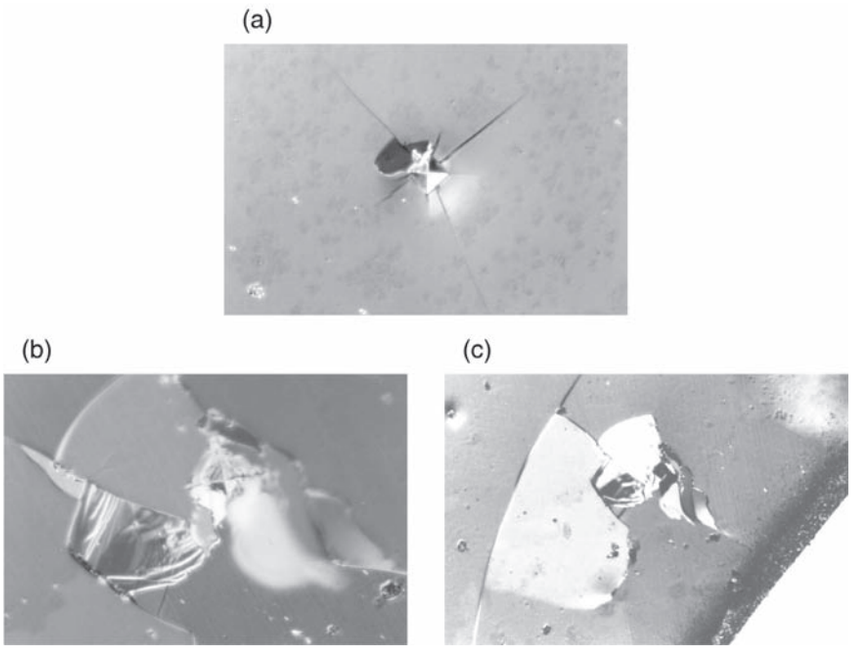

Figure 30. The indentation impressions on the (0 0 1) plane of $YBa_2Cu_3O_{7-\delta}$ crystal, obtained under P_{max} = 49 mN (a) and P_{max} = 196 mN (b, c).

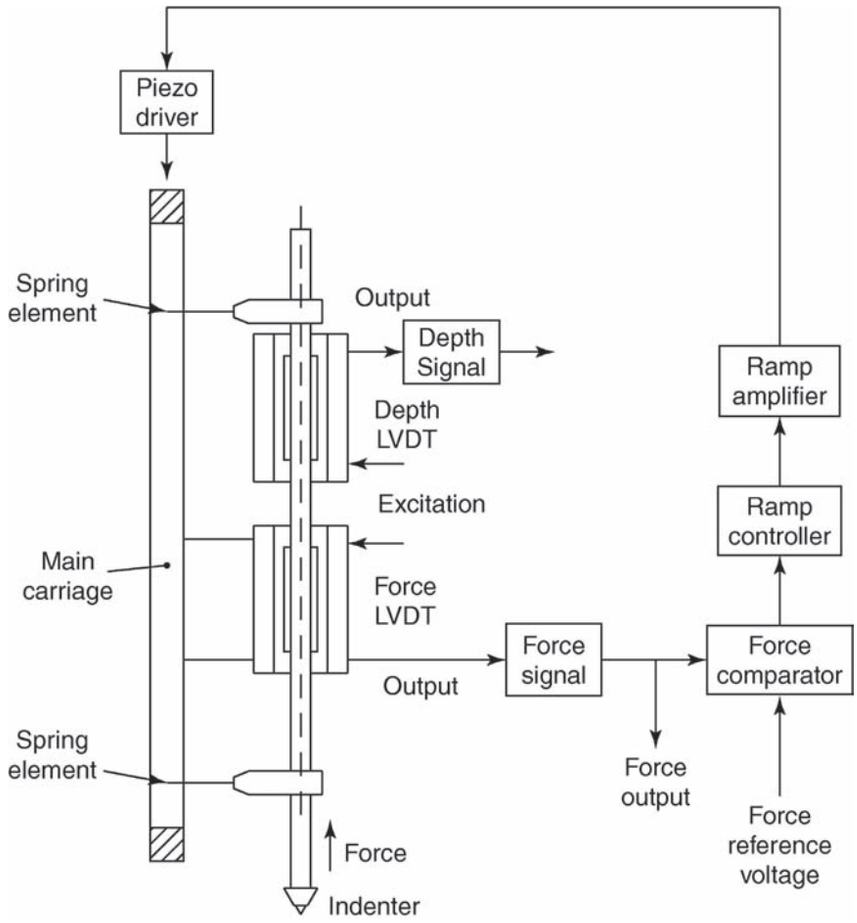

Figure 31. The essential features of the ultramicroindentation system. Reprinted with permission from [59], T. J. Bell et al., *Metrologia* 28, 463 (1992). © 1992, Institute of Physics.

for various orientations of the Berkovich tip (Fig. 32(b)) were small, since the (0 0 0 1) plane of wurtzite structure is quasi-isotropic owing to its sixfold symmetry.

The U_r–P_{max} relationships recorded for In GaN as well as for the $(10\bar{1}0)$ plane of sapphire are depicted in the same figure (Fig. 33), which makes it possible to visualize the significant differences in indentation response of these two crystals. They reflect the anisotropic indentation behavior of InGaN, which becomes marked for the higher-indentation loads, since the effect of the low symmetry of the penetrator is obviously stronger for deeper penetration. In contrast to InGaN, sapphire crystal appeared to be less deformable, that is, harder (Fig. 33). The true hardness H_T of InGaN and sapphire (see Table 3) showed that sapphire appears to be considerably harder than the InGaN [195]. The hardness value recorded in ultralow load experiments is higher than that obtained for moderate loads, which holds for InGaN following a common rule.

The anisotropy of surface deformation of the InGaN crystal registered with a triangular indenter resembled, to certain extent, the nanoindentation behavior of sapphire (theoretically predicted and measured by Nowak and Sakai [46, 193]). In contrast to the (0 0 0 1) plane of sapphire, the observed anisotropic effects were less expressed in the case of the basal plane of InGaN, which involves important and practical consequences – considerable mismatch between the deposited film (InGaN) and a substrate (Al_2O_3). In view of the above, the discovery by Nakamura et al. [213], who observed improvement in the quality of InGaN when grown on the GaN substrate rather than on sapphire, is readily understood.

The AFM observations of the indentation impressions in InGaN revealed that they possess the well-defined shape with no traces of radial cracks (Fig. 34(a)) while their depth profile (Fig. 34(b)) confirmed plastic behavior of InGaN (note pileup near the facet of the indenter) in contrast to the brittle response

Table 3. True hardness H_T of InGaN and sapphire measured using microindentation experiments (Reprinted with permission from [195], R. Nowak et al., *Thin Solid Films* 295, 193 (1997). © 1997, Elsevier).

Material	H_T (GPa) (20 mN ≤ P_{max} ≤ 500 mN)	H_T (GPa) (2 mN ≤ P_{max} ≤ 10 mN)
Undoped crystal	52.0	–
Crystal doped with Mg orientation 0°	49.9	–
InGaN doped with Mg orientation 90°	43.5	45.6
The $(10\bar{1}0)$ plane of sapphire	81.6	83.6

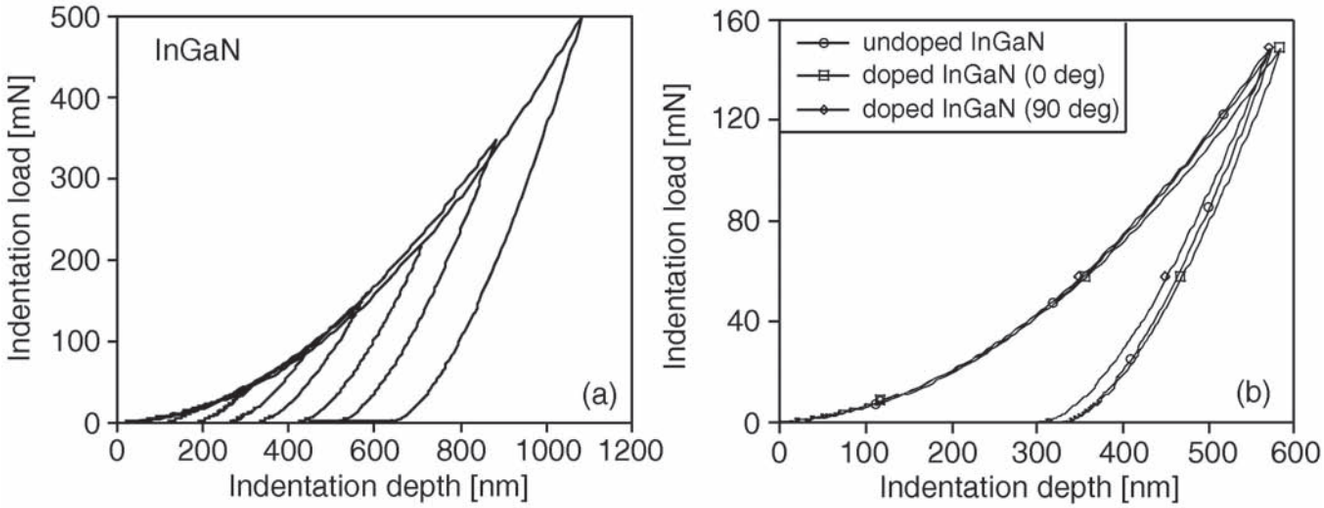

Figure 32. The *P–h* diagrams for undoped InGaN deposited by MOCVD on sapphire (a), and the indentation results obtained with a variously oriented triangular indenter (0°, 90°) for the film doped with Mg (b). Reprinted with permission from [195], R. Nowak et al., Thin Solid Films 295, 193 (1997). © 1997, Elsevier.

observed for ceramic materials, such as sapphire (Fig. 26)). Lack of radial cracks is an indication of considerable fracture toughness of InGaN. Nowak et al. [195] argued that this is precisely what makes it difficult to cleave InGaN, a problem of particular importance in the production of cavity mirrors for LD structure. Their view contradicts Tanaka et al. [217], who attributed the above problem to the exceptional hardness of InGaN.

In sum, nanoindentation experiments [195] have revealed that, contrary to common opinion, InGaN is more deformable than sapphire, while the lack of indentation-induced cracks, detected by AFM technique, indicated that InGaN cannot be considered a brittle material. The excellent result concerning GaN-related research that includes nanoindentation experimentation was recently offered by Kucheyev et al. [218].

Nanoindentation of GaN Bulk Crystals. GaN is produced in the form of a thin film deposited heteroepitaxially onto Al_2O_3 or SiC wafers [219] or quasi-homoepitaxially onto GaN templates [220]. Therefore, even the nanoindentation examination of its mechanical properties faces problems common among HFs – the substrate effect. To avoid this drawback, and to obtain reliable measurement of GaN mechanical characteristics, Nowak et al. [196] conducted nanoindentation studies of bulk GaN. Their approach contrasts with the earlier research by Drory et al. [221], who aimed to evaluate the Vickers hardness and toughness of the same bulk GaN by means of a conventional hardness test. It additionally differs from the nanoindentation experiments on the GaN epilayers deposited onto sapphire conducted by Yu et al. [222] in that their results might be affected by the substrate.

The GaN crystals studied by Nowak et al. [196] were obtained using the self-seeding process, while the

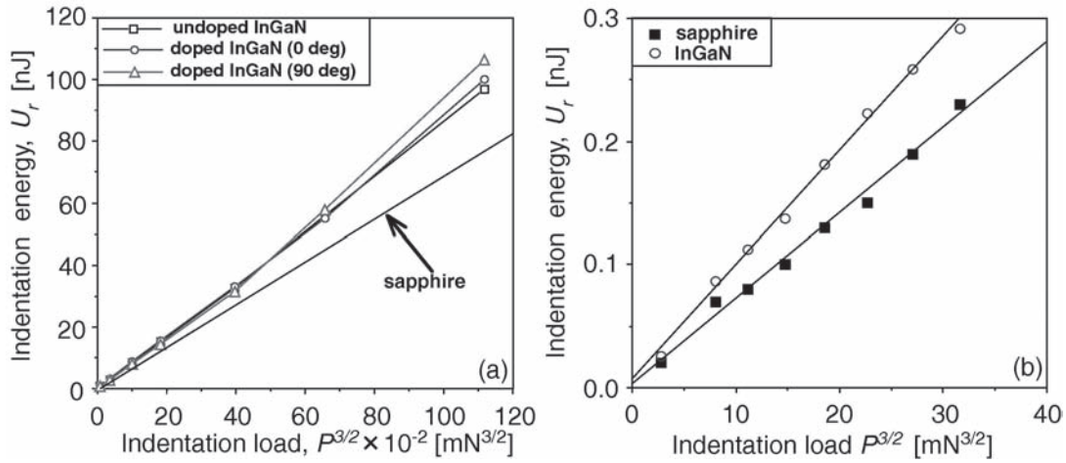

Figure 33. The U_r–$P_{max}^{3/2}$ diagrams for sapphire, and InGaN undoped and doped with Mg obtained under high (a) and low (b) indentation loads. Reprinted with permission from [195], R. Nowak et al., *Thin Solid Films* 295, 193 (1997). © 1997, Elsevier.

indentation experiments were performed on the (0 0 0 1) plane of the crystal using the UMIS-2000 system, equipped with a sharp triangular indenter loaded from 1 to 30 mN.

The $P-h$ data obtained for various maximum loads P_{max} (Fig. 35) enabled the authors to evaluate hardness H and Young's modulus E of GaN, according to the procedure by Oliver and Pharr (see Sections 2.1.2 and 2.2.2). Taking advantage of the recommendation by Leszczynski [214], who suggested the value of $\nu = 0.25$ as being proper for Poisson ratio of GaN, and using eqns (2.10) and (2.24), Nowak et al. [196] were able to resolve E and H, which match the values $E_{GaN} = 295 \pm 3$ GPa and $H_{GaN} = 18-20$ GPa for P_{max} ranging from 2 to 30 mN.

The value of the modulus E_{GaN}, determined by nanoindentation [196], exceeds 287 GPa – the level deduced from Brillouin scattering measurements [221], while it agreed by coincidence with the result ($E = 290$ GPa) obtained for GaN films epitaxially grown on sapphire by Yu et al. [222], despite the latter using the diamond elastic constants and GaN Poisson's ratio which contrast with the commonly accepted values. The magnitude of measured Young's modulus was apparently in agreement with the results of first-principle calculations [216]. Their reckoned H_{GaN} value differed, however, significantly from the Vickers hardness (8–14 GPa) claimed by Drory et al. [221], whose low level is owing to the use of conventional, high-load measurements of considerably lower accuracy than the nanoindentation experiments used in Ref. [196].

In order to verify the value of "true hardness" H_T measured for GaN thin films deposited on sapphire by Yu et al. [222], the P–h curves (Fig. 35) recorded for a bulk crystal were used. Nowak et al. [196] found $H_{T\ GaN}$ to be 30 GPa – markedly different from the 53.6 to 56.3 GPa reported by Yu et al. for GaN epilayers, despite identical conditions in both the works. The authors believe that this difference is associated with an inconsistency in the mechanical response of bulk and thin film material. Contrary to these results (Fig. 35), Yu et al. [222] witnessed the sudden depth excursion during indentation in the 1.3–2.4 μm thick GaN layers ($P_{max} = 1.7$ mN), which they attributed to the onset of the dislocation activity, following the concept articulated by Page et al. [24] and recently confirmed by Fujikane et al. [197].

Interestingly, repeated efforts by Nowak et al. [196] to detect the discontinuities in P–h curves for bulk GaN were unsuccessful (Fig. 35) ; they suspected that the depth excursions reported by Yu et al. [222] did not reflect the inherent properties of GaN, in asmuchas the singularity appears at a very low load, it is unlikely that the event is owing to twinning [99, 132, 197, 205]. They also dismissed the possibility of the pressure-induced phase transformation [175, 223] since GaN transition from wurzite to rocksalt structure is expected at pressure as high as 52.2 GPa [152]. Thus, Nowak et al. argue that the reported discontinuity is associated with the emission of dislocations from the GaN–sapphire interface, given the dependence of critical load for the singularity and Young's modulus on the layer thickness reported by Yu et al. [222].

Furthermore, Nowak et al. [196] confirmed the results obtained by nanoindentation of sharp indenter using stepwise spherical indentation with partial unloading (see Section 2.1.3) (The general illustration – Fig. 5 – represents the data obtained by Nowak et al. [197] for GaN crystal during stepwise spherical indentation with partial unloading.) and determined the yield strength of GaN to equal $\sigma_Y = 15$ GPa. These measurements enabled them to accomplish a near-continuous assessment of the elastic modulus vs. depth, and to resolve relationship between the indentation contact pressure and strain, that is, indentation stress–strain curve for GaN (details in Ref. [196]).

This section, then, provides an example of the successful characterization of a new material that is of central interest in the field of electronics. The mechanical properties of GaN were accurately evaluated owing to the availability of unique bulk crystal and the application of the nanoindentation experiments. According to the results, GaN appears to be a material with unusual properties, one that combines high Young's modulus and hardness with nonbrittle behavior, which was recently confirmed by ultraaccurate measurements by Fujikane et al. [197].

4.4.5. Comments on the EPI Approach and Crystal Deformation

The energy principle approach to the depth-sensing indentation data (EPI) has proved to be successful in predicting new phenomena in deformed crystals and in analyzing "anomalous"

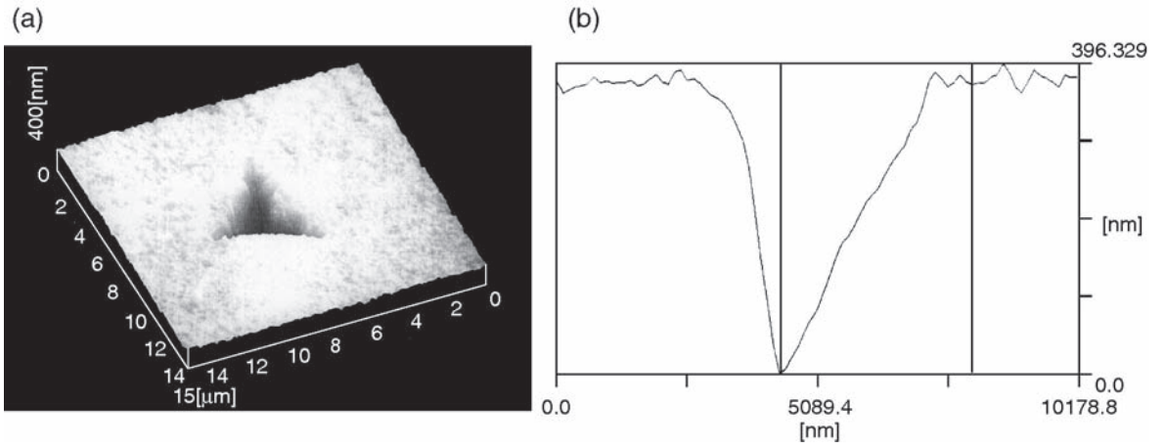

Figure 34. Typical AFM micrograph of the indentation impressions ($P_{max} = 150$ mN) on the (0 0 0 1) plane of InGaN displaying no fracture traces (a) together with its depth-profile (b). Reprinted with permission from [195], R. Nowak et al., *Thin Solid Films* 295, 193 (1997). © 1997, Elsevier.

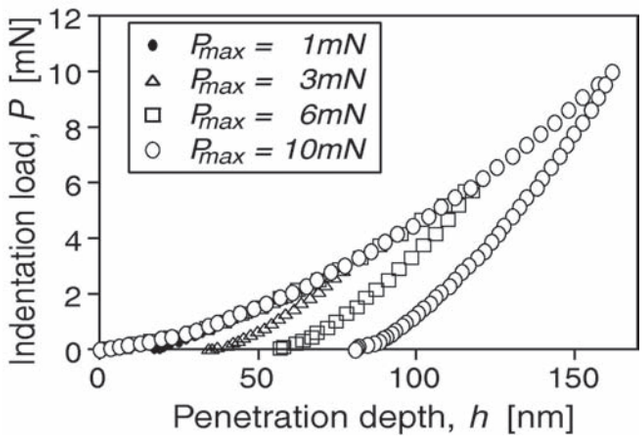

Figure 35. Load–displacement curves obtained for GaN crystal deformed with a sharp indenter. Reprinted with permission from [196], R. Nowak et al., *Appl. Phys. Lett*. 75, 2070 (1999). © 1999, American Institute of Physics.

indentation data. This energy-based analysis is so accurate that it enabled users to resolve the indentation anisotropy of the $(10\bar{1}0)$ plane of sapphire for different orientations of a triangular indenter (Fig. 25), while conventional hardness measurements (Fig. 24) provided somewhat confusing results. It allowed the authors to determine the hardness level of $YBa_2Cu_3O_{7-\delta}$, GaN and InGaN crystals, despite the rather complex indentation behavior exhibited by these materials.

Both the depth-sensing indentation method and EPI theory are well suited to characterizing new materials. The low-load indentation experiments have revealed that, contrary to common opinion, InGaN is softer and more ductile than sapphire crystal (Fig. 33). Its hardness, estimated according to the EPI, is lower than that of sapphire, while its anisotropic surface deformation is less marked than that observed from indentations in Al_2O_3 crystals. The EPI method was also useful when evaluating the mechanical properties of the tiny and very brittle $YBa_2Cu_3O_{7-\delta}$.crystals that exhibited a crushing-like behavior (Figs. 29 and 30). Finally, the mechanical properties of GaN crystals were accurately determined using the EPI analysis of nanoindentation data.

Despite the advantages, the EPI can explain neither the unusual fracture patterns which differ markedly for N and R orientations of the triangular indenter pressed onto the $(10\bar{1}0)$ plane of sapphire (Fig. 26) nor the origin of the pop-ins observed in the loading cycle of $P-h$ curves for particular tip orientations (see Fig. 23). Furthermore, the EPI theory fails to take account of the structure of the tested material and the shape of the used indenter tip (in fact, one refers here to the axisymmetric contact model). These drawbacks do not undermine, however, the validity of the concept of true hardness. The support of the EPI approach with crystallographic considerations (addressed in the following section) is an appropriate way to overcome the shortcomings of the analysis applied to crystalline materials (see, e.g. [197, 218].

4.5. Surface Deformation of Sapphire: ERSS Considerations

The anisotropic indentation fracture and surprising singularities in a loading path of the *P–h* curve recorded during indentation of sapphire (Figs. 23(d) and 26) prompted Nowak and Sakai [193] to search for a suitable model to predict the location and clarify the origin of characteristic surface features visible in the vicinity of impressions. Such a study is, to a certain extent, similar to the investigations of the Knoop hardness anisotropy of crystals, which have a long history. The employment of the depth-sensing indentation research allowed Nowak and Sakai [193] to provide a new insight into this well-established area of material science. Further explanation of the anomalous surface deformation of Al_2O_3 crystals was offered by Nowak, Sekino and Niihara [99, 132, 205] based on low-load indentation experiments. However, the most advanced account of the indentation anisotropy was accomplished in the Nordic Hysitron Laboratory [206–207] and recently revised for nanoscale deformation [38].

4.5.1. Early Approaches to the Knoop Hardness Anisotropy of Crystals

A report on slip lines around the indentation marks and the relationship between crystal orientation and its hardness appeared 90 years ago [198]. Moreover, in 1923, O'Neil studied the Brinell hardness for different crystallographic planes of aluminum crystals [224]. Since the publication of early results concerning the Knoop hardness of minerals by Winchell [225], and the paper on the anisotropy of Knoop hardness by Daniels and Dunn [199], the term "hardness anisotropy" has been used exclusively to define the conventional indentation experiments conducted with a variously oriented Knoop pyramid (the low-class symmetry indenter – refer to Table 1).

In addition, there appeared a considerable number of studies, both theoretical and experimental, which addressed hardness anisotropy of various crystals and the application of the hardness anisotropy to identify crystal slip systems. However, the hardness anisotropy of crystals with hexagonal or rhombohedral structure was never clarified by the existing models. These difficulties triggered investigations of indentation into sapphire by Nowak and Sakai [193]. Moreover, the recent applications of sapphire in electronics required detailed information on material properties formerly considered as to be well understood, which nowadays received a new clarification.

Among a large number of studies on the Knoop hardness anisotropy, the ideas of Daniels and Dunn [199] as well as of Brookes et al. [200] became widely accepted. Daniels and Dunn [199] estimated the probability of activation of the primary slip system during the Knoop hardness test of Fe–3 wt.% Si single crystals. They assumed the direction of the force $\boldsymbol{F}$ exerted on the material unit volume of cross-sectional area A to be parallel to the indenter facet, and consequently derived a formula for the effective resolve shear stress τ_{eff} which acts in a primary slip system:

$$_{eff} = \frac{\boldsymbol{F}}{A}(\cos \ \cos \ )\cos \quad , \tag{4.18}$$

where the product ($\cos\lambda \cos\phi$) is the "Schmidt factor," λ defines the angle between $\boldsymbol{F}$ and the unit normal vector $\boldsymbol{n}$ of the primary slip plane, while ϕ stands for the angle between the slip direction $\boldsymbol{g}$ and the vector $\boldsymbol{F}$. Daniels and Dunn [199] modified the "Schmidt formula" using the constraint factor $\cos\chi$(χ denotes the angle between $\boldsymbol{F}$ and the axis of slip system rotation) to improve the "tensile

strength approximation" they started with. Using eqn (4.18), they predicted the position of the Knoop indenter for which extreme values of τ_{eff} are attained. Their results accorded with the hardness anisotropy observed for cubic crystalline structure (silicon ferrite), having an exception in hexagonal zinc crystals [199].

In 1971 Brookes et al. [200] provided a modified analysis of the indentation deformation of single crystals and proposed a new expression for τ_{ef}:

$$\tau_{eff} = \frac{\mathbf{F}}{A}(\cos\lambda\cos\phi)\frac{\cos\chi + \sin\kappa}{2}, \qquad (4.19)$$

where κ defines the angle between the rotation axis of the selected slip system and its direction $\boldsymbol{g}$.

The approach by Brookes et al. [200] received widespread recognition and for two decades it was in common use for Knoop hardness anisotropy of crystals (see an introduction in Ref. [193]) despite its failure in the case of alumina single crystal, as with the alternative version of ERSS model proposed by Armstrong and Raghuram [202]. Thorough criticism of the drawbacks of the considerations by Daniels and Dunn [199] and Brookes et al. [200] was articulated by Arnell [226], who emphasized that both theoretical approaches were unable to predict hardness anisotropy for materials with hexagonal and rhombohedral structure.

An original view of hardness anisotropy was presented by Hirsch et al. [227] and Roberts et al. [228], which still followed the resolved shear stress concept introduced by Daniels and Dunn [199]. The authors applied Nadai's [229] solution of an elastic contact between a rigid flat punch and an isotropic solid to their Knoop indentation, which enabled them to estimate stress components under the indenter [227]:

$$\sigma_{xx} = -\frac{P}{2\pi}\left[2(\phi_1 - \phi_2) + \sin 2\phi_1 - \sin 2\phi_2\right]$$

$$\sigma_{zz} = -\frac{P}{2\pi}\left[2(\phi_1 - \phi_2) - \sin 2\phi_1 + \sin 2\phi_2\right]$$

$$\sigma_{xz} = -\frac{P}{2\pi}\left[\cos 2\phi_1 - \cos 2\phi_2\right] \qquad \sigma_{yy} = \nu(\sigma_{xx} + \sigma_{zz}) \qquad (4.20)$$

where P and (ϕ_1, ϕ_2) stand for the punch load and the angular coordinates of a given location in the material, respectively.

The more realistic description of the stress under the indenter allowed the researchers to dismiss the constraint factor used in other models. However, the approach by Hirsch et al. [227] was not tested for hexagonal crystals. For completeness, we mention the model by Wonsiewicz et al. [230], based on Taylor's analysis of crystal plasticity [231], while the approach by Pospiech and Gryziecki [201] is addressed in the following section.

4.5.2. Surface Deformation of Sapphire Induced by the Triangular Indenter

A new resolve shear stress model that predicts the indentation deformation of sapphire, a crystal with a rhombohedral structure, was proposed in 1994 by Nowak and Sakai [193]. The approach was an extension of the previous studies by Nowak [203, 204] that concentrated on slip patterns around the Knoop impressions in zinc and sapphire crystals. The new model incorporated the original idea for Knoop hardness anisotropy developed by Daniels and Dunn [199], together with the modifications proposed by Pospiech and Gryziecki [201], Brookes et al. [200], and Sawyer et al. [232]. It introduced a new comprehensive formula for the parameter $T_i(\mu)$ to estimate the probability of activating the ith slip or twinning system under the facet of the sharp indenter, oriented to angle μ:

$$T_i(\mu) \propto \frac{\tau_i}{\tau_{CRi} / \max_i \tau_{CRi}} \Lambda_i, \qquad (4.21)$$

where τ_i stands for shear stress in the ith plane, Λ_i is a correction factor for particular indentation geometry, and τ_{CRi} defines critical shear stress for the ith slip system. The force under the tip is assumed to be perpendicular to the indenter facet, following Pospiech and Gryziecki [201], which yields:

$$\tau_i \propto \cos\lambda\cos\phi, \qquad (4.22)$$

where angles which makes the force vector $\boldsymbol{F}$ with the normal to the slip plane $\boldsymbol{n}_i$ and slip direction $\boldsymbol{g}_i$ are denoted by λ_i and η_i, respectively (Fig. 36). The correction factor Λ_i accommodates the effect of material moving toward the free surface and takes the form:

$$\Lambda_i \propto \cos\omega\cos\delta, \qquad (4.23)$$

where cos ω was incorporated from Pospiech and Gryziecki [201], who found the minimum work required for moving

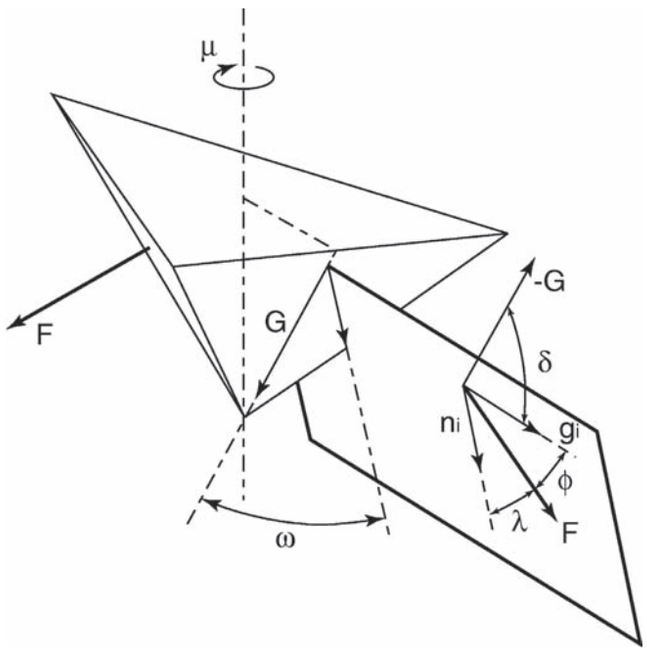

Figure 36. The relationship between the geometry of the triangular indenter and the slip system potentially activated during the penetration process. Reprinted with permission from [193], R. Nowak and M. Sakai, *Acta Metall. Mater*. 42, 2879 (1994). © 1994, Elsevier.

an elemental layer of the material toward the surface to be dependent on ω – the angle between the intersection of the plane determined by the $\boldsymbol{n}_i$ and $\boldsymbol{g}_i$ with the indenter facet, and the vector $-G$, the projection of the pyramid axis onto the indenter facet (details in Fig. 36).

Nowak and Sakai [193] argue, however, that an additional criterion is necessary for selecting the slip system acting along the shortest path to the surface when the value of cos ω reaches its maximum. Such a path could be realized when the slip direction g_i is close to the vector $-G$ parallel to the facet (Fig. 37), which prompted the authors to incorporate into eqn (4.21) an additional factor cos δ(δ is defined in Fig. 36 by vectors $-G$ and g_i). This condition was disregarded in the previous models.

In contrast to the unrealistic assumptions by Daniels and Dunn [199] and by Brookes et al. [200], who considered a single active slip, the $T_i(\mu)$ values [eqn (4.21)] are calculated in [125] for all available slip and twinning systems. The relationship between the T_i value and the hardness $\widetilde{H}(\mu)$, measured with variously oriented (μ) triangular sharp indenter, reads [193]:

$$\widetilde{H}(\mu) \propto \left\{ \sum \left[\max_i T_i^j(\mu) \right] \right\}^{-1}, \qquad (4.24)$$

where j denotes the indenter facet for which the T_i value is apparently determined.

Nowak and Sakai [193] determined the $T_i(\mu)$ parameter for azimuthal positions ($0 \le \mu \le 2\pi$) of the triangular indenter on the (0 0 0 1), (10$\bar{1}$0), and (1$\bar{2}$10) planes of sapphire [193], using the critical resolved shear stress values for slip and twinning in sapphire listed in Table 4 (see the results in Figs. 38(a)–38(c)). The additional calculations were made assuming a single $\tau_{CR}i$

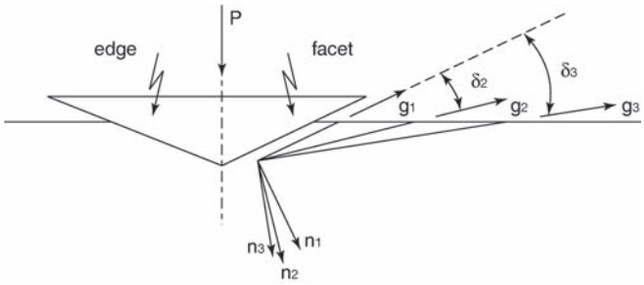

Figure 37. The schematic that enables us to recognize the slip systems for which the models of Daniels and Dunn [199], Brookes et al. [200], and the one by Pospiech and Gryziecki [201] suggest the same value of the effective shear stress τ_{eff}.

value for various slip–twinning systems in the crystal (the results are given in Figs. 38(a1)–38(c1)). This approach enabled us to identify the deformation systems that are most prone to be activated while using the T–μ curves shown in Figure 38.

Since the orientation "N" of the triangular tip can be described in terms of three μ values: 180°, 300°, and 60°, while the "R" orientation define 0°, 120°, and 240° (Fig. 22), the highest values of T parameter determine the systems activated in the vicinity of the particular impression. Hence, Figure 38(a) predicts rhombohedral or basal twinning for "R" orientation of the impression on the (10$\bar{1}$0) plane, and particularly intensive twinning is expected near the facet positioned along the [1$\bar{2}$10] direction (Fig. 38(a1)). Nowak and Sakai [193] expected the "R" impression to be associated with particularly large deformation near the indicated facet, which might cause lateral cracking during unloading. In the case of the "N" impression on the (10$\bar{1}$0) plane, the authors

AQ4 **Table 4.** Twinning and slip systems considered in the model calculations [84] (the indices are referred to the structural unit cell (c/a = 2.73)).

Symbol	Twinning–slip system	Description	Critical shear stress (GPa)	Reference
1	$\langle 2\bar{1}\bar{1}0\rangle$ (0001)		17	[235, 236, 240]
2	$\langle 10\bar{1}0\rangle \{\bar{1}2\bar{1}0\}$	Prismatic slip		[237; J. Cadoz et al., Rev. Phys. Appl. 3, 473 (1977); J. Cadoz et al., Rev. Phys. Appl. 16, 135 (1981); J. Castaing et al., J. Am. Ceram. Soc. 64, 504 (1981); D. Kotchick et al., J. Am. Ceram. Soc. 64, 429 (1980)]
3	$\eta_1\langle 1\bar{1}00\rangle k_1(0001)$	Basal twinning	0.148	[235, 238, 240]
4	$\eta_1\langle 0\bar{1}11\rangle k_1(01\bar{1}2)$	Rhombohedral twinning	0.111	[235, 238, O. Bhandari et al., Acta Metall. Mater. 21, 1515 (1973); W. Scott et al., J. Am. Ceram. Soc. 66, 27 (1983); 239, J. Chung et al., Proc. 6 Japan.–Korean Sem. Ceram., Osaka, 521 (1989)]
5	$\langle 2\bar{1}\bar{1}0\rangle \{01\bar{1}2\}$	Rhombohedral slip	3	[235, 240]
6	$\langle 10\bar{1}1\rangle \{\bar{1}101\}$	Pyramidal slip	18	[235, 237, 240]
	$\langle 10\bar{1}1\rangle \{\bar{1}012\}$			
	$\langle 10\bar{1}1\rangle \{\bar{1}\bar{1}23\}$			

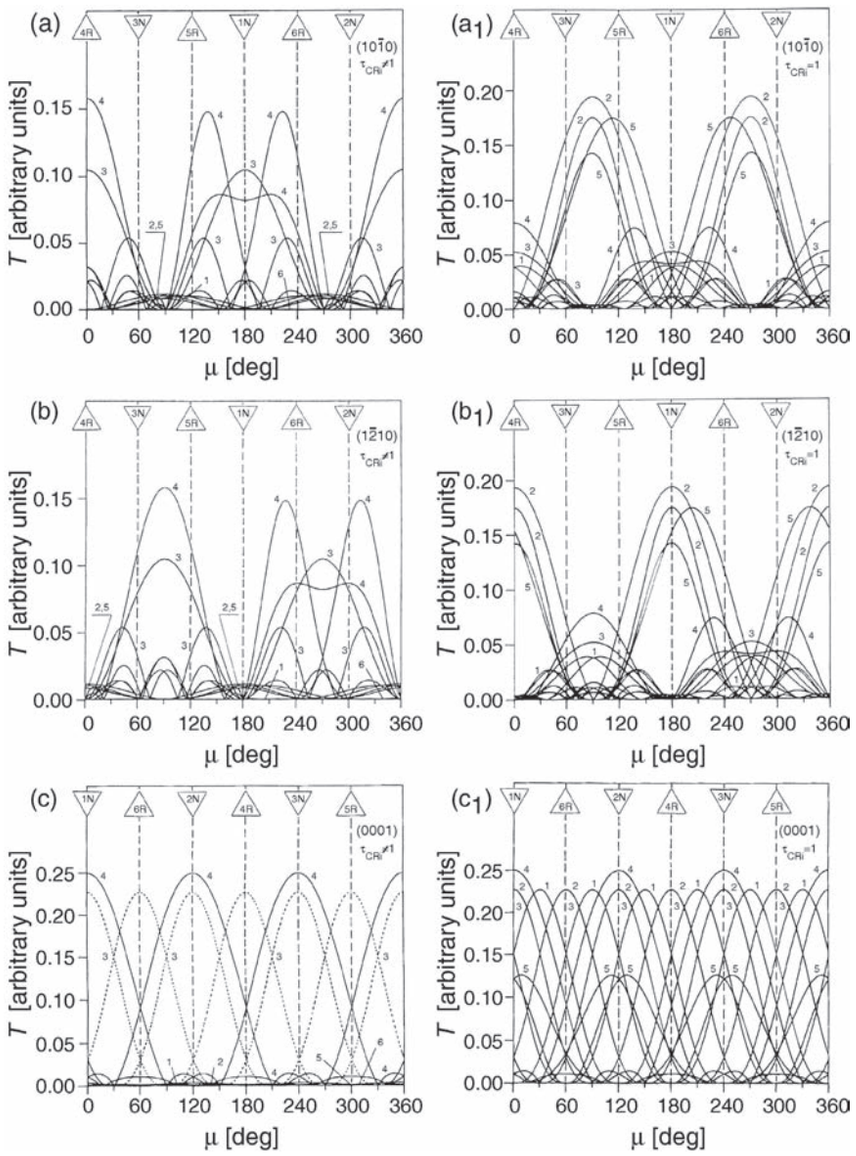

Figure 38. *T* parameter calculated for the variously oriented (l angle) Berkovich indenter on the (10$\bar{1}$0) plane (a-a$_1$), the (1$\bar{2}$10) plane (b-b$_1$), and the (0 0 0 1) plane (c-c$_1$) of sapphire. The τ_{CRi} values were taken from Table 4 (a–c) or assumed to be unit (a$_1$, b$_1$, and c$_1$) (after Nowak and Sakai [125]). The numbers of the respective curves represent the slip–twinning systems given in Table 4. Reprinted with permission from [193], R. Nowak and M. Sakai, Acta Metall. Mater. 42, 2879 (1994). © 1994, Elsevier.

suggested that basal twinning and prismatic slip should dominate the deformation near each facet (Fig. 38).

Their prediction was confirmed by microscopic inspection of the indentation features on the (10$\bar{1}$0) plane of Al_2O_3 crystal (Fig. 39). Indeed, the deformation patterns around the "N" impression are less developed than for R orientation. Since the probability of activating slip and twinning is considerably lower for the N orientation (Fig. 38(a)), the stress induced by indentation relaxes through fracture. This explains the appearance of radial cracks for "N" impression and their absence for R orientation (Fig. 39). Differences in mechanical response of the (10$\bar{1}$0) plane of sapphire indented with various tip orientations (N, R) are reflected in the shape of the $P-h$ curves (compare Figs. 23(c) and 23(d)).

A similar discussion was offered for indentation of the (1$\bar{2}$10) and (0 0 0 1) planes of sapphire [193]. The analysis of Figures 38(b) and 38(b$_1$) allowed the authors to conclude that the predicted indentation deformation for the (1$\bar{2}$10)N and (1$\bar{2}$10)R impressions should be identical, which was confirmed by the microscopic observations of the R and N crack–twin patterns resembling each other (Fig. 40) as well as similar $P-h$ curves (Figs. 41(a) and 41(b)).

The most surprising results of both the indentation experiments (Figs. 41(c) and 41(d)) and model predictions (Figs. 38(c) and 38(c1)) were realized by Nowak and Sakai [193] for the (0 0 0 1) plane. While the basal plane of rhombohedral crystal is believed to possess quasi-isotropic mechanical properties, the authors observed striking difference between the (0 0 0 1)N and

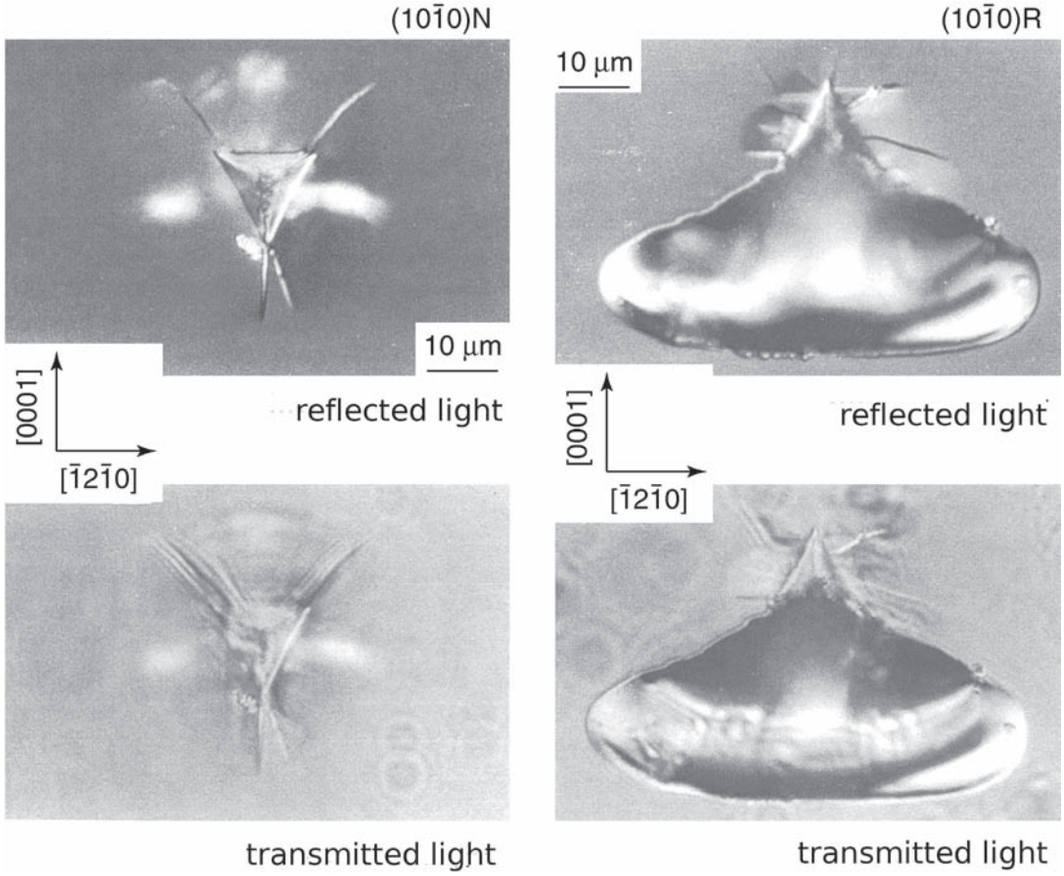

Figure 39. The deformation patterna near "N"- and "R"-oriented indentation impressions on the (10$\bar{1}$0) plane of sapphire observed in reflected and transmitted light. Reprinted with permission from [193], R. Nowak and M. Sakai, *Acta Metall. Mater*. 42, 2879 (1994).© 1994, Elsevier.

(0 0 0 1)R indentations (Figs. 41(c), 41(d) and 42). Based on their theoretical prediction (Fig. 38(c)), and taking advantage of the studies by Kollenberg [233], Nowak and Sakai [193] concluded that large deformation, close to the (0 0 0 1)N impression, is related to the maximum probability of activating rhombohedral twinning, while the defect pattern near the (0 0 0 1)R indentation mark is associated with the minimum probability.

In summary, Nowak and Sakai [193] proved that their theoretical model allows the prediction of mechanisms responsible for the indentation deformation and cracking of sapphire. The prognosis concurred with the patterns of microscopic surface defects and the shape of the *P–h* curves. The presented approach is the only model to provide successful characterization of the indentation anisotropy of crystals with hexagonal and rhombohedral structures provided so far. The important outcome of this study is the conclusion that twinning plays a dominant role in the indentation deformation of sapphire, which agrees with earlier findings by Kollenberg [233] and very fresh TEM [25, 234] and Raman spectroscopy [28] findings.

4.5.3. Deformation of Sapphire under a Spherical Indenter

ERSS Model for Spherical Contact. In order to avoid the anisotropic effects caused by the particular orientation of a nonaxisymmetric indenter on a given crystallographic plane, Nowak, Sekino, and Niihara [99, 132, 205] performed nanoindentation into sapphire with a spherical tip. Use of an axisymmetric penetrator allowed the authors to observe novel phenomena associated with deformation of Al_2O_3 crystal, and consequently to verify earlier findings by Page et al. [24], Kollenberg [233], Lagerlöf, Pirouz, Heuer and coworkers [235–243], as well as Nowak and Sakai [46, 193]. The starting point for the study was the ERSS considerations by Nowak and Sakai [193] concerning deformation of sapphire under a sharp indenter (refer to the preceding section), since displacements in an anisotropic body under the point loading cannot be determined analytically [244], in a similar manner to the isotropic Hertz problem [245, 246]. Nowak et al. [99] found it unrealistic to approximate the stress under a ball indenter with a few force vectors as in the case of Knoop (four forces – Pospiech and Gryziecki [201]) or Berkovich (three vectors – Nowak and Sakai [193]) indenters, and in such a cases, the μ angle that defines the orientation of the indenter on a plane (Fig. 36) is no longer useful.

The authors assumed the directions of the forces $\boldsymbol{F}$ to be perpendicular to every infinitesimal grid ($d\mu \in d\psi$) representing the area of common contact between the indenter and the crystal (Fig. 43). The position of the grid and hence that of the vectors $\boldsymbol{F}$ were denoted by the angular coordinates

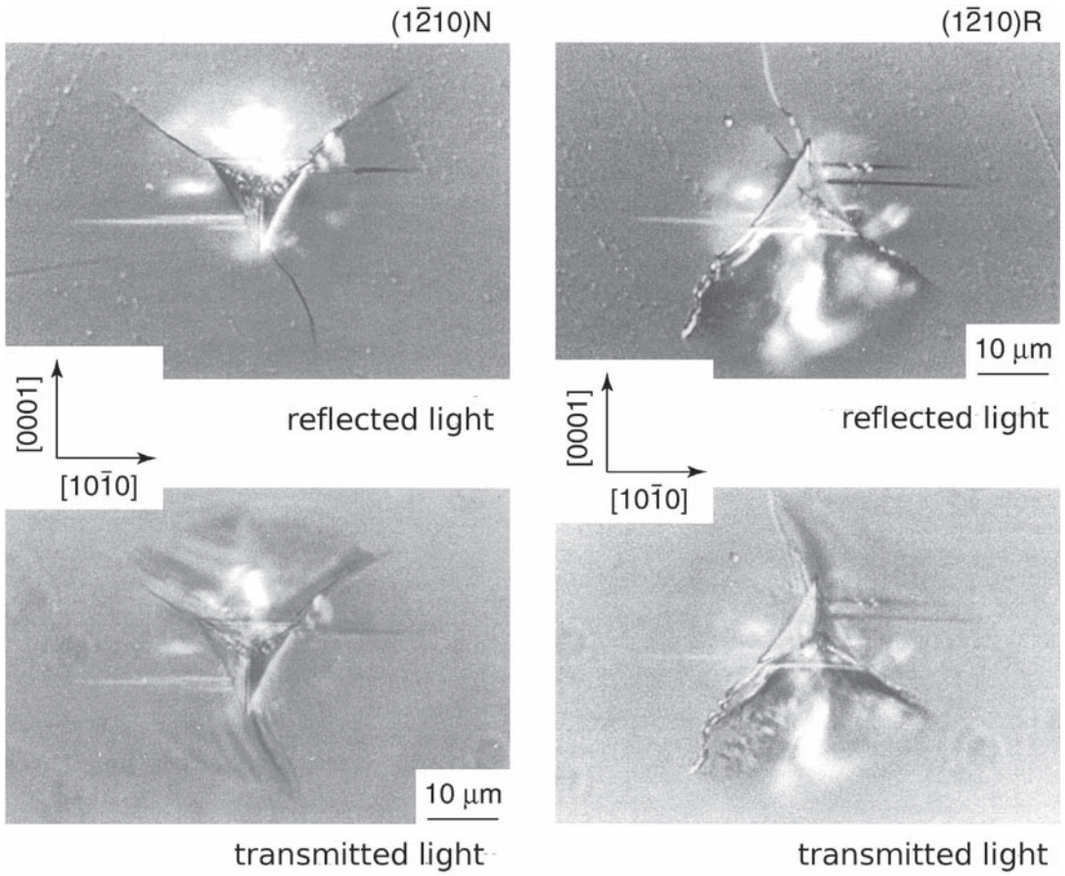

Figure 40. The "N"- and "R"-oriented indentation impressions on the (1$\bar{2}$10) plane of sapphire observed in reflected and transmitted light. Reprinted with permission from [193], R. Nowak and M. Sakai, *Acta Metall. Mater*. 42, 2879 (1994). © 1994, Elsevier.

(μ,ψ) of their center points, where μ is the angle between the plane of indenter symmetry containing vector $\boldsymbol{F}$ and the x-axis, while ψ is defined between the negative part of the z-axis and the vector $\boldsymbol{F}$ (Fig. 43). Approximating the spherical grid by means of a square on the tangent plane (correct on the assumption: $d\mu \to 0$ and $d\psi \to 0$), one comes to the contact problem of the flat facet with the adjacent material. Thus, it was possible to estimate the probability of slip–twinning activation close to the grid (dμ dψ) based on the previously derived equations (eqns (4.21) and (4.23)). The difference between the formulae for a sharp and spherical tip lies in the definition of λ_i, ϕ_i, ω_i, and δ_i parameters, which are in the latter case functions of variables μ and ψ coordinates of the center of a selected grid [$Ti = Ti(\mu, \psi)$], which yields new form of eqn (4.24) for spherical contact [99]:

$$\widetilde{H} \propto \left(\iint_{\mu,\psi} \max T_i(\mu,\psi)\, d\mu d\psi \right)^{-1}, \qquad (4.25)$$

where $0 \le \mu \le 2\pi$ and $0 \le \psi \le \alpha$ for α angle corresponding to the maximum indentation depth h (Fig. 44).

The model by Nowak et al. [99] introduced explicitly indentation-load dependence into the formula for $T_i(\mu, \psi)$, since the higher the mean pressure p under the indenter ($p = P/\pi a^2$), the higher the value of force F, and consequently, the higher shear stress in the ith slip system:

$$T_i(\mu,\psi,p) \propto p \frac{\cos\lambda_i \cos\phi_i}{\tau_{CRi} / \max\limits_i \tau_{CRi}} \cos\omega_i \cos\delta_i. \qquad (4.26)$$

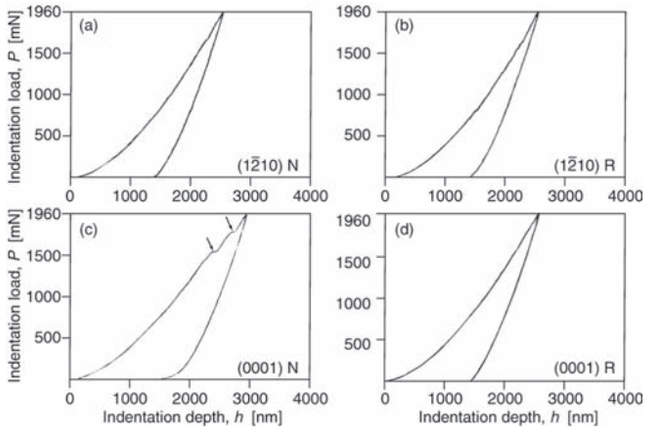

Figure 41. Typical indentation curves obtained with the triangular indenter for the (1$\bar{2}$10)N (a), (1$\bar{2}$10)R (b), (0 0 0 1)N (c), and (0 0 0 1)R (d) orientations. Reprinted with permission from [193], R. Nowak and M. Sakai, *Acta Metall. Mater*. 42, 2879 (1994). © 1994, Elsevier.

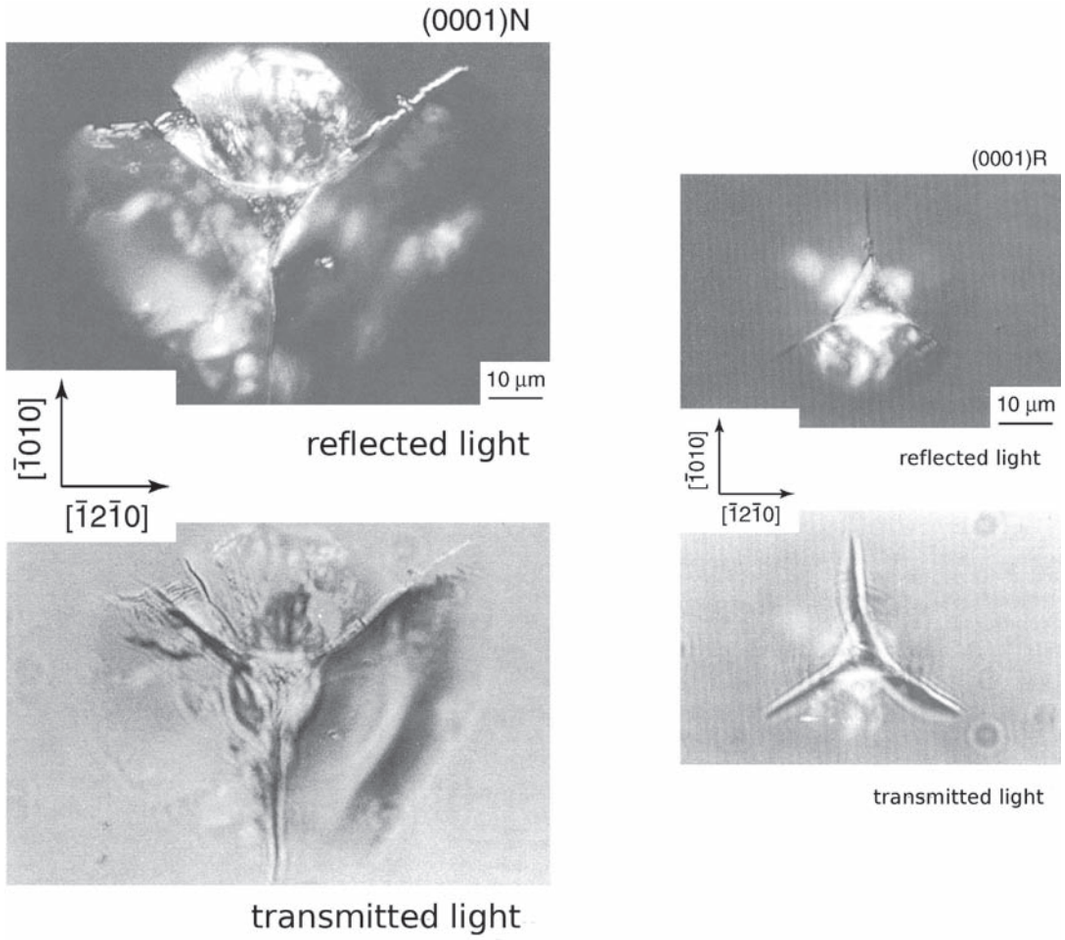

Figure 42. The "N"- and "R" -oriented indentation impressions on the (0 0 0 1) plane of sapphire observed in reflected and transmitted light. Please note that the magnification used for the "N" micrographs is considerably lower than that for "R" indentations. Reprinted with permission from [193], R. Nowak and M. Sakai, *Acta Metall. Mater.* 42, 2879 (1994). © 1994, Elsevier.

In order to determine the slip and twinning systems most prone to be activated during the indentation process, the authors [99] calculated the value of the $T_i(\mu,\in\psi,\in p)$ parameter for μ ranging from 0 to 2π when ψ varies between 0 and α The numerical results were obtained for varying μ and ψ angular coordinates when the distribution of slip directions ***gi*** and slip planes ***ni*** (Table 4) corresponded to the geometry of indentation in the (0 0 0 1) and (10$\bar{1}$0) planes of sapphire. The calculations were performed for all slip and twinning systems (Table 4). The variations of the $T_i(\mu,\in\psi,\in p)$ parameter corresponding to the high- and low-load indentations on the (10$\bar{1}$0) and the (0 0 0 1) planes were plotted [99] vs. the μ angle for constant ψ values (Figs. 45 and 46), enabling the authors to predict the deformation in different crystallographic directions around the ball indenter and to indicate the slip–twinning systems activated during the subsequent stages of penetration (refer to the right scale in Fig. 46 as well as to eqn (4.26)).

Nowak, Sekino, and Niihara [99] conclude that the results of calculations for the (10$\bar{1}$0) plane of sapphire suggest that rhombohedral twinning η_1 ⟨0$\bar{1}$11⟩ K_1 {01$\bar{1}$2} and, secondly, basal twinning ⟨1$\bar{1}$00⟩ (0001) are the mechanisms which should be readily activated at the early stages of indentation (see Figs. 41(a) and 41(b)). They found the highest values of the *T* parameter for rhombohedral and basal twinning in the neighborhood of the orientation $\mu = 0°$ and that denoted by $\mu = 180°$ (Fig. 45(a)). The authors argue that the twinned zone would be extended along the [0 0 0 1] direction, while simultaneous activity of both the basal and the rhombohedral twinning should be expected close to the orientation $\mu = 0°$.

Furthermore, Nowak et al. [99] conclude that, for higher loads, basal twinning becomes the preferred deformation mechanism close to the orientation $\mu = 0°$, while the rhombohedral twinning should be activated close to the orientations $\mu = 135°$ and $\mu = 225°$ (see Fig. 45(b)). The authors expected the activity of the prismatic ⟨0$\bar{1}$0⟩ {$\bar{1}$2$\bar{1}$0} as well as the rhombohedral ⟨2$\bar{1}\bar{1}$0⟩ {01$\bar{1}$2} slip systems close to specific orientations: $\mu = 90°$ and $\mu = 270°$, where the *T* parameter for basal and rhombohedral twinning always reaches its minimum value (see Fig. 44(b)).

The microscopic inspection of the indentation impression produced by a spherical indenter on the (10$\bar{1}$0) plane of sapphire (Fig. 47) confirmed the theoretical prediction. Indeed, for a high-indentation load, the twin lamellae appear close to $\mu = 0°$, $\mu = 135°$, and $\mu = 225°$ orientations

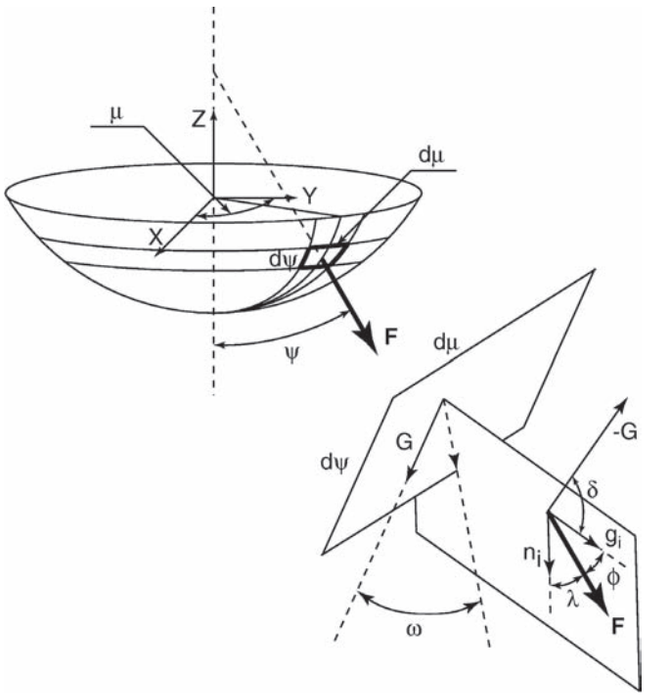

Figure 43. A geometric relationship between a spherical indenter and the ith slip system denoted by normal to the slip plane ($\boldsymbol{n}_i$) and slip direction ($\boldsymbol{g}_i$). $\boldsymbol{F}$ is the force perpendicular to the grid ($d\mu \in d\psi$) and $\boldsymbol{G}$ determines the intersection between the plane of indenter symmetry and the tangent to a grid. Coordinates μ and ψ denote the position of the grid. Reprinted with permission from [99], R. Nowak et al., *Philos. Mag*. A74, 171 (1996). © 1996, Taylor & Francis.

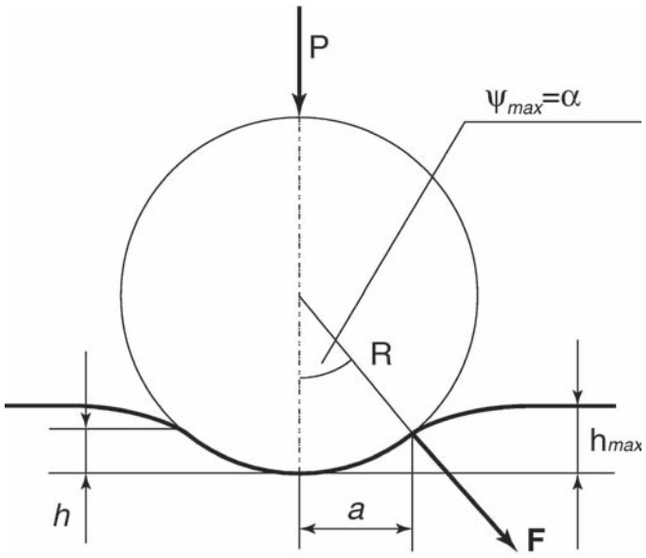

Figure 44. The geometry of the elastic–plastic indentation contact of a spherical indenter of radius R loaded by the force P. The contact area is a function of its radius a, the angle ψ_{max}, indentation depth h, and the total indentation depth h_{max} affected by a surface deflection. Reprinted with permission from [99], R. Nowak et al., *Philos. Mag*. A74, 171 (1996). © 1996, Taylor & Francis.

with a particularly intensive twinning in the area $\mu = 0°$ (Fig. 47(a)). The crystal volume close to directions $\mu = 90°$ and 270° was deformed elastically or by slip, and there was no trace of twins in these regions, as predicted by the model (compare Figs. 45 and 47).

Similar analysis [99] was successful in the case of the indentation of the (0 0 0 1) plane. The extreme values of the T parameter were achieved again for rhombohedral and basal twinning systems (Fig. 46). Although the shape of impressions on the (0 0 0 1) plane of sapphire exhibits irregularities, the predicted threefold symmetry can be deduced from the micrograph (compare Figs. 46 and 48(a)). When all the preferred slip–twinning systems – that is, those with the maximum value of T parameter in a given interval of the variable μ – are activated, the deformation zone is expected to posses a sixfold symmetry (Fig. 46(b)), which was observed by the SEM technique (Fig. 48(b)). A deviation from the ideal deformation pattern has occurred in the fractured areas.

These results [99] agree with the findings by Farber et al. [241, 242], who studied in detail the dislocation structure generated by Vickers indentation in the basal plane of sapphire. Moreover, Farber et al. [242] claim that, for room temperature indentation, twinning and cracks are the principal features in the sapphire plastic zone, as is confirmed by the theoretical prediction and experimental observations presented by Nowak et al. [99].

The above considerations formed a basis of more exact modeling of stress field under the acting spherical tip using 3D FEM modeling of anisotropic solid with the point symmetry of sapphire (see Fig. 49). The obtained results [77, 206] correctly reflected and therefore clarified (Fig. 50) the origin of the specific surface patterns (Figs. 47 and 48), which have been attributed to the combined response of basal and rhombohedral twinning proving the accurate prediction of previously applied ERSS models [99, 132, 205].

Sudden Depth Excursions during Nanoindentation in Sapphire. Using their ERSS model [99, 132, 205] and independently FEM simulations [77, 206] for a spherical contact (see the preceding section), Nowak et al. clarified the origin of the surprising discontinuities which appear in the loading part of the $P-h$ curves recorded for spherical indentation in the $(10\bar{1}0)$ and (0 0 0 1) planes of sapphire (see Figs. 50, 51(b), 51(c), and 52). Similar sudden indentation depth excursions were earlier reported by O'Hern et al. [29], Nowak et al. [8], and Nowak and Sakai [46, 193] (Figs. 23(d) and 41(c)) for high-load indentation in the (0 0 0 1) plane of sapphire with Vickers, Knoop, and Berkovich tips, respectively. The singularities for spherical indentation (Figs. 51 and 52) occur at considerably higher-indentation loads [99, 132] than those reported by Page et al. [24], which led us to argue that, apart from the noted similarities, the high-load discontinuities should be attributed neither to the initial generation of dislocations discussed in Page et al. [24] nor trivially explained as a sudden increase of crystal plasticity [29].

In the case of spherical indentation in the $(10\bar{1}0)$ and (0 0 0 1) planes of sapphire, pure elastic deformation dominates the initial stages of penetration up to relatively high loads (Figs. 51(a) and 51(b) , and curve 1 in Fig. 52(a)).

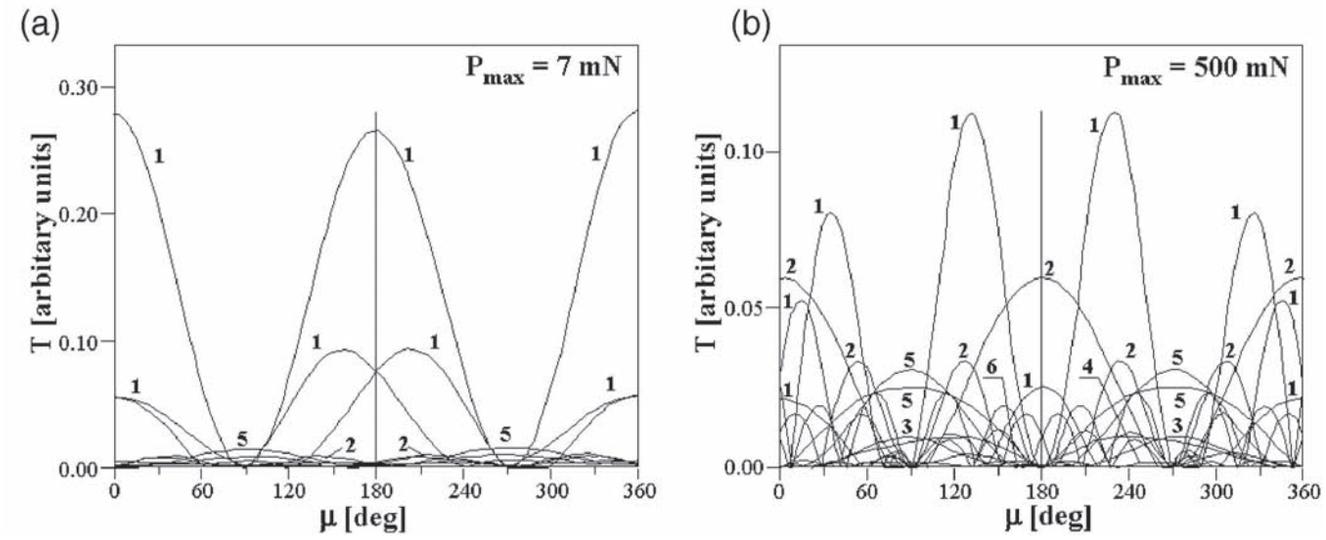

Figure 45. The prediction of the slip and twinning systems for the $(10\bar{1}0)$ plane of sapphire according to the model by Nowak et al. for P_{max} = 7 mN (a) and P_{max} = 500 mN (b). The numbers of the curves correspond to rhombohedral twinning (1), basal twinning (2), rhombohedral slip (3), basal slip (4), prismatic slip (5), and pyramidal slip (6). Reprinted with permission from [99], R. Nowak et al., *Philos. Mag.* A74, 171 (1996). © 1996, Taylor & Francis.

Frequently, an elastic deformation is suddenly interrupted by a plastic response, registered as a large pop-in in the loading cycle of the $P-h$ relationship. This takes place at indentation load levels close to 200 mN for the $(10\bar{1}0)$ plane (Figs. 45(b) and (c)) and around 400 or 500 mN, when indenting the (0 0 0 1) plane (curve 2 in Figs. 52(a) and (b)), independent of the accompanying fracture processes [99].

The characteristic loads for which the pop-in have been registered on the $(10\bar{1}0)$ plane scales with the distance of the twin lamellae from the center of the impression. Indeed, the closer the location of the large twin to the center of the impression, the lower the formation load of the popin (see Fig. 53) , which proves the relationship between the pop-ins and twinning.

Although the twin lamellae are not visible on the (0 0 0 1) crystal surface (Fig. 48), the large pop-in (Fig. 52) is caused again by twinning [99]. In exceptional cases, twinning may occur in the very small volume of material under the indenter at early stages of indentation and expand by tiny steps to the adjacent material. It is reflected in a quasi-smooth shape of the selected $P=h$ curves (curve 3 in Fig. 52(a)) and by the fact that both of the loading curves (curves 2 and 3 in Fig. 52(a)) reach an identical maximum point. The latter indicates that the same volume of sapphire has been transformed into a twinned phase.

Finally, the authors [132] identified the slope of the twin in order to provide an independent crystallographic analysis of the linear surface features appearing near the

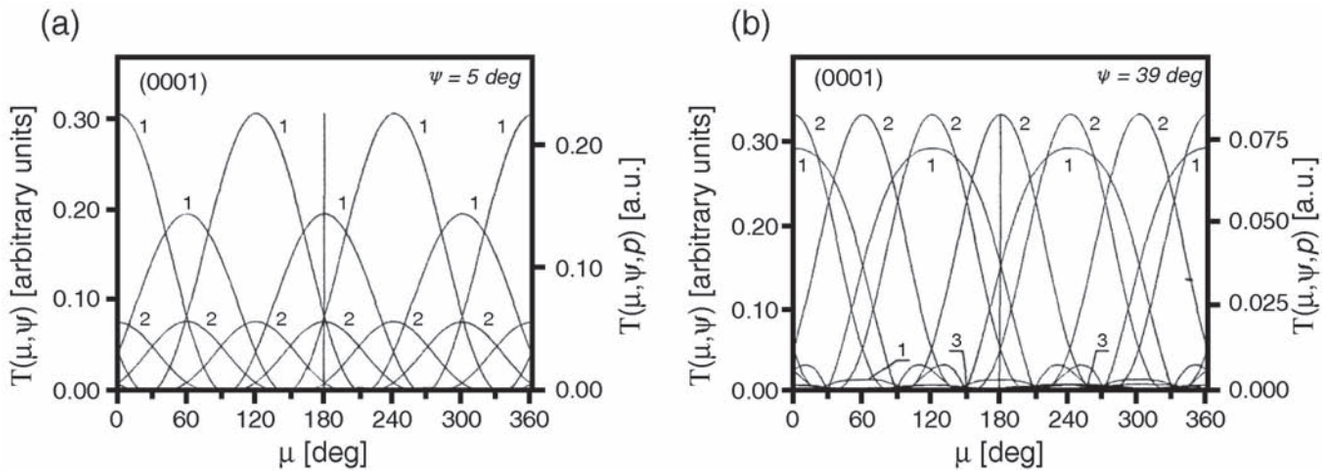

Figure 46. The prediction of the slip and twinning systems for the (0 0 0 1) plane of sapphire for P_{max} = 7 mN (a) and P_{max} = 500 mN (b). Reprinted with permission from [99], R. Nowak et al., *Philos. Mag*. A74, 171 (1996). © 1996, Taylor & Francis.

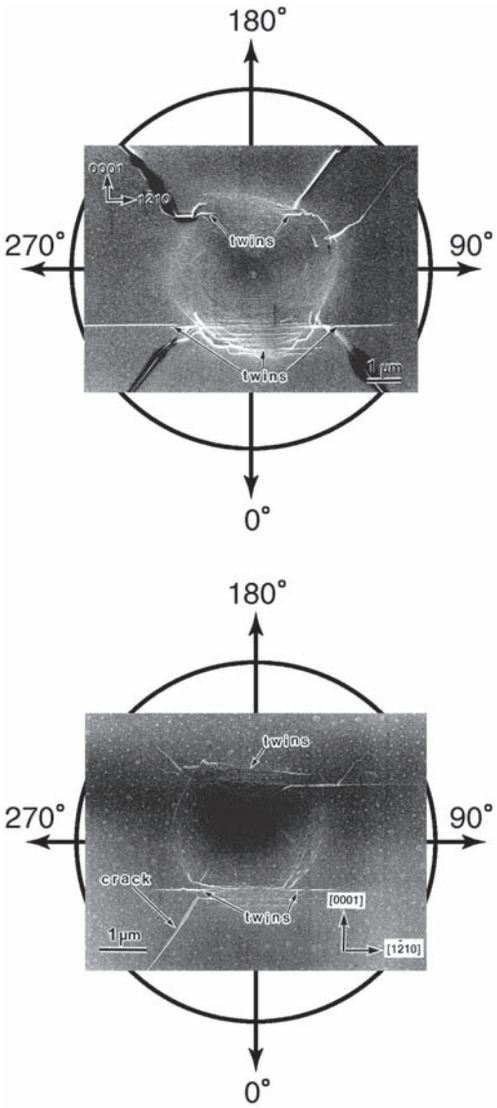

Figure 47. Micrographs of the surface features near the impressions on the $(10\bar{1}0)$ plane of sapphire obtained under the maximum load $P_{max} = 500$ mN (a) and 200 mN (b). Reprinted with permission from [99], R. Nowak et al., *Philos. Mag*. A74, 171 (1996). © 1996, Taylor & Francis.

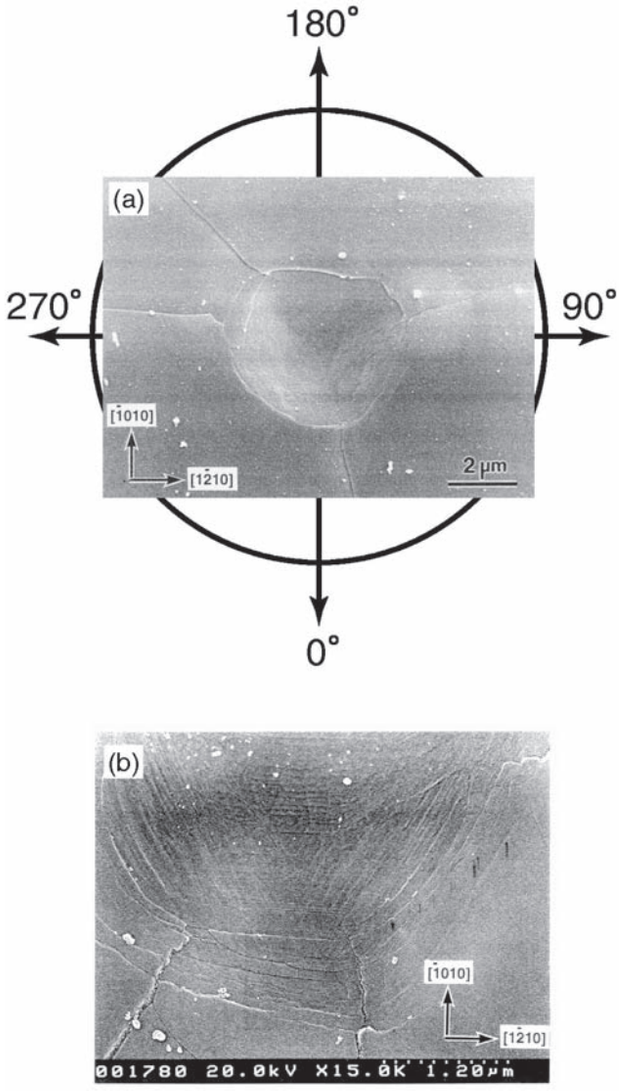

Figure 48. Micrograph of the spherical indentation impression on the (0 0 0 1) plane of sapphire obtained under the load of $P_{max} = 500$ mN (a). The details of the surface deformation are shown in the micrograph (b). Reprinted with permission from [99], R. Nowak et al., *Philos. Mag*. A74, 171 (1996). © 1996, Taylor & Francis.

indentation impressions on the $(10\bar{1}0)$ plane of sapphire (Fig 47). The study demonstrated that it is unlikely that the observed surface eruptions are caused by rhombohedral twinning exclusively. Indeed, the surface features were formed owing to the co-operative action of rhombohedral and basal twinning since the value of the $(10\bar{1}0)$ surface tilt $-39°$ (Fig. 54) can be achieved only by the co-operative action of two twinning systems.

The concept of co-operation of two twinning systems fits the prediction of the ERSS model and FEM calculations (see the precedent section), which indicate the high probability of activation of twinning as far as the indentation in the $(10\bar{1}0)$ plane is concerned. Interestingly, twinning has not been accounted for by other reports on "nonlinear deformation mechanisms during indentation" (see the review by Bahr et al. [112]), while it came recently into intense investigation [25, 28, 234].

4.5.4. Concluding Remarks on the Indentation of Sapphire

The present review provides an example of the application of the theoretical analyses to the nanoindentation of sapphire. Despite the complicated structure of the Al_2O_3 crystal, which exhibits low *R3C* symmetry, and a number of available deformation systems which may eventually be activated during indentation, phenomena associated with its surface deformation induced either by sharp or spherical indenters were successfully clarified [46, 77, 99, 132, 193, 205, 206]. The deformation mechanisms, that is, slip and twinning systems responsible for indentation behavior of α-alumina crystal were precisely predicted by the ERSS model, and subsequently confirmed by microscopic observations. The sequence of hardness for various orientations of sapphire surface was clarified in terms of "true hardness" introduced by the EPI method.

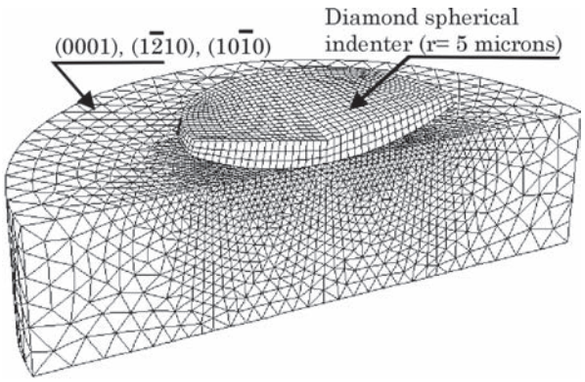

Figure 49. FEM mesh constructed in order to model the contact between variously oriented, elastically anisotropic sapphire crystal and deformable, and spherical diamond tip. Reprinted with permission from [206], R. Nowak et al., *JSME Int*. J. A 46, 265–271 (2003). © 2003, The Japan Society of Mechanical Engineers.

In order to compare the results obtained from their ERSS simulation and the outcome of the EPI analysis, the true hardness values H_T obtained for various orientations (N, R) of the triangular indenter on different crystallographic planes (Fig. 22) and the theoretical hardness $\widetilde{H}$ calculated according to eqn (4.24) are illustrated in Figure 55. Respective hardness values were normalized with these for the (0 0 0 1)N basal orientation. The quantitative agreement between the true hardness H_T and the hardness $\widetilde{H}$ based on the predicted slip–twinning activity in deformed crystal was achieved. A discrepancy for the hardest (10$\bar{1}$0) N orientation may have been caused by the overestimation of the critical stress for twinning and by the indentation-induced cracks, which change the stress state under the tip.

The clarification of the origin of the sudden depth excursion observed in the loading cycle of the registered $P-h$ indentation curves, as well as explanation of the nature of the linear features in the vicinity of the residual indentation impressions made on the (10$\bar{1}$0) plane, accounts for the success of the presented approach. The precise location of the surface features was predicted by the models pointing toward the twinning process as the most probable source of the observed surface eruptions. Further identification of the slopes of a twin region provided an independent crystallographic analysis of the linear features appearing near the indentation impressions on the (10$\bar{1}$0) plane of sapphire, which proved that they were formed as a result of the co-operative action of basal and rhombohedral twinning. Thus, the controversial issue [77, 99, 132, 193, 205, 206] of the origin of linear features around indentation impressions in sapphire was finally solved, while recent nanodeformation measurements served as negative verification of Oliver–Pharr method (see Fig. 9).

4.6. Indentation of Thin Films and Ion-Implanted Surfaces

4.6.1. Indentation of HfN Films Sputter Deposited on Silicon Substrate

The nanoindentation technique is considered the most convenient tool for studying mechanical properties of thin films.

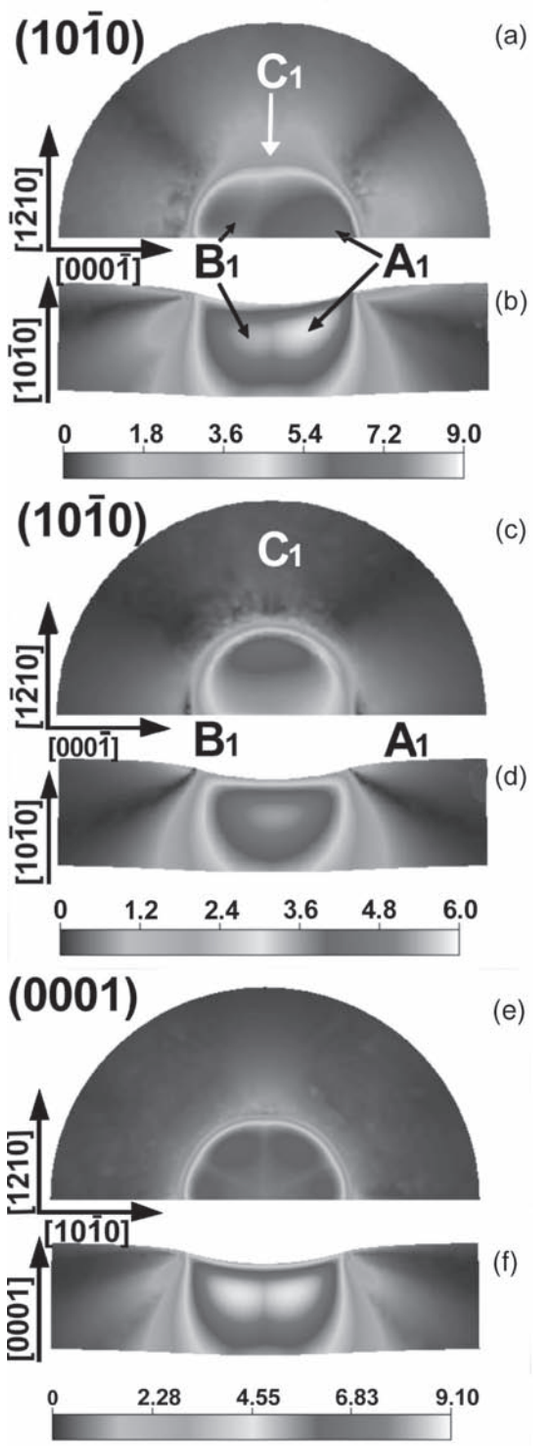

Figure 50. The distribution of the shear stress (scale in GPa) for rhombohedral twinning (a) and (b) and prismatic slip (c) and (d), near the spherical tip loaded onto the (1 0 1 -bar 0) plane of sapphire. The horizontal cross sections (a and c) are located 0.2 μm under the surface, while the vertical (b and d) illustrate the depth profile of shear stress. The regions A1, B1, and C1 correspond to the different crystal areas defined in [77, 206]. The analogous distribution of shear stress in twinning systems for indentation in the (0 0 0 1) plane is presented in (e) and (f). Reprinted with permissions from [77], R. Nowak et al., *Appl. Phys. Lett*. 83, 5214 (2003). © 2003, American Institute of Physics.

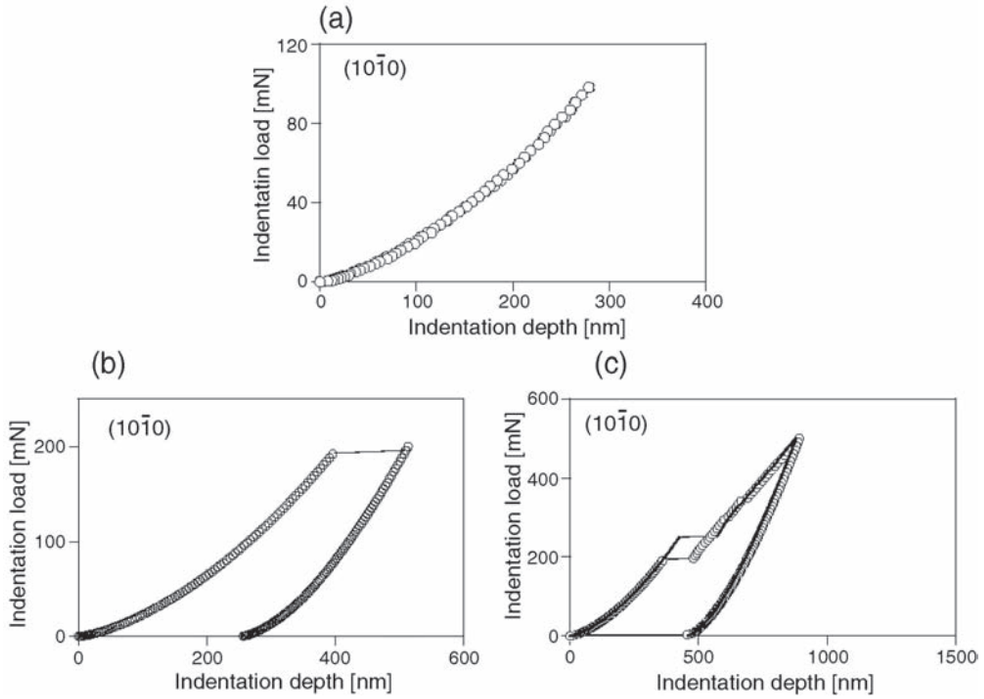

Figure 51. The $P-h$ curves for spherical indentation in the $(10\bar{1}0)$ plane of sapphire obtained under the load P_{max} = 100 mN (a), 200 mN (b), and 500 mN (c). Reprinted with permission from [99], R. Nowak et al., *Philos. Mag*. A74, 171 (1996). © 1996, Taylor & Francis.

Moreover, the first nanoindentation testers were designed to examine the coatings [13], and since its inception, the method has been used to examine both hard [247, 248] and soft [16, 124, 249] thin layers. Since it is particularly difficult to investigate the surface deformation of ultrahard thin films, this review concentrates on the nanoindentation studies of sputter-deposited hard HfN layers.

HfN thin films are inherently brittle in comparison with metallic layers, while their high activation energy against electromigration, coupled with excellent conductivity, has already attracted considerable attention. This material seems to be better suited for diffusion barriers in electronics than TiN, since there has been no report on the interfacial brittle layer being formed when depositing HfN, despite the observation of such an effect for Ti–N system [250]. Furthermore, HfN was found [251] to be an effective diffusion barrier between the silicon and aluminum, while Yamanaka et al. [252] discovered a new layer-structured superconductor based on HfN.

An interest in HfN films emerged two decades ago, when their considerable hardness and excellent wear resistance

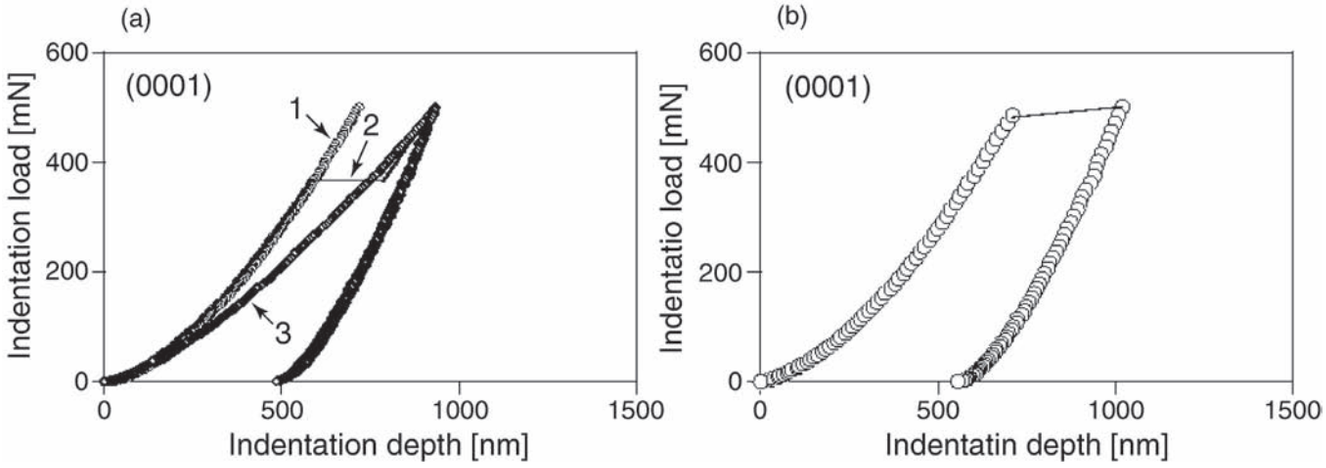

Figure 52. The $P-h$ curves for spherical indentation in the (0 0 0 1) plane of sapphire under the load P_{max} = 500 mN. The curves denoted by 1, 2, and 3 show perfectly elastic, elastic–plastic, and transition-type deformation, respectively (a). The combination of perfectly elastic and perfectly plastic responses exhibits hysteresis (b). Reprinted with permission from [99], R. Nowak et al., *Philos. Mag*. A74, 171 (1996). © 1996, Taylor & Francis.

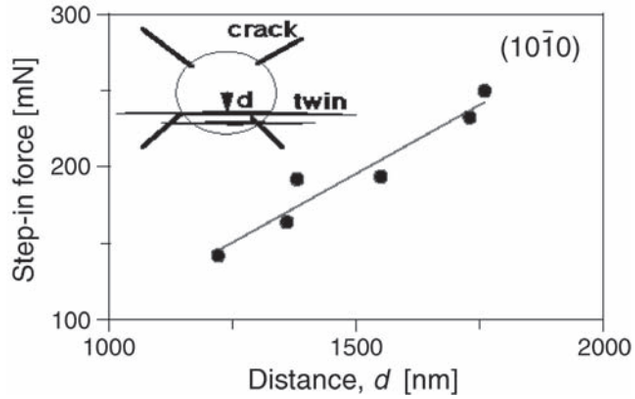

Figure 53. Relationship between the pop-in force and the location of the first twin lamellae produced under spherical indenter acting on the (10$\bar{1}$0) plane. The distance *d* between the center of the indentation and the twin is defined in the inlet. Reprinted with permission from [99], R. Nowak et al., *Philos. Mag*. A74, 171 (1996). © 1996, Taylor & Francis.

came to be widely recognized, and were immediately applied in the manufacture of cemented carbide cutting tools. Since HfN films have additionally been found useful in the electronic industry, their physical properties have been studied in terms of deposition conditions and their particular structure. An example is the study of the structure as well as electrical and mechanical properties of HfN films deposited on silicon by a reactive r.f. sputtering method [253]. This information was obtained by means of the thin-film X-ray diffraction method, Auger electron spectroscopy, and electron microscopy, while the nanoindentation results were analyzed using the EPI approach. The authors [253] emphasized the correlation between the deposition conditions of HfN films and the resulting structure, which affects both their electrical (resistivity) and mechanical (mechanism of deformation, residual stress) properties.

Interestingly, the hardness data reported for HfN films by various authors appear inconsistent (see Table 5) despite the apparent similarity of investigated layers in terms of their

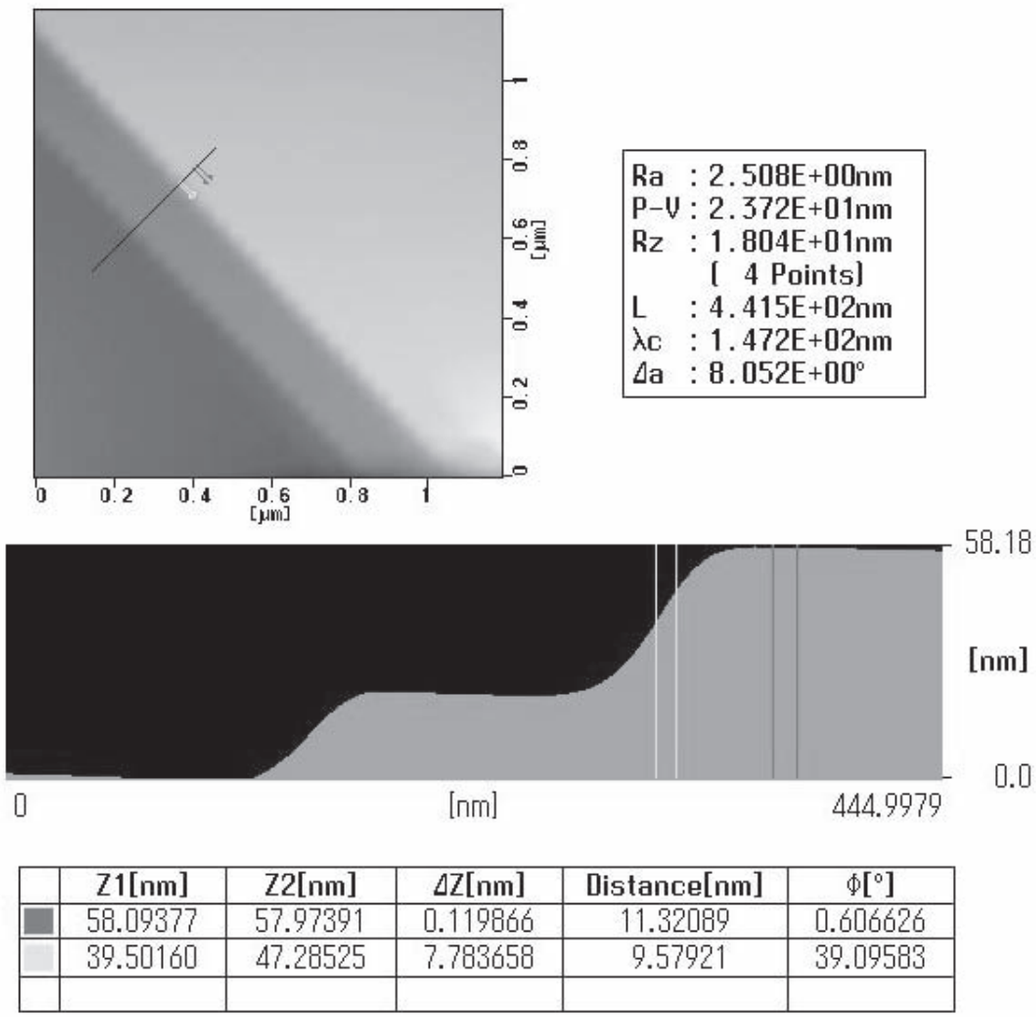

	Z1[nm]	Z2[nm]	ΔZ[nm]	Distance[nm]	φ[°]
	58.09377	57.97391	0.119866	11.32089	0.606626
	39.50160	47.28525	7.783658	9.57921	39.09583

Figure 54. The AFM cross section of the linear feature which appeared in the vicinity of the residual impression (P_{max} = 500 mN) on the (10$\bar{1}$0) plane of sapphire crystal, highlighting the slope of the defected region with respect to the original surface orientation. Reprinted with permission from [132], R. Nowak et al., *Acta Mater*. 47, 4329 (1999). © 1999, Elsevier.

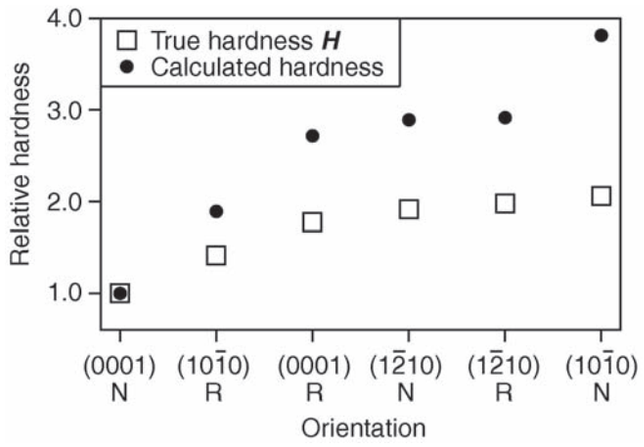

Figure 55. The true hardness $\boldsymbol{H}_1$ and the theoretical hardness $\widetilde{H}$ calculated for various orientations of Berkovich indentations in sapphire. The values were normalized with those obtained for the (0001)N orientation. Reprinted with permission from [193], R. Nowak and M. Sakai, *Acta Metall. Mater*. 42, 2879 (1994). © 1994, Elsevier.

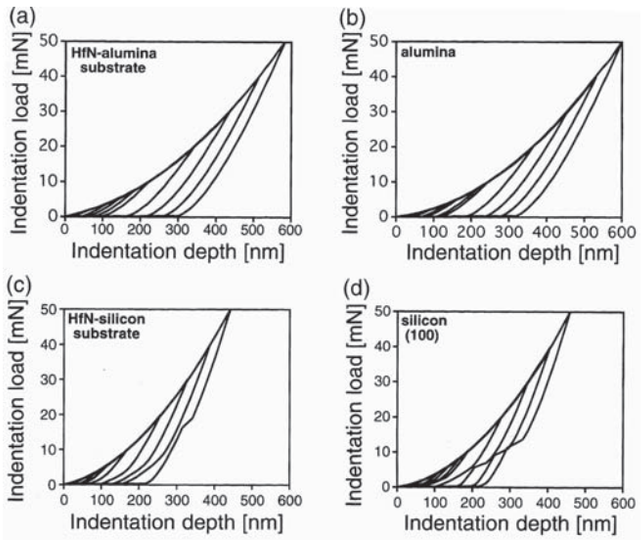

Figure 56. *P–h* curves obtained for HfN on alumina substrate (a), alumina substrate alone (b), HfN on silicon substrate (c), and silicon wafer (d). The indentation load P_{max} applied to Berkovich indenter ranged between 2 and 50 mN. Reprinted with permission from [254], R. Nowak et al., J. Mater. Res. 12, 64 (1997). © 1997, Materials Research Society.

composition and morphology. Therefore, Nowak et al. [254] used nanoindentation to examine the HfN layers sputter deposited onto silicon and alumina substrates to discover a reason for the reported discrepancies. Indeed, the large disagreement in experimental results (Table 5) raises doubts as to whether the hardness test in its conventional form is applicable for HfN films. Radical steps to improve the accuracy of the examination of HfN hardness have already been undertaken, either by measuring the size of residual indentation impressions by means of the SEM technique [2] or by placing the tester itself inside the column of the scanning electron microscope [256].

The major advantage of the nanoindentation claimed for thin films is that it provides results not affected by the substrate properties. The assumption is that very shallow penetration of the indenter insures that deformation of the substrate will not occur. However, the observations of Hainsworth et al. [248] and of Shiwa et al. [65], which concerned HFs deposited on softer substrates (SSs), raised doubts as to the correctness of the above thesis, and prompted us [254] to perform independent research concerning HfN–silicon and HfN–alumina systems.

Examples of the *P–h* curves for 300 nm thin HfN films deposited on silicon and alumina as well as for substrate materials themselves are depicted in Figure 56. The nanoindentation experiments revealed significant differences in the deformation of HfN films deposited on different substrates (compare Figs. 56(a) and 56(c)). The HfN layers grown on silicon (Fig. 56(c)) were harder than those prepared on alumina (Fig. 56(a)), reflecting their substrate material behavior (compare Figs. 56(d) and 56(b)). Furthermore, the characteristic pop-outs appearing during the unloading of silicon (Fig. 56(b)), which reflect the pressure-induced phase transformation [49], have similarly been observed for HfN deposited on a silicon wafer (Fig. 56(c)).

Furthermore, the conventional hardness value calculated from the depth-sensing data [254] reflected the relationship between the film properties and its substrate (Fig. 57). The difference in hardness between each of the nitride films

Table 5. Hardness of HfN films reported in the literature.

Hardness	Deposition process	Substrate	Indentation load	Reference
KHN 1850-2420 kgf mm^{-2} (18.13–23.72 GPa)	Activated reactive evaporation	Tantalum, stainless, high-speed steel	490 mN	R. Nimmagada et al., *Thin Solid Films* 63, 327 (1979)
KHN 1650±100 kgf mm^{-2} (16.17±0.98 GPa)	rf sputtering	Stainless steel	98 mN	A. Grill et al., *Thin Solid Films* 108, 173 (1983)
HV 2570 kgf mm^{-2} (26.95 GPa)	High-rate reactive sputtering	Glass, steel	9800 mN	[250, 255, 256]
HV 2800-3500 kgf mm^{-2} (27.44–34.3 GPa)	Reactive magnetron sputtering	Glass, steel	245 mN	
HV 2800-6000 kgf mm^{-2} (27.44–58.8 GPa)	Reactive magnetron sputtering	High-speed steel	10 mN, 19 mN 1000 mN	

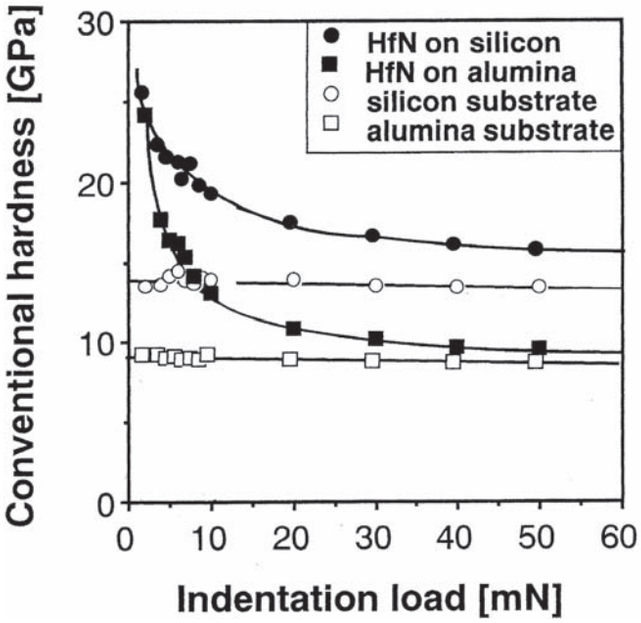

Figure 57. Conventional hardness of HfN thin films deposited in alumina and silicon wafer as well as their substrates, as a function of the indentation load P_{max}. Reprinted with permission from [254], R. Nowak et al., *J. Mater. Res.* 12, 64 (1997). © 1997, Materials Research Society.

and its substrate increases rapidly for descending indentation loads. This enabled Nowak et al. [254] to qualify the increase in HfN hardness as one that is caused by the decreasing contribution of the substrate. The authors suspected, however, that what they were witnessing for low loads was merely a decrease in the substrate effect, and the absolute hardness value of HfN was largely undetermined. Their conclusion runs to counter the common belief that the ratio of indentation depth to film thickness is lower than 1:10, allowing one to disregard the substrate effect [257].

Furthermore, the linear relationship [eqn (4.12)] predicted by the EPI theory was consequently confirmed by the data registered for the investigated materials (Fig. 58). The values of true hardness are listed in Table 6, while the results for sapphire are illustrated in Figure 58 for the purposes of comparison.

Surprisingly, the diagrams suggest that the HfN film deposited on alumina is softer than the alumina substrate itself, while there is almost no difference in hardness between the nitride film and its silicon substrate (Table 6). This effect was attributed to indentation cracking occurring in the film's volume and along the film–alumina interface owing to the superposition of high internal stress and indentation stress field [253, 254].

Hardness of the HfN films obtained by ultrashallow indentation appeared to be higher (Fig. 58(b)) than estimated for moderate loads (Fig. 58(a)) and exceeded the hardness value of the related substrate (Table 6). However, even in the range of minimal indentation depths, one may still find evidence of the substrate effect on the HfN indentation data. This is caused by the mechanism introduced by

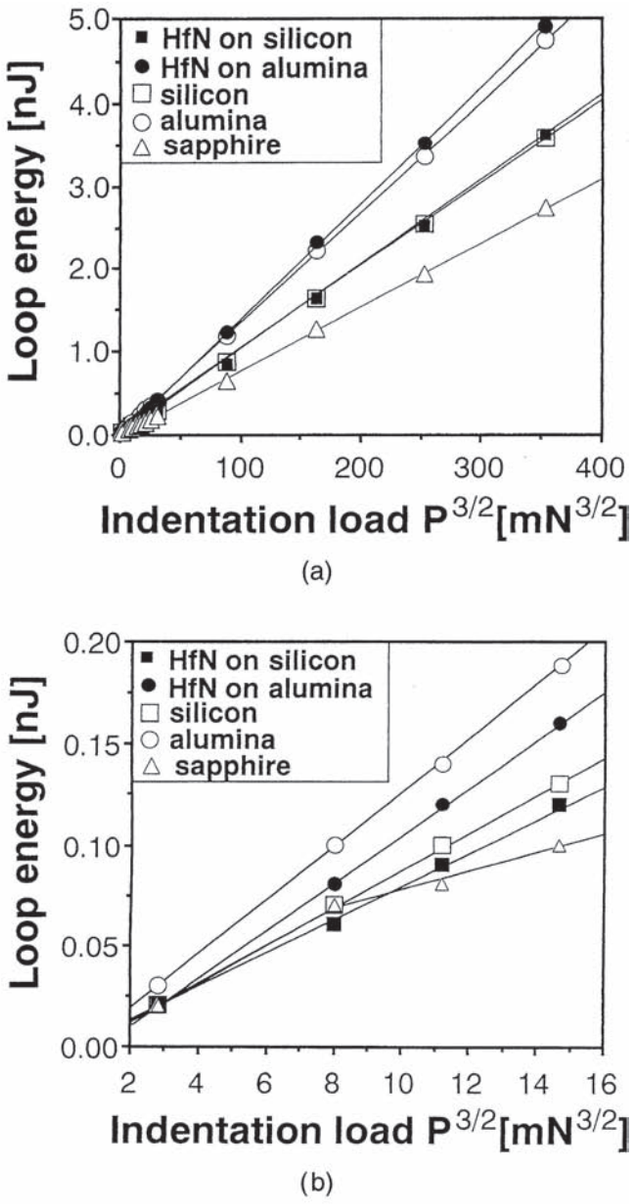

Figure 58. The U_r–$P_{max}^{3/2}$ relationship for HfN films deposited on silicon and alumina, their substrates, and bulk sapphire crystals registered for moderate (a) and low (b) indentation loads. Reprinted with permission from [254], R. Nowak et al., *J. Mater. Res.* 12, 64 (1997). © 1997, Materials Research Society.

Shiwa et al. [65]. The latter observed that TiN layers fail to deform plastically under an indenter, and is instead pushed inside the soft silicon substrate. A similar phenomenon for carbon coatings on steel is discussed in [248].

The EPI theory allows us to determine the hardness sequence of the investigated materials and comment on the anomalies caused by the substrate effect. Since there is no physical basis for defining conventional hardness, the authors did not use the models separating the coating hardness from that of the film–substrate composite; these are obtainable from the literature (see, e.g. [257]).

Table 6. Hardness H_T calculated for HfN thin films according to EPI theory [195].

Material	Hardness H_T (2 mN ≤ P_{max} ≤ 50 mN	Regression coefficient	Hardness H_T (2 mN ≤ P_{max} ≤ 6 mN	Regression coefficient
HfN on silicon	26.3	1.000	38.1	0.994
HfN on alumina	13.9	1.000	19.5	0.987
Silicon	26.6	1.000	31.7	0.999
Alumina	15.3	1.000	15.7	0.997

4.6.2. Surface Deformation of Ion-Implanted Sapphire

Reports on radiation effects in sapphire and polycrystalline alumina are legion, since aluminum oxide has been considered for a long time a candidate for the first-wall insulator in fusion nuclear reactors. The early research with ion-bombarded alumina simulated in a controlled manner the conditions of radiation prevailing in a reactor core (see, e.g. [258]).

Following these early studies [259, 260] on the ion-bombarded Al_2O_3 crystals (see Table 7), McHargue et al. [261, 262] and Naramoto et al. [263, 264] reported a considerable increase in hardness and fracture toughness for sapphire implanted with Cr, Zr, or Ti ions. Furthermore, Farlow et al. [265, 266] investigated sapphire implanted with Fe, Mn, Ni, Ti, Cr, and Ge ions. They observed a considerable number of defects created in the modified area, which recombined during the implantation process. Such a phenomenon led to formation of a less-defected, crystalline near-surface region in Al_2O_3 bombarded by Al, Ga, In, Mn, Fe, Ni, Cu, Zn, Mo, and W ions with various energies and fluences (see Table 7). Farlow et al. found that the hardness variations correlate with the degree of lattice residual damage [265, 266]. Finally, a definitive study on the short-range order and changes of near-neighbor bond length in sapphire implanted with Fe ions was conducted by McHargue et al. [267, 268] using a number of techniques for surface characterization (Table 7).

Since in the ion beam–modified materials the volume available for experiments is quite small, the indentation technique appeared naturally as a method for investigating the mechanical properties of such solids. Consequently, a number of works reported low-load Vickers or Knoop hardness as the essential parameter characterizing modified surfaces [12, 261–265, 267–275]. However, a conventional hardness test is frequently inadequate for estimating the mechanical properties of the implanted region because of its limited accuracy. The results of the measurements are strongly affected by the presence of virgin material located directly beneath the ion-modified surface zone (the substrate effect).

Ever since the availability of nanoindentation testers (see pioneering publications by Newey et al. [11] and Pethica et al. [12]), they have been applied to ion-implanted metals [276, 277], and the first depth-sensing indentation in sapphire implanted with Cr ions was reported in 1991 by O'Hern et al. [29]. The latter registered the characteristic pop-in in the *P–h* curves for virgin sapphire indented with a load as low as 2 mN, the singularity undetected in the case of ion-modified crystal. The similar sudden depth excursions into the $(10\bar{1}0)$ plane when indented with Knoop indenter (see Section 4.5.3.2), which did not show up after bombardment with Au and Ni ions, were reported in 1992 [8]. Furthermore, Ensinger and Nowak [30–32] observed the depth excursions which appear at higher (2 mN) loads for the indented $(\bar{1}2\bar{1}0)$ plane of sapphire and disappear after modification of the surface with Ta^+ ions (refer to Table 7).

Since nanoindentation experiments with spherical tips are able to quantify the localized stress–strain behavior [48], Nowak et al. [278] studied the deformation of ion beam–modified sapphire induced by a spherical indenter. The indentation results supported by AFM observations revealed the difference in deformation of the $(10\bar{1}0)$ plane of sapphire when modified by bombardment with highly energetic Ni^{2+} and Au^{2+} ions (E = 3 MeV; a fluence 2×10^{16} cm^{-2}). The peak range of implanted species estimated by TRIM code calculations equalled 1140 and 680 nm for nickel and gold, respectively.

The registered *P–h* curves indicate minor differences in maximum penetration depth measured for virgin and ion-modified surfaces (Fig. 59(a)). They remain smooth, as in the case of those reported for the prismatic plane of sapphire (see Figs. 23(a)–23(c)). Closer inspection of the indentation data, however, revealed that the hardness is greatest for the Ni-implanted and minimal for the Au-implanted sapphire (Fig. 59(b)), as in the earlier Vickers and Knoop hardness tests [8]. The *P–h* curves for spherical indentations exhibited elastic response of virgin crystal with a distinct pop-in event registered for higher loads which characterized the onset of nonlinear behavior (Fig. 60), as previously observed by Nowak et al. [97, 130, 205], who attribute this effect to the location of the twin lamellae and the stage of the indentation. For the implanted Al_2O_3, the elastic regime was far more limited (Fig. 60). The onset from elastic to plastic response of the modified crystals using the load partial-unload tests was determined. This approach enabled the contact pressure and modulus to be determined before and after the pop-in event. In the case of the implanted material, the onset of plastic deformation was identified from the commencement of the splitting of the "loading points" (Fig. 61) using the analysis developed by Field and Swain (see Section 2.1.3).

The plots of contact pressure vs. depth for the virgin, gold, and nickel-implanted sapphire crystals (Fig. 62) show the contact pressure pre- and postpop-in event for the $(10\bar{1}0)$ plane of virgin Al_2O_3. The nickel-modified oxide shows a continuous rising contact pressure to a depth of ~200 nm reaching maximum value and, thereafter slightly declining with further penetration (Fig. 56(a)), while the

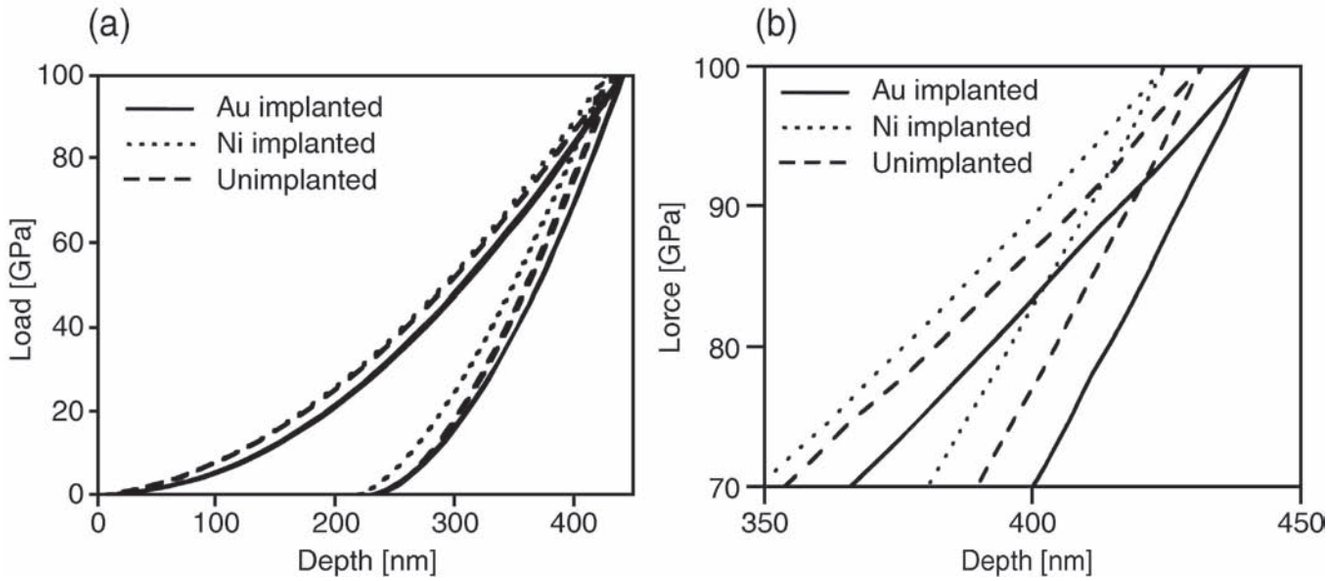

Figure 59. Indentation results for the plane of sapphire – virgin and modified with energetic Ni^{2+} and Au^{2+} ions – deformed with Berkovich tip (a). The higher resolution of the data near the maximum load is shown in (b). Reprinted with permission from [278], R. Nowak et al., *Mater. Sci. Eng.* A253, 167 (1998). © 1998, Elsevier.

data for gold-implanted Al_2O_3 tended to reach the value of the substrate (Fig. 62(b)).

Nowak et al. [278] determined variations of elastic modulus with the depth of penetration into the virgin and ion-modified sapphire (Fig. 63(a)), which show a constant value for the virgin material and a slightly lower value for the Ni, and significantly lower values for Au-implanted crystals. The elastic modulus of alumina crystal implanted with Au_{2+} ions increased uniformly with depth of penetration, whereas for the material modified with Ni_{2+} species, it exhibited a gradual increase toward the value characteristic of bulk sapphire. The modulus of the virgin material displayed tiny change when a pop-in occurred (Fig. 63(b)).

The authors [272] derived additional information from the plots of mean contact stress vs. contact strain (Fig. 64). They found that the virgin material exhibits linear (elastic) behavior to pop-in as anticipated from the elastic relationship between the mean contact pressure and the strain,

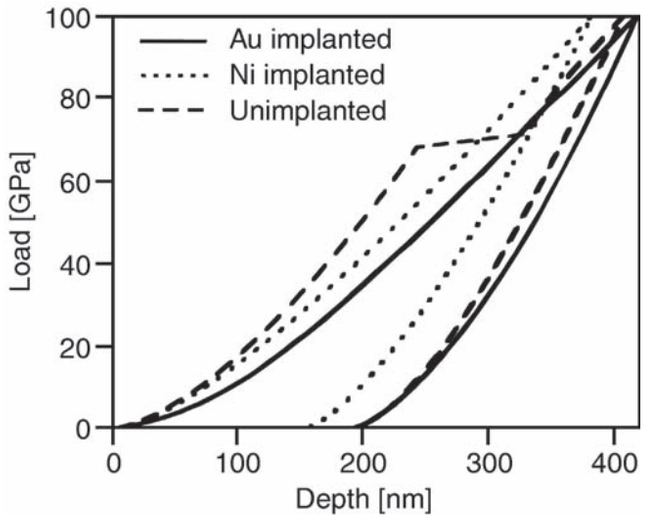

Figure 60. *P–h* curves of the plane of sapphire – virgin and modified, and modified with energetic Ni^{2+} and Au^{2+} ions – deformed by a nominally 2 μm radius spherical-tipped indenter. Reprinted with permission from [278], R. Nowak et al., *Mater. Sci. Eng.* A253, 167 (1998). © 1998, Elsevier.

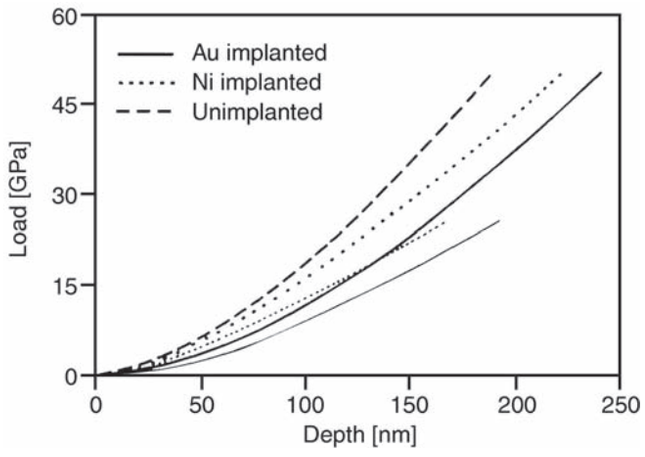

Figure 61. Load partial–unload force–displacement data obtained with the nominally 2 μm radius spherical-tipped indenter for unimplanted sapphire and modified with energetic Ni^{2+} and Au^{2+} ions. Reprinted with permission from [278], R. Nowak et al., *Mater. Sci. Eng.* A253, 167 (1998). © 1998, Elsevier.

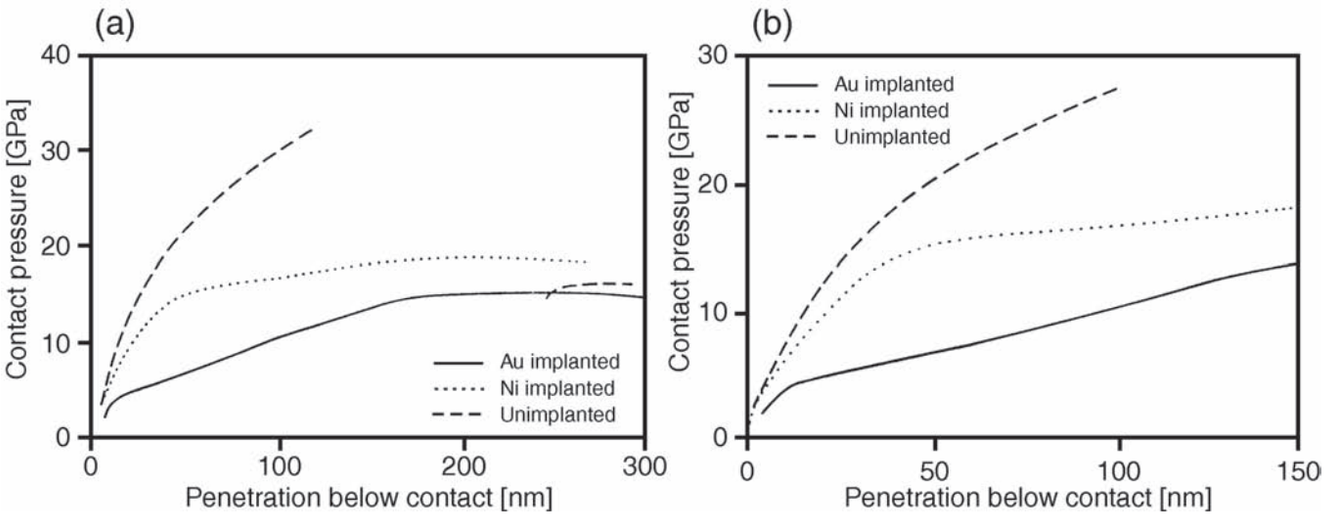

Figure 62. Plots of contact pressure vs. contact depth for the implanted and virgin sapphire with the nominally 2 μm radius spherical-tipped indenter; registered for maximum indentation load of 50 mN (a) and 100 mN (b). Reprinted with permission from [278], R. Nowak et al., *Mater. Sci. Eng.* A253, 167 (1998). © 1998, Elsevier.

while the Ni-implanted material showed two distinct slopes prior to the onset of yielding; a complex response was registered for Al_2O_3 implanted with Au ions (Fig. 64).

In order to explain the observed influence of the ion bombardment on the indentation behavior of the ion-treated sapphire, Nowak et al. calculated the values of displacement per atom (TRIM code) for their particular conditions. They were up to 31 and 120 dpa, with the maximum occurring at a depth of 460 nm for the Au and 1000 nm for the Ni, respectively. Hence, the authors conclude that sapphire modified by the nickel was considerably within the crystal damage dose, while the implantation with gold approached the amorphization level. In the latter case, it was expected [278] that small gold particles might have formed because of the exceptionally low solubility of Au in sapphire. Moreover, they suspected that the excessive number of Frenkel pairs induced by bombardment with very massive Au ions would result in the formation of numerous dislocation loops and, in turn, that sapphire would exhibit plastic behavior. Ni implantation on the other hand, as is the case with most implanted species, may form vacancies and interstitials resulting in the development of compressive stresses within the implanted layer [278].

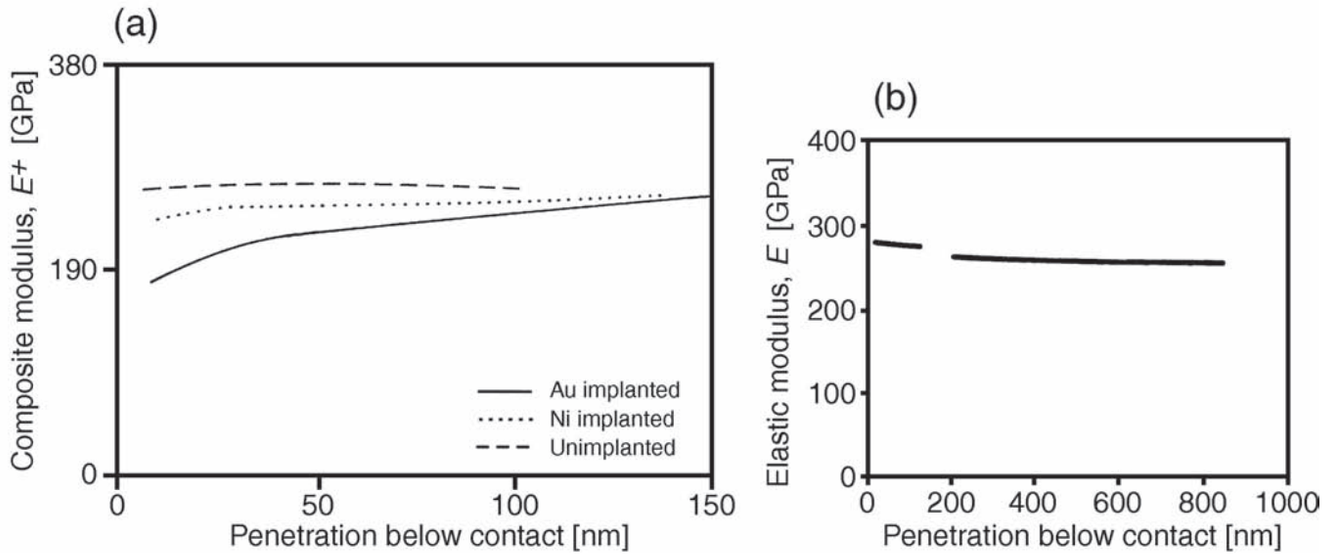

Figure 63. Effective elastic modulus [eqn (2.13)] vs. depth of penetration for the unimplanted and ion-modified sapphire, registered for maximum indentation load of 50 mN (a) and 500 mN (b). Reprinted with permission from [278], R. Nowak et al., *Mater. Sci. Eng.* A253, 167 (1998). © 1998, Elsevier.

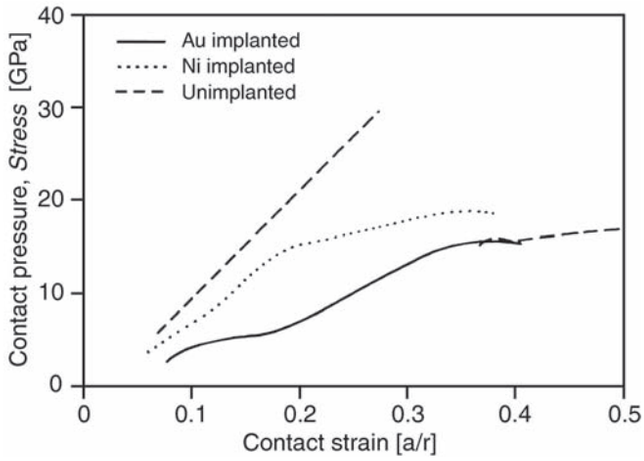

Figure 64. Plots of mean contact pressure (stress) vs. contact strain for the unimplanted and ion-modified sapphire. Reprinted with permission from [278], R. Nowak et al., *Mater. Sci. Eng.* A253, 167 (1998). © 1998, Elsevier.

The present section provides an example of an alternative to the EPI-method approach to the indentation data recorded for crystals. The studies reviewed suggest that experiments with spherical indenters are able to distinguish the influence of ion implantation resulting in mild and more severe damage of sapphire crystal lattice. The unimplanted aluminum oxide was characterized by a sharp pop-in of plastic deformation at contact stresses considerably in excess of the steady state hardness of the material, while the elastic modulus was slightly reduced for the alumina crystals bombarded with Ni^{2+} ions and initially significantly changed for aluminum oxide modified with Au^{2+} ions.

It would be difficult to draw similar conclusions using experimental techniques other than nanoindentation since the implanted species reside beneath the surface, forming a complex layered structure on the substrate. There is a relatively thin modified layer of near-pristine material on the sapphire overlaying the lattice-damaged zone, which requires surface-probing investigations.

4.6.3. Indentation of the Ion Beam–Modified Thin Films

Nanoindentation is useful in quite a new and rapidly expanding area, – postdeposition ion-beam treatment of thin films and multilayer structures – which offers unexpected opportunities for modifying the film's physical properties, hitherto controlled exclusively by deposition conditions [279]. Furthermore, nanoindentation of ion-modified thin films is currently considered an important tool for the characterization of microelectromechanical systems (MEMSs) [280–282].

The modification of thin films by ion bombardment has concentrated mainly on improving the tribological properties [283], the determination of the damage within the collision cascade [284], the bombardment-induced grain growth [285], variations in film composition [286], and the structure [287]. In contrast, Nowak et al. [288–292] performed the nanoindentation in HfN thin films as complementary experiments to the complex program that aimed to resolve the problem of postdeposition relaxation of the ultra-high internal stresses after ion treatment of these films. This resulted in detection of the amorphous silicon interlayer formed by ion treatment beneath the examined film. Furthermore, Perry et al. [293] and Manory et al. [294, 295] used nanoindentation to characterize the mechanical properties of the ion beam–modified TiN coatings on steel.

Detection of an Amorphous Silicon Interlayer by Indentation [232, 236]. The HfN films sputter deposited on silicon were modified by bombardment with Si^+ ions [288, 292] in a beam perpendicular to the film's surface (Fig. 65). The conditions of the ion-beam treatment are given in Figure 65. Based on the numerically determined (TRIM code) peaks of the distribution profile of Si^+ ions in HfN, they were matched by the authors in such a way as to assure collision between the incident ions and HfN everywhere in the volume of the 600, 300, and 200 nm thin films (see Fig. 65). The nanoindentation in virgin and ion-modified HfN was performed [292] for thicker films (600 nm) to minimize the substrate effect. Their *P–h* curves, registered for maximum load of 20 mN (Fig. 66(a)), indicate a considerable increase in the indentation depth and the energy expended for irreversible deformation (compare the area bounded by *P–h* graphs) for the modified films The singularity PT in Figure 66(a) caused by the stress-induced phase transformation in silicon substrate, which was recorded for virgin HfN, is not present for ion-bombarded layer.

Hence, the authors were aware that their results were still affected by the deformation of the silicon substrate, as in the case of the TiN–Si system studied by Shiwa et al. [65], and conclude that the lack of singularities for

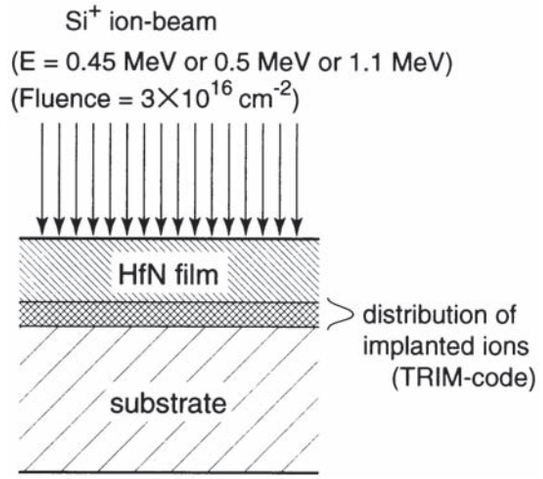

Figure 65. A schematic illustration of postdeposition ion beam modification applied to HfN thin films grown on silicon wafer by reactive sputtering method. The distribution profile of the implanted species was designed based on computer simulation. Reprinted with permission from [291], R. Nowak et al., *J. Appl. Phys.* 85, 841 (1999). © 1999, American Institute of Physics.

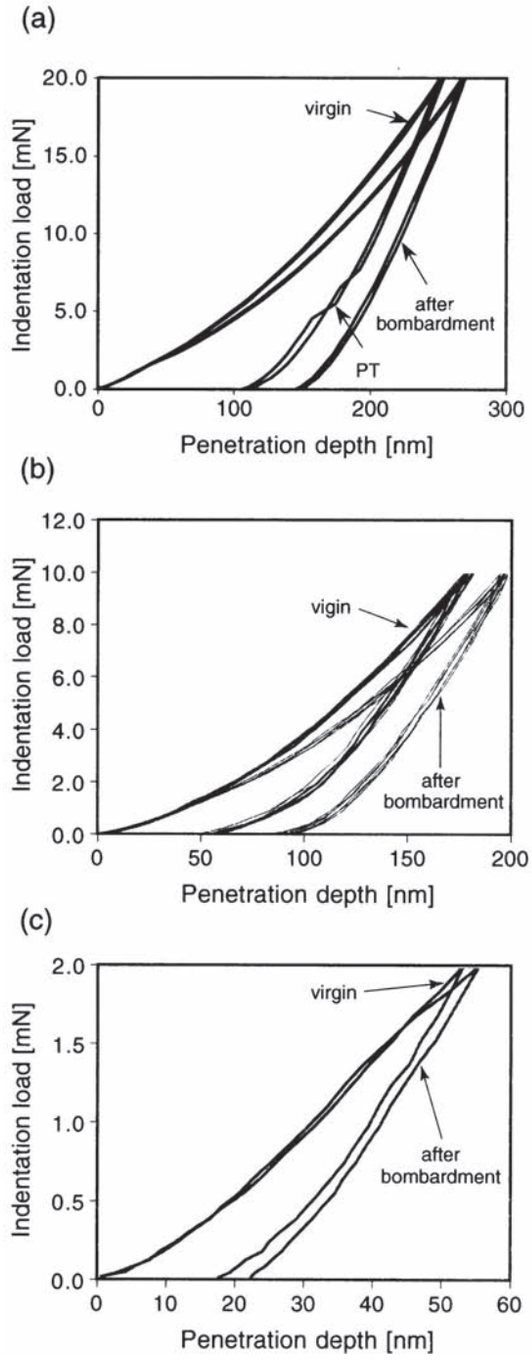

Figure 66. Typical *P–h* curves registered under the maximum indentation load of 20 mN (a) 10 mN (b), and 2 mN (c) for virgin and ion beam–modified HfN thin films deposited on silicon wafer. The point PT (a) denotes pressure-induced phase transformation for silicon. Reprinted with permission from [291], R. Nowak et al., *J. Appl. Phys.* 85, 841 (1999). © 1999, American Institute of Physics.

ion-bombarded films suggests that the crystalline structure of silicon has changed after the applied treatment (Fig. 66(a)). The substrate effect was less pronounced for lower maximum loads (see Fig. 60(b)) and the peculiar result has been obtained by for HfN layers, which deformed identically before and after ion treatment up to a maximum load of 2 mN [292].

The apparent anomaly was clarified [292] by analysis of the nanoindentation data for thinner (200 nm) films (Fig. 66(c)) exhibiting identical loading parts as long as the deformation of the substrate beneath the film does not occur. When the indentation depth exceeds 45 nm, the ion-modified substrate plastic flow starts in, while untreated HfN–silicon system exhibits rigid behavior (Fig. 66(c)).

The coincidence in the hardness of virgin and modified nitrides, observed for low loads, was attributed [292] to the absence of the substrate effect and the fact that the ion bombardment affects merely the distribution of point defects in HfN, while the crystallographic and dislocation structures remained largely unchanged. The above conclusion coincided with the authors' TEM observations, which detected an amorphous layer formed directly below the HfN film (see Fig. 67). The presented study proves that HfN was deformed mainly elastically, while plastic deformation occurred within the substrate (silicon). Consequently, the indenter penetrated deeper in the ion-modified sample with a softer interlayer of amorphous silicon. Hence, the authors [292] demonstrated that the amorphous interlayer could be detected using nanoindentation; even when only the top film is examined.

Identification of an Amorphous Silicon Interlayer by FEM Analysis. The surface deformation of the virgin and Au-bombarded HfN–silicon systems (the conditions of ion treatment are given in Fig. 68) , similar to those described in the previous section, was investigated by computer simulation of the nanoindentation process [94]. The starting point for the computer experiments were nanoindentation measurements for HfN thin films, which exhibited distinct differences between the untreated material and the ion-modified system (Fig. 69(a)).

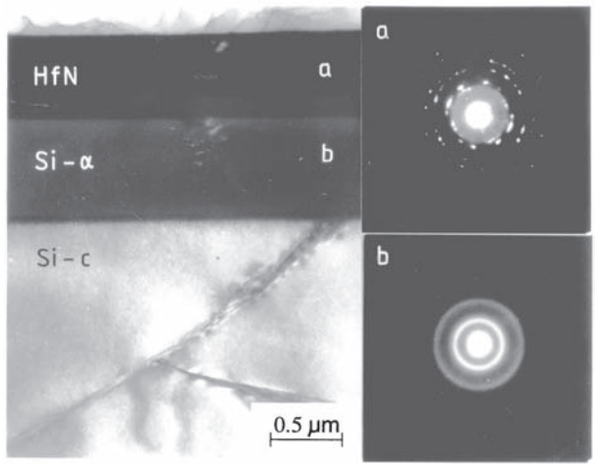

Figure 67. Cross section of the sputter-deposited HfN thin film after bombardment with Si^+ ions (E = 1.1 MeV). The insets show the electron diffraction patterns which confirm the fine polycrystalline nature of nitride film (a) and amorphous structure (Si-α) of the silicon interlayer (b) located between HfN and crystalline silicon wafer (Si-c). Reprinted with permission from [291], R. Nowak et al., *J. Appl. Phys.* 85, 841 (1999). ©1999, American Institute of Physics.

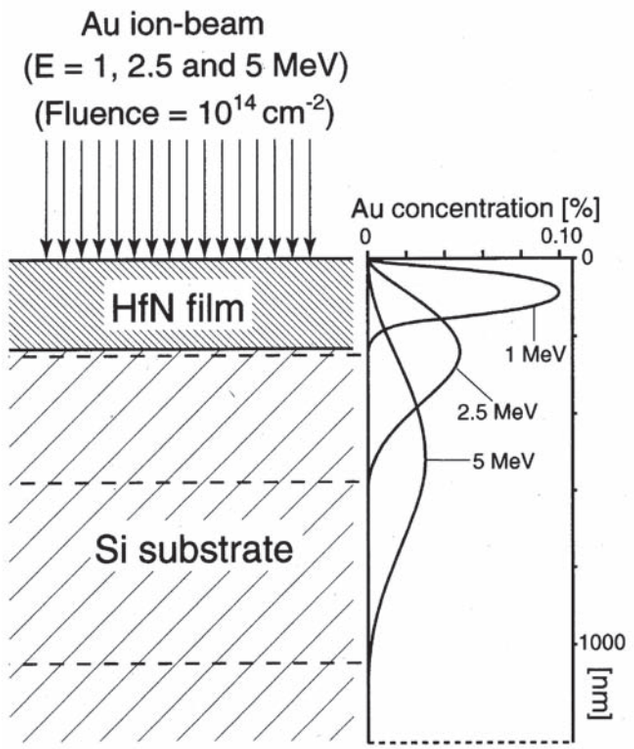

Figure 68. A schematic illustration of modification of HfN–Si system by bombardment with Au ions and the calculated (SASAMAL simulation code) distribution profiles of the implanted species. Reprinted with permission from [94], R. Nowak et al., *Nucl. Instrum. Met, Physics Res.* B148, 110 (1999). © 1999, Elsevier.

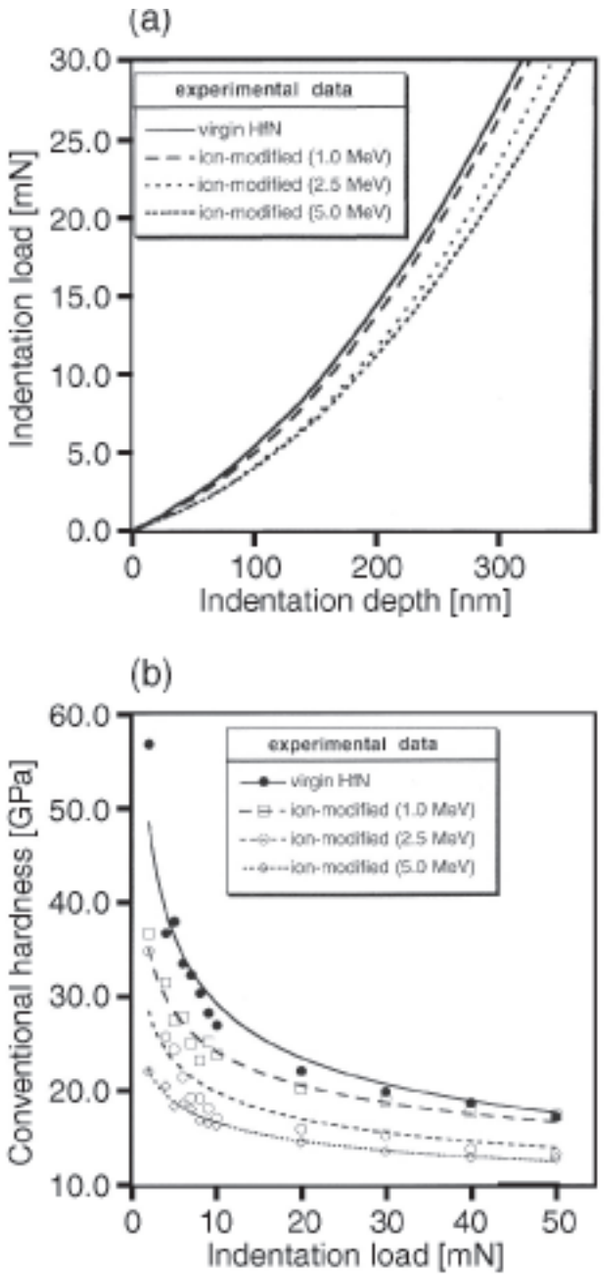

Figure 69. *P–h* curves (loading cycle) registered under P_{max} = 30 mN, for virgin and gold-modified HfN films on silicon (a) and conventional hardness (b) of HfN–Si systems – virgin and modified with Au ions (E = 1, 2.5, and 5 MeV). Reprinted with permission from [94], R. Nowak et al., *Nucl. Instrum. Met. Physics Res.* B148, 110 (1999). © 1999, Elsevier.

To clarify the unexpected softening observed for the HfN–Si system after the ion bombardment (refer to Fig. 69(b)), Nowak et al. [94] assumed that the indentation into hard and thin films deposited on an SS (case of the HfN–silicon system) is affected by the elastic–plastic response of the substrate itself (bases given in [254, 290, 292]). Although the structure of HfN top film appears to be unaffected by ion treatment (see the precedent section), the bombarding species penetrated deep into the silicon substrate [290], and they altered the mechanical properties of the material directly below the nitride layer, which could cause an apparent softening of the film–substrate system (Fig. 69(b)). The cause of the postbombardment decrease in hardness is difficult to be impossible to determine, however, without a theoretical model allowing quantitative estimation of the substrate's influence on the surface deformation of the film.

Therefore, the authors [94] performed the numerical simulation of the indentation of a sharp indenter into the HF located on the SS with the interlayer (IS – the modified substrate with different mechanical properties) using FEM simulation (see Fig. 70). It was assumed that the top layer (HF) deforms exclusively elastically, since ion-bombarded nitrides possess an original structure of stoichiometric HfN [289–290], while sputter-deposited HfN films exhibit ultrahigh hardness and yield strength [250, 296]. The SS and IS regions exhibit elastic–perfectly plastic behavior with a yield condition governed by the von Mises criterion. Moreover, for a specific part of the SS region (where the hydrostatic stress component exceeds 11.5 GPa), the volumetric change associated with pressure-induced phase transformation of silicon crystal [63] was modeled. The authors carried out several trial simulations by altering the mechanical characteristics of the IS interlayer, while the values of the parameters for the HF and SS areas were maintained constant.

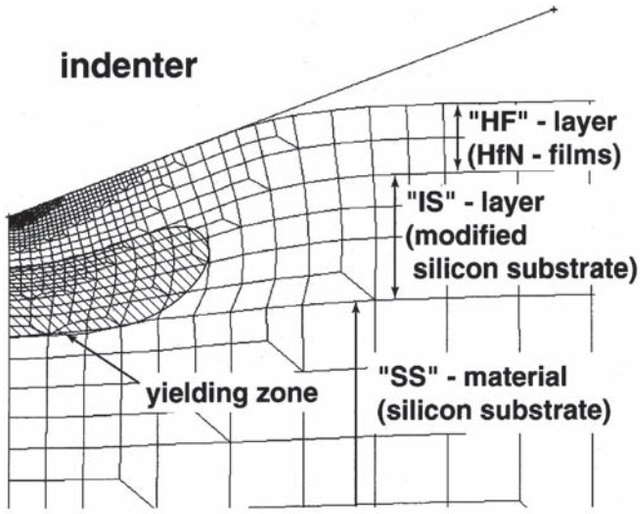

Figure 70. Finite element mesh used to simulate indentation in HfN–Si system implanted with highly Au ions. The Berkovich tip was approximated by a cone indenter which allowed us to treat the problem in two dimensions. Reprinted with permission from [94], R. Nowak et al., *Nucl. Instrum. Met. Physics Res.* B148, 110 (1999). © 1999, Elsevier.

The triangular indenter was modeled by a cone to reduce the computation time.

Nowak et al. [94] achieved an agreement between the simulated results (see Fig. 71) and their experimental data (see Fig. 69) for Young's modulus and yield strength of IS layer equal 135 and 4.5 GPa, respectively. These values appeared to be accurate for amorphous silicon. A similar approach was explored by Myers et al. [280], who discussed the hardness changes for ion-implanted nickel in terms of FEM modeling.

The works of this kind are being nowadays in a canter of interest and address the structures with increasing complexity. The numerical investigation of indentation into highly inhomogenous powder compacts by Kumar et al. [297], who modeled densification of the material as well as FEM analysis of spherical indentation in alumina-based trilayers composites accomplished by Ha et al. [298], serves as interesting examples of the actual trends. However, the recent nanodeformation experiments require basic mechanical data that sometimes cannot be achieved by conventional methods. The example is the determination of HfN, TiN, and ZrN elastic constants using *ab initio* calculations by Nagao et al. [299].

5. SUMMARIZING REMARKS

The present review started with a criticism of the definition of hardness and the introduction of the concept of depth-sensing indentation experiments. Subsequently, it addressed the issue of the available theoretical approaches to nanoindentation data, and how they allow one to determine Young's modulus and conventional hardness of tested

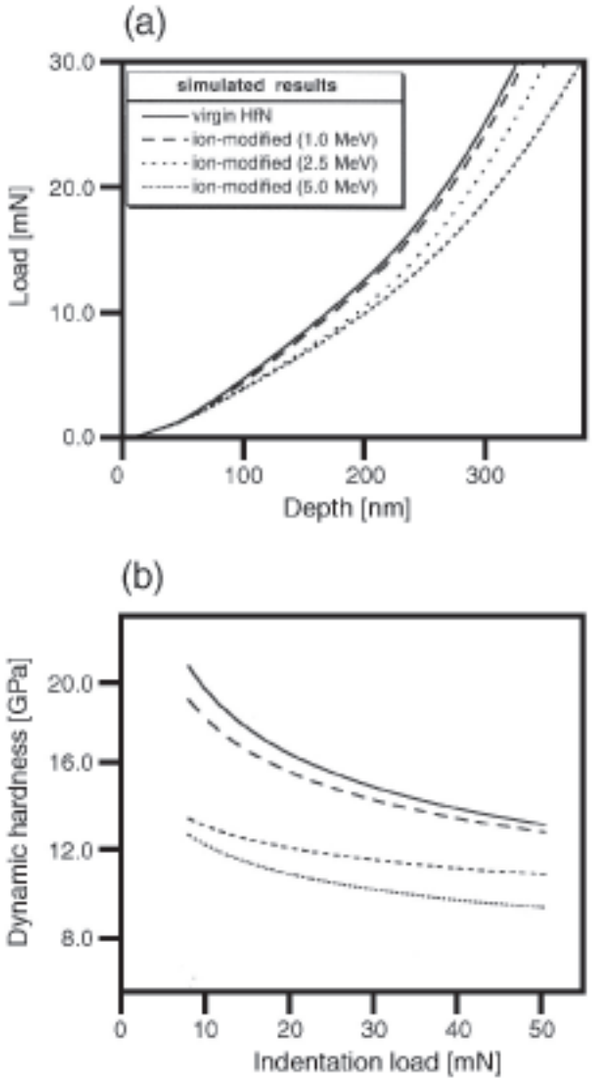

Figure 71. Simulation-predicted *P–h* curves (a) and hardness variation (b) calculated for the virgin and ion-modified HfN–Si systems. Reprinted with permission from [94], R. Nowak et al., *Nucl. Instrum. Met. Physics Res.* B148, 110 (1999). © 1999, Elsevier.

materials (Sections 2.1 and.2). Attention has been given to the experiments with both sharp and spherical tips, as well as to such phenomena as pileup and sinking-in, which remain dilemmas for indentation measurements. Further, the numerical simulation of the indentation process using the FEM method received appropriate consideration since they enable us to make conclusions about the shape and size of the contact area, the pertinent parameter that is not available for experiments.

Nanoindentation characterization of ceramic materials, including new semiconductors and superconductors, was reviewed in Section 3, based in a large part on research by the present author. The first part of the chapter elaborates two essentially different approaches based on the analysis of the indentation energy consumed during the penetration

process, namely, by Rother et al. [185] and the EPI method [133]. The latter appears to be followed by a number of examples that point out the effectiveness of the theory for characterizing a range of new and advanced materials as well as multilayer structures.

Hence, this review presents an alternative to the more or less accepted routine procedures concerning nanoindentation results. The only exemption was the nanoindentation of bulk GaN [196], which represents enough unique material itself to be treated by standard methods. In due course, the anisotropic surface deformation of crystals was elaborated with the emphasis on the new models for sharp and spherical contact [77, 99, 193, 205, 206], which helped in the explanation of the anomalies and novel phenomena observed during the nanoindentation of sapphire. These approaches are completed by the recent MD simulation [22, 171] and quantum considerations [299].

The closing section is devoted to the nanoindentation of ion beam–modified solids and thin films – the subject being nowadays of great importance for electronics, MEMS, nanostructures, and smart materials (see, e.g. [242]). In this case, the advantages of using the FEM simulation of surface deformation was demonstrated by the example in which the presence of the amorphous silicon interlayer was deduced from the indentation data, although the discussed region was beyond direct experimental access. Moreover, the mechanical characteristics of this part of material (interlayer) modified by ion bombardment were evaluated based on FEM calculations, which together with similar studies by Myers et al. [280], Kumar et al. [297], and Ha et al. [298], represent the most promising result.

This review has deliberately disregarded the analysis of the force–distance (P–h) curves obtained by means of an atomic force microscope, since Capella and Dieter [300] offered thorough review of this particular subject in 1999. It completes and frequently contrasts the other available summaries of nanoindentation research (e.g. [301, 302]) that routinely base on mechanical analysis, while our work emphasizes a combination of the approaches that stem from nanomechanics and solid-state physics (atomistic considerations).

ACKNOWLEDGMENTS

The authors thank Dr. T. Wyrobek (Hysitron Inc., Minneapolis), Profs. R. Tenne & H. Wagner, Drs. S. Cohen & Y. Rousso (Weizmann Inst. Science, Rehovot), Prof. G. Kostorz (ETH, Zürich), Prof. J. Pospiech (Polish Academy of Sciences), Prof. M. Sakai (Toyohashi University of Technology), Prof. M. V. Swain (University of Otago), Prof. I. Yonenaga (Tohoku University), Prof. W. Sakamoto & Prof. S.-I. Hirano (Nagoya University) for the invaluable discussions. Drs. Chunliag Li & M. Fujikane, Profs. T. Sekino & K. Niihara (Osaka University) as well as Dr. S. Nagao (Nordic Hysitron Laboratory) all are acknowledged for stimulating ideas expressed during co-operative nanoindentation research with R.N. The long-standing collaboration with Profs. M. Pessa (Tampere University of Technology), K. Nordlund, J. Räisänen and J. Keinonen (Helsinki University) as well as the support by the Academy of Finland through sponsoring the consortia NAKAMA-EXT, NANOTOMO, and CIBNANO – coordinated or participated by the Nordic Hysitron Laboratory – are also gratefully acknowledged.

CONVENTIONS AND NOTATIONS

a	contact radius
a_r	radius of the residual contact impression
A	projected contact area
A_c	actual contact area
A_p	projected area of the indentation mark
B, m	fitting parameters in Oliver–Pharr analysis
d, d_1	size of the residual impression
d_c	distance of the contact cross section from the indenter tip
D	diameter of spherical indenter
E	Young's modulus
E_1	elastic modulus of the indented solid
E_2	elastic modulus of the indenter
E_{eff}	effective elastic modulus
$\tilde{E}_1, \tilde{E}_2, \tilde{E}_3$	specific energies for densification, shear displacement, and interface formation
$\boldsymbol{F}$	force exerted on the material by indenter facet
$\boldsymbol{g}$	slip direction
$\boldsymbol{G}$	the vector which defines the projection of the indenter axis onto its facet
H_0	initial indentation depth
h_1	elastic displacement above the contact line
h_2	elastic displacement below the contact line
h_c	contact depth
h_E	total elastic displacement under the spherical tip ($h_E^{max} = h_t - h_r$)
h_e	elastically recovered indentation depth
h_f	residual indentation depth after complete unloading
h_p	plastic depth of indentation
h_r	residual indentation depth
h_t, h_{max}	maximum indentation depth ($h_t = h_{max}$)
$\tilde{h}_1, \tilde{h}_2, \tilde{h}_3$	the depth components associated with densification, shear, and interface formation
H	conventional hardness
H_T	true hardness
$\tilde{H}$	hardness based on calculated probability of activation slip and twinning systems
H/E	hardness to Young's modulus ratio
J_2	second invariant of the stress deviator
k_i	shape factors for particular indenter geometry
K_{IC}	fracture toughness
n	work hardening exponent; Norton creep-law exponent
$\boldsymbol{n}$	unit normal vector of the slip plane
N	number of cracked grain boundaries
$\boldsymbol{N}_j$	inward vector, normal to the contact
p_o	far-field hydrostatic compression
$p = p_{av}$	mean contact pressure

P current indentation load
P_{max} maximum indentation load
R radius of the spherical indenter
S stiffness $S = dP/dh$
S_u unloading slope
$T_i(\mu)$ probability of activating ith slip–twinnig system for orientation μ
u_1, u_2, u_3 mean energy densities expended for densification, shear, and interface formation
u_{2max} maximum positive surface displacement
U_F friction energy
U_r energy expended for the irreversible surface deformation
U_T total deformation energy
U_1, U_2, U_3 deformation energies expended for densification, shear displacement, and interface formation
V volume of indenter tip under the contact perimeter ($V = (1/3).\alpha_0.a^3.\cot\psi$)
$\alpha_\circ$ geometrical factor denoting shape of the indenter
$\alpha = \psi_{max}$ the angle between force F and axis of ball indenter for maximum loading
β indenter shape coefficient in Oliver–Pharr analysis
γ geometrical factor denoting surface deflection
γ_e geometrical factor denoting surface deflection for perfectly elastic contact
γ_o geometrical factor denoting surface deflection for perfectly plastic contact
γ_H geometrical factor denoting surface deflection for elasto-plastic contact
Γ_I work of indentation
δ depth of an elastic penetration of a spherical indenter
δ the angle between the slip direction $\boldsymbol{g}$ and vector $-\boldsymbol{G}$
δ_{ij} Kronecker tensor
ε^c stress-dependent creep rate
ε_{kl} strain tensor
ε_p engineering nominal strain $\varepsilon_p = \varepsilon_{kl} - \sigma/E$
ζ surface displacement factor
η, ξ geometrical factor denoting shape of the indenter in Chandler–Page analysis
κ the angle between the slip direction $\boldsymbol{g}$ and the axis of rotation of slip system
λ the angle between force $\boldsymbol{F}$ and and the vecor $\boldsymbol{n}$ denoting slip plane
Λ_i shear stress correction factor for particular surface orientation
ϕ the angle between the slip direction $\boldsymbol{g}$ and force $\boldsymbol{F}$
μ orientation of the indenter
$(\mu, \in\psi)$ angular coordinates of the grid on s spherical indenter
ν_1 Poisson's ratio of the tested solid
ν_2 Poisson's ratio of the indenter
χ the angle between force $\boldsymbol{F}$ and and the axis of rotation of slip system
ρ friction coefficient
σ_{ij} stress tensor
σ'_{ij} deviatoric tensor $\sigma'_{ij}\sigma = \sigma_{ij} - \sigma_{kk}\delta_{ij}/3$
σ_e effective Mises stress $\sigma_e = (3/2)\sigma_{ij}\sigma'_{ij}$
σ_u ultimate stress
σ_Y yield stress
τ_{eff} the effective resolved shear stress
τ_i shear stress in the ith slip system
τ_{CRi} critical shear stress in the ith slip system
ψ semiapex angle of cone indenter
ω the angle between the intersection of the $(\boldsymbol{n}, \boldsymbol{g})$ plane and the indenter facet, and the vector $-\boldsymbol{G}$

REFERENCES

1. K. Hiraoka, *Thin Solid Films* 235, 182–194 (1993).
2. I. J. McColm, "Ceramic Hardness," New York: Plenum, 1990.
3. J. H. Westbrook and H. Conrad (Eds.), "The Science of Hardness Testing and its Research Applications," Metals Park, OH: American Society for Metals, 1973.
4. D. Tabor, *Proc. R. Soc. Lond. Ser. A* 192, 247–253 (1948).
5. D. Tabor, "The Hardness of Metals," Oxford: Clarendon Press, 1951.
6. R. Hill, B. Storåkers, and A. B. Zdunek, *Proc. R. Soc. Lond.* A423, 301–330 (1989).
7. B. Storåkers and P. L. Larsson, *J. Mech. Phys. Solids* 42, 307–332 (1994).
8. R. Nowak, K. Ueno, and M. Kinoshita, in "Fracture Mechanics of Ceramics" (R. C. Bradt et al., Eds.), Vol. 10, pp. 155–174, New York and London: Plenum Press, 1992.
9. R. W. Armstrong and W. H. Robinson, *N. Z. J. Sci.* 17, 429–437 (1974).
10. W. J. Cousins, R. W. Armstrong, and W. H. Robinson, *J. Mater. Sci.* 10, 1655–1661 (1985).
11. D. Newey, M. A. Wilkins, and H. M. Pollock, *J. Phys. E: Sci. Instrum.* 15, 1655–1664 (1982).
12. J. B. Pethica, R. Hutchings, and W. C. Oliver, *Philos. Mag.* A48, 593–606 (1983).
13. P. E. Wierenga and A. J. Franken, *J. Appl. Phys.* 55, 4244–4247 (1984).
14. R. F. Cook and G. M. Pharr, *J. Am. Ceram. Soc.* 73, 787–807 (1990).
15. R. Tandon, D. J. Green, and R. F. Cook, *J. Am. Ceram. Soc.* 73, 2619–2627 (1990).
16. W. R. LaFontaine, C. A. Paszkiet, M. A. Korhonen, and Y. Li, *J. Mater. Res.* 6, 2084–2092 (1991).
17. D. Stone, W. LaFontaine, P. Alexopoulos, T. Wu, and Y. Li, *J. Mater. Res.* 3, 141–152 (1988).
18. B. N. Lucas, W. C. Oliver, R. Williams, J. Brynestad, and M. E. O'Hern, *J. Mater. Res.* 6, 2084–2092 (1991).
19. R. Clarke, M. C. Kroll, P. D. Kirchner, R. F. Cook, and B. J. Hockey, *Phys. Rev. Lett.* 21, 2156–2158 (1988).
20. S. Ruffell, J. E. Bradby, and J. S. Williams, *Appl. Phys. Lett.* 89, 091919 (2006).
21. S. Ruffell, J. E. Bradby, N. Fujisawa, and J. S. Williams, *J. Appl. Phys.* 101, 083531, (2007).
22. D. Chrobak, K. Nordlund, and R. Nowak. *Phys. Rev. Lett.* 98, 045502, (2007).
23. R. Nowak, D. Chrobak, S. Nagao, D. Vodnick, M. Berg, A. Tukiainen, and M. Pessa [in press]. AQ2
24. T. F. Page, W. C. Oliver, and C. J. McHargue, *J. Mater. Res.* 7, 450–475 (1992).
25. S. J. Lloyd, J. M. Molina-Aldereguia, and W. J. Clegg, *Philos. Mag. A* 82, 1963–1969 (2002).
26. S. Basu, M. W. Barsoum, and S. R. Kalidindi, *J. Appl. Phys.* 99, 063501 (2006).
27. F. Giuliani, S. J. Lloyd, L. J. Vandeperre, and W. J. Clegg, in:"Proc. Electr. Micros. Anal." (S. McVitie and D. McComb. Eds.), Vol. 179, pp. 123–126, Oxford:, Institute of Physics, 2003.
28. T. Wermelinger, C. Borgia, C. Solenthaler, and R. Spolenak, *Acta Mater.* 55, 4657–4666 (2007).

29. M. E. O'Hern, C. J. McHargue, C. White, and G. Farlow, *Nucl. Instrum. Meth.* B46, 171–175 (1990).
30. W. Ensinger and R. Nowak, *Nucl. Instrum. Met. Physics Res.* B80/81, 1085–1090 (1993).
31. W. Ensinger, R. Nowak, Y. Horino, and K. Baba, *Ceram. Forum Int.* 70, 164–167 (1993).
32. R. Nowak, Y. Horino, W. Ensinger, K. Ueno, M. Kinoshita, and M. Satou, in "Euroceramics II," Vol. 2, pp. 1055–1059, 1992.
33. M. F. Doerner and W. D. Nix, *J. Mater. Res.* 1, 601–612 (1986).
34. G. M. Pharr, W. C. Oliver, and F. R. Brotzen, *J. Mater. Res.* 7, 613–617 (1992).
35. C. W. Shih, M. Yang, and J. C. M. Li, *J. Mater. Res.* 6, 2623–2630 (1992).
36. W. C. Oliver and G. M. Pharr, *J. Mater. Res.* 7, 1564–1571 (1992).
37. D. Tranchida and S. Piccarolo, *Macromol. Rapid Commun.* 26, 1800–1804 (2005).
AQ3
38. R. Nowak, M. Fujikane, S. Kucharski, and T. Wyrobek [in press].
39. A. K. Bhattacharya and W. D. Nix, *Int. J. Solids Struct.* 24, 881–891 (1988).
40. T. A. Lursen and J. C. Simo, *J. Mater. Res.* **7**, 618–627 (1992).
41. H. Hertz, *J. Reine Angew. Math.* 92, 156–171 (1882); H. R. Hertz, "Miscellaneous Papers," London: Macmillan, 1986, Chaps. 5 and 6.
42. K. L. Johnson, "Contact Mechanics," Cambridge, Cambridge University Press, 1985.
43. The parameters refer to the tester – Hysitron TriboIndenter (http://www.hysitron.com)
44. M. Sakai and R. Nowak, in "Ceramics Adding the Value, AUSTCERAM 92" (M. J. Bannister, Ed.), pp. 922–931, Sydney: CSIRO Publications, 1992.
45. M. Sakai, *Acta Metall. Mater.* 41, 1751–1759 (1993).
46. R. Nowak and M. Sakai, *J. Mater. Res.* 8, 1068–1078 (1993).
47. G. M. Pharr, in "Modification of Ceramics and Semiconductors by Ion Bombardment" (R. Nowak et al., Eds.) (1998; special issue, *Mater. Sci. Eng.* A253, 151–159 (1998)).
48. M. V. Swain, in "Modification of Ceramics and Semiconductors by Ion Bombardment" (R. Nowak et al., Eds.) (1998; special issue, *Mater. Sci. Eng.* A253, 160–166 (1998)).
49. J. R. Turner, *Int. J. Solids Struct.* 16, 409–419 (1980).
50. V. I. Fabrikant, *Trans. ASME* 53, 798–806 (1986).
51. H. Fan and L.M. Keer, *Trans. ASME* 61, 250–255 (1994).
52. J. Boussinesq, "Applications des Potentiels á l'Étude de Équilibre et du Mouvement des Solides Élastiques," Paris: Gauthier-Villars, 1885.
53. J. G. Simmonds and P. G. Warne, *J. Elast.* 34, 69–82 (1994).
54. I. N. Sneddon, *Int. J. Eng. Sci.* 3, 47–57 (1965).
55. S. L. Bulychev, V. Alekhin, M. K. Shorshorov, A. P. Ternovski. and G. D. Shmyrev, *Int. Lab.* 41, 1409–1412 (1975).
56. R. B. King, *Int. J. Solids Struct.* 23, 1657–1664 (1987).
57. J. L. Loubet, J. M. Georges, O. Marchesini, G. Meille, and W. C. Oliver, *J. Tribol.* 106, 43–48 (1984).
58. D. Tranchida and S. Piccarolo, *Polymer* 46, 4032–4040 (2005).
59. T. J. Bell, A. Bendelli, J. S. Field, M. V. Swain, and E. G. Twaite, *Metrologia* 28, 463–469 (1992).
60. J. S. Field and M. V. Swain, *J. Mater. Res.* 8, 297–306 (1993).
61. J. S. Field and M. V. Swain, *J. Mater. Res.* 10, 101–112 (1995).
62. E. R. Weppelmann, J. S. Field, and M. V. Swain, *J. Mater. Res.* 8, 830–840 (1993).
63. E. R. Weppelmann, J. S. Field, and M. V. Swain, *J. Mater. Sci.* 30, 2455–2462 (1995).
64. T. J. Bell, J. S. Field, and M. V. Swain, in "Mater. Res. Soc. Symp.," Vol. 238, pp. 331–336, 1992.
65. M. Shiwa, E. R. Weppelmann, A. Bendeli, M. V. Swain, D. Munz, and T. Kishi, *Surf. Coat. Technol.* 68–69, 598–602 (1994).
66. E. R. Weppelmann and M. V. Swain, *Thin Solid Films* 286, 111–121 (1996).
67. A. C. Fischer-Cripps, "Introduction to Contact Mechanics," New York: Springer Science+Business Media, 2007.
68. W. W. Gerberich, W. Yu, D. E. Kramer, A. Strojny, D. F. Bahr, E. T. Lilleodden, and J. Nelson, *J. Mater. Res.* 13, 421–439 (1998).
69. E. Söderlund and N.H. Macmillan, *J. Mater. Sci. Lett.* 10, 720–722 (1991).
70. E. Söderlund and D. J. Rowcliffe, *J. Hard Mater.* 5, 149–177 (1994).
71. P. L. Larsson, A. Giannakopoulos, E. Söderlund, D. J. Rowcliffe, and R. Vestergaard, *Int. J. Solids Struct.* 33, 221–248 (1996).
72. K. Zeng, E. Söderlund, A. Giannakopoulos, and D. J. Rowcliffe, *Acta Mater.* 44, 1127–1141 (1996).
73. S. V. Hainsworth, H. W. Chandler, and T. F. Page, *J. Mater. Res.* 8, 1987–1995 (1996).
74. M. R. Begley and J. W. Hutchinson, *J. Mech. Phys. Solids* 46, 2046–68 (1998).
75. J. L. Loubet, J. M. Georges, and G. Meille, in "Microindentation Techniques in Materials Science and Engineering" (P. J. Blau and B. R. Lawn, Eds.), pp. 72–89, Philadelphia: American Society for Testing and Materials, 1986.
76. B. Taljat, T. Zacharia, and F. M. Haggag, *J. Mater. Res.* 4, 965–974 (1997).
77. R. Nowak, T. Manninen, K. Heiskanen, T. Sekino, A. Hikasa, K. Niihara, and T. Takagi, *Appl. Phys. Lett.* 83, 5214–5216 (2003).
78. S. Kucharski and Z. Mroz, *Trans. ASME, J. Eng. Mater. Technol.* 123, 245 (2001); *Mater. Sci. Eng. A* 318, 65–76 (2001); *Mater. Sci. Eng. A* 379, 448 (2004).
79. W. C. Oliver, R. Hutchings, and J. B. Pethica, in "ASTM STP" (P. J. Blau and B. R. Lawn, Eds.), pp. 90–108, Philadelphia: Amer. Soc. Test. Mater., 1986.
80. J. B. Pethica and W. C. Oliver, *Phys. Scr.* T19, 61–66 (1987).
81. C. W. Shih, M. Yang, and J. C.M. Li, *J. Mater. Res.* 6, 2623–2628 (1991).
82. H. Bei, E. P. George, J. L. Hay, and G. M. Pharr, *Phys. Rev. Lett.* 95, 45501–045505 (2005).
83. A. Bolshakov and G. M. Pharr, *J. Mater. Res.* 13, 1049–1058 (1998).
84. C. Hardy, C. N. Baronet, and G. V. Tordion, *Int. J. Num. Mech. Engng.* 3, 451–467 (1971).
85. C. H. Lee, S. Masaki, and S. Kobayashi, *Int. J. Mech. Sci.* 14, 417–426 (1972).
86. P. S. Follansbee and G. B. Sinclair, *Int. J. Solids Struct*. 20, 81–91 (1984). G. B. Sinclair, P. S. Follansbee, and K. L. Johnson, *Int. J. Solids Struct*. 21, 865–888 (1985).
87. R. Hill and B. Storåkers, in "Elasticity: Mechanical Methods and Applications" (G. Eason and R. W. Ogden, Eds.), pp. 199–210, Chichester: Ellis Horwood, 1990.
88. S. Biwa and B. Storåkers, Report 168, Analysis of Fully Plastic Brinell Indentation, Department of Solid Mechanics, The Royal Institute of Technology, Stockholm, 1994.
89. T. O. Mulhearn and D. Tabor, *J. Inst. Metals* 89, 7–12 (1960).
90. F. H. Norton, "Creep of Steel in High Temperatures," New York: McGraw-Hill, 1929.
91. Mc. Shaw and G. J. DeSalvo, *Trans. ASME J. Eng. Indust.* 92, 480–494 (1970); *Trans. ASME J. Eng. Indust.* 469–479.
92. A. K. Bhattacharya and W. D. Nix, *Int. J. Solids Struct.* 24, 1287–1298 (1988).
93. J. C. Simo, *Comput. Met. Appl. Mech. Engin.* 68, 1–31 (1988).
94. R. Nowak, C. L. Li, T. Okada, and F. Yoshida, *Nucl. Instrum. Met. Physics Res.* B148, 110–115 (1999).
95. H. Wang and H. Bangert, *Mater. Sci. Eng.* A163, 43–50 (1993).
96. A. Giannakopoulos, P. L. Larsson, and R. Vestergaard, *Int. J. Sol. Struct*. 5, 149–177 (1994).
97. G. M. Pharr and R. F. Cook, *J. Mater. Res.* 15, 847–851 (1990).
98. W. Zielinski, H. Huang, and W. W. Gerberich, *J. Mater. Res.* 8, 1300–1310 (1993).
99. R. Nowak, T. Sekino, and K. Niihara, *Philos. Mag.* A74, 171–195 (1996).
100. K. Zeng, A. E. Giannakopoulos, and D. J. Rowcliffe, *Acta Metall. Mater.* 43, 1945–1954 (1995).

101. K. Zeng and D. J. Rowcliffe, *Acta Metall. Mater.* 43, 1935–1943 (1995).
102. J. Salomonson, K. Zeng, and D. J. Rowcliffe, *Acta Mater.* 44, 543–546 (1996).
103 K. Zeng and D. J. Rowcliffe, *Philos. Mag.* 74, 1107–1116 (1996).
104. A. Giannakopoulos and P. L. Larsson, *Mech. Mater.* 25, 1–35 (1997).
105. D. C. Drucker and W. Prager, *Q. Appl. Math.* 10, 157–165 (1952).
106. J. Mackerle, *Eng. Comput.: Int. J. Comp.-Aided Eng.* 21, 23–52 (2004).
107. J. Mackerle, *Finite Elements Anal. Des.* 37, 811–819 (2001).
108. J. Mackerle, "Finite Element Methods, A Guide to Information Sources," Amsterdam: Elsevier, 1991.
109. Y.-T. Cheng and C.-M. Cheng, *J. Mater. Res.* 13, 1059–1064 (1998).
110. T. Sawa, Y. Akiyama, A. Shimamoto, and K. Tanaka, *J. Mater. Res.* 14, 2228–2232 (1999).
110. A. C. Fischer-Cripps and B. R. Lawn, *J. Am. Ceram. Soc.* 79, 2609–2618 (1996).
112. A. Shimamoto, K. Tanaka, Y. Akiyama, and H. Yoshizaki, *Philos. Mag.* 74, 1097–1105 (1996).
113. J. C. Hay, A. Bolshakov, and G. M. Pharr, *J. Mater. Res.* 14, 2296–2305 (1999).
114. M. C. Fivel, C. F. Robertson, G. R. Canova, and L. Boulanger, *Acta Mater.* 46, 6183–6194 (1998).
115. C. F. Robertson and M. C. Fivel, *J. Mater. Res.* 14, 2251–2258 (1999).
116. E. B. Tadmor, R. Miller, and R. Phillips, *J. Mater. Res.* 14, 2233–2250 (1999).
117. A. E. Giannakopoulos and S. Suresh, *Acta Mater.* 46, 2153–2164 (1999); *Int. J. Solids Struct.* 34, 2357–2369 (1997); *Int. J. Solids Struct.* 34, 2393–2411 (1997).
118. S. Suresh, A. E. Giannakopoulos, and J. Alcala, *Acta Mater.* 45, 130713–130721 (1997).
119. S. Suresh and A. E. Giannakopoulos, *Acta Mater.* 46, 5755–5767 (1998).
120. T. Nakamura, *Acta Mater.* 48, 4293–4306 (2000).
121. T. F. Page, G. M. Pharr, J. C. Hay, W. C. Oliver, B. N. Lucas, E. Herbert, and L. Riester, in "Fundamentals of Nanoindentation and Nanotribolog" (S. P. Baker et al., Eds.), Vol. 522, pp. 47–59, Proc. Symp. Mater. Res. Soc., 1998.
122. M. R. McGurk and T. F. Page, *J. Mater. Res.* 14, 2283–2295 (1999).
123. S. V. Hainsworth, M. R. McGurk and T. F. Page, *Surf. Coat. Technol.* 102, 97–107 (1998).
124 S. K. Venkataraman, D. L. Kohlstedt, and W. W. Gerberich, *J. Mater. Res.* 8, 685–696 (1993).
125. W. W. Gerberich, S. K. Venkataraman, H. Huang, S. E. Harvey, and D. L. Kohlstedt, *Acta Metall. Mater.* 43, 1569–1576 (1995).
126. W. Zielinski, H. Huang, S. Venkataraman, and W. W. Gerberich, *Philos. Mag.* 72, 1221–1237 (1995).
127. M. P. de Boer and W. W. Gerberich, *Acta Mater.* 44, 3169–3175 (1996); *Acta Mater.* 44, 3177–3187 (1996)
128. W. W. Gerberich, J. C. Nelson, E. T. Lilleodden, P. Anderson, and J. T. Wyrobek, *Acta Mater.* 44, 3585–3598 (1996).
129. S. G. Corcoran, R. J. Colton, E. T. Lilleodden, and W. W. Gerberich, *Phys. Rev. B* 55, R16057–R16060 (1997).
130. D. F. Bahr, D. E. Kramer, and W. W. Gerberich, *Acta Mater.* 46, 3605–3617 (1998).
131. D. F. Bahr and W. W. Gerberich, *J. Mater. Res.* 13, 1065–1074 (1998).
132. R. Nowak, T. Sekino, and K. Niihara, *Acta Mater.* 47, 4329–4338 (1999).
133. N. I. Tymiak, D. E. Kramer, D. F. Bahr, T. J. Wyrobek, and W. W. Gerberich, *Acta Mater.* 49, 1021–1034 (2001).
134. C. A. Schuh, *Mater. Today* 9, 32–40 (2006).
135. A. M. Minor, S. A. Syed Asif, Z. Shan, E. A. Stach, E. Cyrankowski, T. Wyrobek, and O. L. Warren, *Nature Mater.* 5, 697–702 (2006).
136. Hysitron Nano-ECR (http://www.hysitron.com).
137. U. Landman, W. D. Luedtke, N. A. Burnham, and R. J. Colton, *Science* 248, 454–459 (1990).
138. D. Christopher, R. Smith, and A. Richter, *Nanotechnology* 12, 372 (2001).
139. J. M. Thijsen, "Computational Physics," Cambridge University Press, 2003.
140. L. Verlet, *Phys. Rev.* 159, 98–106 (1967).
141. H. J. C. Berendsen, J. P. M. Postma, W. F. Van Gunsteren, A. DiNola, and J. R. Haak, *J. Chem. Phys.* 81, 3684–3690 (1984).
142. S. Melchionna, G. Ciccotti, and B. L. Holian, *Mol. Phys.* 78, 533–544 (1993).
143. F. Stillinger and T. A. Weber, *Phys. Rev. B* 31, 5262 (1985).
144. J. Tersoff, *Phys. Rev. B* 37, 6991 (1988).
145. D. W. Brenner, *Phys. Rev. B* 42, 9458 (1990).
146. M. Finnis and J. Sinclair, *Philos. Mag. A* 50, 45–55 (1984).
147. S. Foiles, M. Baskes, and M. Daw, *Phys. Rev. B* 33, 7983–7991 (1986).
148. I. Szlufarska, *Mater. Today* 9, 42–50 (2006).
149. P. Walsh, A. Omeltchenko, R. K. Kalia, A. Nakano, and P. Vashishta, *Appl. Phys. Lett.* 82, 118–120 (2003).
150. J. Li, K. J. Van Vliet, T. Zhu, S. Yip, and S. Suresh, *Nature* 418, 307–310 (2002).
151. S. G. Corcoran, R. J. Colton, E. T. Lilleodden, and W. W. Gerberich, *Phys. Rev. B* 55, R16057–R16060 (1997).
152. A. Guldstone, K. J. Van Vliet, and S. Suresh, *Nature* 411, 656–657 (2001).
153. S. Suresh, *Science* 292, 2447–2451 (2001).
154. J. Li, K. J. Van Vliet, T. Zhu, S. Yip, and S. Suresh, *Nature* 418, 307–310 (2002).
155. C. A. Schuh, J. K. Mason, and A. C. Lund, *Nature Mater.* 4, 617–621 (2005).
156. I. Szlufarska, A. Nakano, and P. A. Vashista, *Science* 309, 911–914 (2005).
157. W. Gerberich and W. Mook, *Nature Mater.* 4, 577–578 (2005).
158. S. Suresh, *Nature Mater.* 5, 253–254 (2006).
159. G. L. W. Cross, A. Schirmeisen, P. Grütter, and U. T. Dürig, *Nature Mater.* 5, 370–376 (2006).
160. P. Schall, I. Cohen, D. A. Weitz, and F. Spaepen, *Nature* 440, 319–323 (2006).
161. C. L. Kelchner, S. J. Plimpton, and J. C. Hamilton, *Phys. Rev. B* 58, 11085 (1998).
162. J. D. Kiely, R. Q. Hwang, and J. E. Houston, *Phys. Rev. Lett.* 81, 4424 (1998).
163. J. A. Zimmerman, C. L. Kelchner, P. A. Klein, J. C. Hamilton, and S. M. Foiles, *Phys. Rev. Lett.* 87, 165507 (2001).
164. I. Szlufarska, R. K. Kalia, A. Nakano, and P. Vashista, *Phys. Rev. B* 71, 174113 (2005).
165. K. J. Van Vliet, J. Li, T. Zhu, S. Yip, and S. Suresh, *Phys. Rev. B* 67, 104105 (2003).
166. Y. Choi, K. J. Van Vliet, J. Li, and S. Suresh, *J. Appl. Phys.* 94, 6050 (2003).
167. H. S. Leipner, D. Lorenz, A. Zeckzer, H. Lei, and P. Grau, *Physica B* 308–310, 446–449 (2001).
168. E. LeBourhis and E. Patriarche, *Micron* 38, 377–389 (2007).
169. J. E. Brandby, J. S Williams, J. Wong-Leung, M. V Swain, and P. Munroe, *Appl. Phys. Lett.* 78, 3235–3237 (2001).
170. E. Le Bourhis and E. Patriarche, *Phys. Status Solidi C* 4, 3002–3009 (2007).
171. D. Chrobak, A. Chrobak, and R. Nowak, *Solid State Phenom.* 130, 213–218 (2007).
172. P. Valentini, W. W. Gerberich, and T. Dumitrica, *Phys. Rev. Lett.* 99, 175701 (2007).
173. J. M. Besson, J. P. Itie, A. Polian, G. Weill, J. L. Mansot, and J. Gonzales, *Phys. Rev. B* 44, 4214 (1991).
174. Z. C. Li, L. Liu, X. Wu, L. L. He, and Y. B. Xu, *Mater. Sci. Eng.* A337, 21–24 (2002).

175. M. Hebbache and M. Zemzemi, *Phys. Rev. B* 67, 233302 (2003).
176. J. E. Bradby, J. S. Williams, and M. V. Swain, *Phys. Rev. B* 67, 085205 (2003).
177. V. Domnich, Y. Gogotsi, and S. Dub, *Appl. Phys. Lett.* 76, 2214–2216 (2000).
178. W. C. D. Cheong and L. C. Zhang, *Nanotechnology* 11, 173 (2000).
179. J. Jang, M. J. Lance, S. Wen, T. Y. Tsui, and G. M. Pharr, *Acta Mater.* 53, 1759–1770 (2005).
180. I. Zarudi, L. C. Zhang, W. C. D. Cheong, and T. X. Yu, *Acta Mater.* 53, 4795 (2005).
181. D. E. Kim and S. I. Oh, *Nanotechnology* 17, 2259 (2006).
182. S. Izumi, S. Hara, T. Kumagai, and S. Sakai, *J. Crystal Growth* 274, 47 (2005).
183. C. Spinella, S. Lombardo, and F. Piriolo, *J. Appl. Phys.* 48, 5383 (1998).
184. M. Sakai, *J. Mater. Res.* 14, 3630–3639 (1999).
185. B. Rother and D. A. Dietrich, *Phys. Stat. Sol.* 142, 389–407 (1994).
186. B. Rother and D. A. Dietrich, *Surf. Coat. Technol.* 74–75, 614–617 (1995).
187. B. Rother, *J. Mater. Sci.* 30, 5394–5398 (1995).
188. B. Rother, *J. Mater. Sci.* 31, 6025–6028 (1996).
189. B. Rother, *Surf. Coat. Technol.* 86–87, 535–541 (1996).
190. B. Rother and H. A. Jehn, *Surf. Coat. Technol.* 85, 183–188 (1996).
191. B. Rother, T. Lunow, and G. Leonhardt, *Surf. Coat. Technol.* 71, 229–232 (1996).
192. M.V. Swain, *private communication*.
193. R. Nowak and M. Sakai, *Acta Metall. Mater.* 42, 2879–2891 (1994).
194. R. Nowak, I. Sakamoto, and S. Maruno, in "Third Euro-Ceramics" (F. Duran and J. F. Fernandez, Eds.), Vol. 2**,** pp. 571–576, 1993.
195. R. Nowak, T. Soga, and M. Umeno, *Thin Solid Films* 295, 193–198 (1997).
196 R. Nowak, M. Pessa, M. Suganuma, M. Leszczynski, I. Grzegory, S. Porowski, and F. Yoshida, *Appl. Phys. Lett.* 75, 2070–2072 (1999).
197 M. Fujikane, M. Leszczynski, S. Nagao, T. Nakayama, S. Yamanaka, K. Niihara, and R. Nowak, *J. Alloys Compd.* 450, 405–411 (2008).
198. F. Osmond and G. Cartaud, *Rev. Metall.* II, 811–819 (1905); M. H. Roth-Meyer, *Seance Acad. Sci.* 30, 906–913 (1950).
199. F. W. Daniels and C. G. Dunn, *Trans. Am. Soc. Met.* 41, 419–438 (1949).
200. C. A. Brookes, J. B. O'Neill, and A. W. Redfern, *Proc. R. Soc.* A322, 73–88 (1971).
201. J. Pospiech and J. Gryziecki, *Arch. Hutn.* XV, 267–283 (1970).
202. R. W. Armstrong and A. C. Raghuram, in "The Science of Hardness Testing and its Research Applications" (J. H. Westbrook and H. Conrad, Eds.), pp. 174–185, Metals Park, OH: American Society for Metals, 1973.
203. R. Nowak, *Acta Cryst.* A43, C-96 (1987).
204 R. Nowak, K. Ueno, and M. Kinoshita, in "Mechanical Behaviour of Materials – VI" (M. Jono and T. Inoue, Eds.), pp. 551–556, Pergamon Press, 1991.
205. R. Nowak, T. Sekino, S. Maruno, and K. Niihara, *Appl. Phys. Lett.* 68, 1063–1065 (1996).
206. R. Nowak, T. Manninen, C. L. Li, K. Heiskanen, V. Lindroos, S.-P. Hannula, T. Soga, and F. Yoshida, *J. JSME Intern. A* 46, 265–271 (2003).
207. M. Fujikane, D. Setoyama, S. Nagao, R. Nowak, and S. Yamanaka, *J. Alloys Compd.* 431 250–255 (2007); M. Fujikane, S. Nagao, X. Liu, D. Chrobak, S. Yamanaka, A. Lehto, and R. Nowak, *J. Alloys Compd.* 448, 293–297 (2008).
208. R. F. Cook, T. R. Dinger, and D. R. Clarke, *Appl. Phys. Lett.* 51, 454–456 (1987).
209. A. S. Raynes, S. W. Freiman, F. W. Gayle, and D. L. Kaiser, *J. Appl. Phys.* 70, 5254–5257 (1991).
210. N. Guclu, U. Kolemen, O. Uzun, and S. Celebi, *Physica C* 433**,** 115–122 (2005).
211. U. Kolemen, S. Celebi, Y. Yoshino, and A. Ozturk, *Physica C* 406, 20–26, (2004).
212. K. Kim, W. R. L. Lambrecht, and B. Segall, *Phys. Rev. B* 50, 1502–1508 (1994); H. Marchand, X. H. Wu, J. P. Ibbetson, P. T. Fini, P. Kazodoy, S. Keller, J. S. Speck, S. P. DenBaars, and U. K. Misra, *Appl. Phys. Lett.* 73, 747–749 (1998).
213. S. Nakamura, M. Senoh, S. Nagahama, N. Iwasa, and Y. Sugimoto, *Jpn. J. Appl. Phys.* 35, L74–L77 (1996).
214. M. Leszczynski, *Acta Phys. Polonica A* 92, 653–659 (1998).
215. K. Funato, F. Nakamura, S. Hashimoto, and M. Ikeda, *Jpn. J. Appl. Phys.* 37, 1023–1026 (1998).
216. V. Fiorentini, M. Methfessel, and M. Scheffler, *Phys. Rev. B* 47, 13353–13358 (1993); K. Miwa and A. Fukumoto, *Phys. Rev. B* **48**, 7897–7904 (1993); K. Shimada, T. Sota, K. Suzuki, and H. Okumura, *Jpn. J. Appl. Phys.* 37, L1421–L1423 (1998).
217. H. Tanaka, A. Nakadaira, and T. Matsuoka, in "Topical Workshop III–V Nitrides," Sept. 1995, Nagoya, Ext. Abstr. D-2.
218. S. O Kucheyev, J. S. Williams, and S. J. Pearton, *Mater. Sci. Eng. R* 33, 51–108 (2001).
219. C. Youtsey, L. T. Romano, and I. Adesia, *Appl. Phys. Lett.* 73, 797–799 (1998).
220. S. Nakamura, M. Senoh, S. Nagahama, N. Iwasa, T. Yamada, T. Matsushita, H. Kiyoku, et al., *Jpn. J. Appl. Phys*. 37, L1020–L1024 (1998).
221. M. D. Drory, J. W. Ager III, T. Suski, I. Grzegory, and S. Porowski, *Appl. Phys. Lett.* 69, 4044–4046 (1996).
222. G. Yu, H. Ishikawa, T. Egawa, T. Soga, J. Watanabe, T. Jimbo, and M. Umeno, *J. Cryst. Growth* 189/190, 701–707 (1998).
223. D. Tabor, *Nature* 273, 406–407 (1978).
224. H. O'Neil, *J. Inst. Metals* 30, 299–312 (1923).
225. H. Winchell, *Am. Miner.* 30, 583–589 (1945).
226. R. D. Arnell, *J. Phys. D: Appl. Phys.* 7, 1225–1232 (1974).
227. P. B. Hirsch, P. Pirouz, S. G. Roberts, and P. D. Warren, *Philos. Mag.* 52B, 759–784 (1986).
228. S. G. Roberts, P. D. Warren, and P. B. Hirsch, *Mater. Sci. Eng.* A105/106, 19–28 (1988); S. G. Roberts, *Philos. Mag.* 54B, 37–53 (1986).
229. A. Nadai, "Plasticity," New York: McGraw-Hill, 1931.
230. B. C. Wonsiewicz and G. Y. Chin, in "The Science of Hardness Testing and its Research Applications" (J. H. Westbrook and H. Conrad, Eds.), pp. 167–173, Metals Park, OH: American Society for Metals, 1973.
231. G. I. Taylor, *J. Inst. Metals* 62, 1121–1146 (1938).
232. G. R. Sawyer, P. M. Sargent, and T. F. Page, *J. Mater. Sci.* 15, 450–475 (1980).
233. W. Kollenberg, *J. Mater. Sci.* 23, 3321–3326 (1988).
234. C. Lu, Y. W. Mai, P. L. Tam, and Y. G. Shen, *Philos. Mag. Lett.* 87, 409–415 (2007).
235. K. P. D. Lagerlöf, A. H. Heuer, J. Castaing, J. P. Rivière, and T. E. Mitchell, *J. Am. Ceram. Soc.* 77, 585–597 (1994).
236. B. J. Pletka, T. E. Mitchell, and A. H. Heuer, *J. Am. Ceram. Soc.* 57, 388–393 (1974).
237. J. D. Snow and A. H. Heuer, *J. Am. Ceram. Soc.* 56, 153–157 (1973).
238. A. H. Heuer, *Philos. Mag.* 13, 379–393 (1966).
239. T. Geipel, K. P. D. Lagerlöf, P. Pirouz, and A. H. Heuer, *Acta Metall. Mater.* 42, 1367–1372 (1994).
240. P. Pirouz and P. M. Hazzledine, *Solid State Phenom.* 35–36, 183–216 (1994).
241. B. Y. Farber, S. Y. Yoon, K. P. D. Lagerlöf, and A. H. Heuer, *Z. Metallkd.* 84, 426–430 (1993).
242. B. Y. Farber, S. Y. Yoon, K. P. D Lagelöf, and A. H. Heuer, *Phys. Stat. Sol.* 137, 485–498 (1993).
243. K. P. D. Lagerlöf, in "Plastic Deformation of Ceramics" (R. C. Bradt, C. A. Brookes, and J. L. Ruotbort, Eds.), pp. 207–217, New York: Plenum Press, 1995
244. J. R. Willis, *J. Mech. Phys. Solids* 14, 163–76 (1966).
245. H. Leipholz, "Theory of Elasticity," pp. 272–287, Noordhoff Intern. Publ., 1974.
246. M. Dahan and J. Zarka, *Int. J. Solid Struct.* 13, 229–238 (1977).

247 J. C. Knight, A. J. Whitehead, and T. F. Page, *J. Mater. Sci.* 27, 3939–3952 (1992).

248. S. V. Hainsworth, T. Barlett, and T. F. Page, *Thin Solid Films* 236, 214–218 (1993).

249. B. D. Fabes, W. C. Oliver, R. A. McKee, and F. J. Walker, *J. Mater. Res.* 7, 3056–3064 (1992).

250. B. O. Johansson, U. Helmersson, M. K. Hibbs, and J. E. Sundgren, *J. Appl. Phys.* 58, 3104–3111(1985).

251. R. Nowak and C. L. Li, *Thin Solid Films* 305, 297–303 (1997).

252. S. Yamanaka, K. Hotehama, and H. Kawaji, *Nature* 392, 580–582 (1999).

253. R. Nowak and S. Maruno, *Mater. Sci. Eng. A* 202, 226–237 (1995).

254. R. Nowak, C. L. Li, and S. Maruno, *J. Mater. Res.* 12, 64–69 (1997).

255 W. D. Sproul, *Thin Solid Films* 118, 279–284 (1984).

256. H. A. Jehn, U. Kopacz, and S. Hofmann, *J. Vac. Sci. Technol.* A3, 2406–2410 (1985).

257 B. Jönsson and S. Hogmark, *Thin Solid Films* 114, 257–269 (1984).

258. G. P. Pells, "AERE Rep. R9359," Harwell, UK: Atomic Energy Research Establishment, 1979.

259. G. W. Arnold, G. B. Krefft, and C. B. Norris, *Appl. Phys. Lett.* 25, 540–552 (1974).

260. G. B. Krefft and E. P. EerNisse, *J. Appl. Phys.* 49, 2725–2730 (1978).

261. C. J. McHargue, H. Naramoto, B. R. Appleton, C. W. White, and J. M. Williams, *Proc. Mater. Res. Soc.* 7, 147–153 (1982).

262. C. J. McHargue and C. S. Yust, *J. Am. Ceram. Soc.* 67, 117–123 (1984).

263. H. Naramoto, C. W. White, J. M. Williams, C. J. McHargue, O. W. Holland, M. M. Abraham, and B. R. Appleton, *J. Appl. Phys.* 54, 683–698 (1983).

264. H. Naramoto, C. J. McHargue, C. W. White, J. M. Williams, O. W. Holland, M. M. Abraham, and B. R. Appleton, *Nucl. Instrum. Met. Physics Res.* 209–2106, 1159–1166 (1983).

265. G. C. Farlow, C. W. White, C. J. McHargue, and B. R. Appleton, *Proc. Mater. Res. Soc.* 27, 395–443 (1984).

266. G. C. Farlow, P. S. Sklad, C. W. White, and C. J. McHargue, *J. Mater. Res.* 5, 1502–1519 (1990).

267. C. J. McHargue, P. S. Sklad, C. W. White, J. C. McCallum, A. Perez, and G. Marest, *J. Mater. Res.* 6, 2160–2177 (1991).

268. C. J. McHargue, P. S. Sklad, C. W. White, and G. C. Farlow, *J. Mater. Res.* 8, 2145–2159 (1991).

269. T. Hioki, A. Itoh, M. Okubo, S. Noda, H. Doi, J. Kawamoto, and O. Kamigato, *J. Mater. Sci.* 21, 1321–1328 (1985).

270. T. Hioki, A. Itoh, S. Noda, H. Doi, J. Kawamoto, and O. Kamigato, *Nucl. Instrum. Met. Physics Res.* B7, 521–525 (1985).

271. C. J. McHargue, G. C. Farlow, C. W. White, J. M. Williams, B. R. Appleton, and H. Naramoto, *Mater. Sci. Eng.* 69, 123–127 (1985).

272. C. J. McHargue, *Nucl. Instrum. Met. Physics Res. B* 19–20, 797–804 (1987).

273. T. Hioki, A. Itoh, S. Noda, H. Doi, J. Kawamoto, and O. Kamigato, *Nucl. Instrum. Met. Physics Res. B* 39, 657–664 (1989).

274. C. J. McHargue, M. E. O'Hern, C. W. White, and M. B. Lewis, *Mater. Sci. Eng. A* 115, 361–367 (1989).

275. S. J. Bull and T. F. Page, *J. Mater. Sci.* 26, 3086–30106 (1991).

276. H. M. Pollock, D. Maugis, and M. Barquins, "ASTM Spec. Tech. Publ.," pp. 47–72, 1985.

277. J. B. Pethica, R. Hutchings, and W.C. Oliver, *Nucl. Instrum. Met. Physics Res.* 209–210, 995–1000 (1983).

278. R. Nowak, C. L. Li, and M. V. Swain, in "Modification of Ceramics and Semiconductors by Ion Bombardment" (R. Nowak et al., Eds.) (special issue, *Mater. Sci. Eng.* A253, 167–77 (1998)).

279. R. Nowak, "Preface to the Volume: Modification of Ceramics and Semiconductors by Ion Bombardment" (R. Nowak et al., Eds.), (special issue, *Mater. Sci. Eng.* A253 (1998)).

280 S. M. Myers, J. A. Knapp, D. Follstaedt, and M. T. Dugger, *J. Appl. Phys.* 83, 1256–1269 (1998).

281. S. M. Spearing, *Acta Mater.* 48, 179–196 (2000).

282 E. Mastropaolo, A. M. Gundlach, C. Fragkiadakis, P. B. Kirby, and R. Cheung, *Electron. Lett.* 43, 1467–1469 (2007).

283. R. R. Manory and G. Kimmel, *Surf. Coat. Technol.* 63, 85 (1994); L. J. Liu, D. K. Sood, R. R. Manory, and W. Zhou, *Surf. Coat. Technol.* 71, 159–166 (1995).

284. K. R. Padmanabhan, K. Saitoh, Y. Miyagawa, and S. Miyagawa, *Jpn. J. Appl. Phys.* 30, 796–801 (1991).

285. D. E. Alexander and G. S. Was, *Phys. Rev. B* 47, 2983–2994 (1993); H. A. Atwater, C. V. Thompson, and H. I. Smith, *J. Appl. Phys.* 64, 2337–2353 (1995).

286. S. P. Kaye, H. Kheyrandish, J. S. Colligon, and E. W. Roberts, *Thin Solid Films* 228, 252–256 (1993).

287. W. Li, X. He, and H. Li, *J. Appl. Phys.* 75, 2002–2006 (1994).

288. R. Nowak, Y, Horino, Y. Ando, and S. Maruno, *Appl. Phys. Lett.* 68, 3743–3745 (1996).

289. R. Nowak, J. Morgiel, and F. Yoshida, *Mater. Sci. Eng.* A253, 328–336 (1998).

290. R. Nowak, Y. Miyagawa, C. L. Li, S. Nakao, S. Maruno, and S. Miyagawa, *Mater. Lett.* 33, 31–36 (1997).

291. R. Nowak, F. Yoshida, J. Morgiel, and B. Major, *J. Appl. Phys.* 85, 841–852 (1999).

292. R. Nowak, F. Yoshida, Y. Miyagawa, and S. Miyagawa, *Nucl. Instrum. Met. Physics Res.* B148, 232–237 (1999).

293. A. J. Perry, R. R. Manory, R. Nowak, and D. Rafaja, *Vacuum* 49, 89–95 (1998).

294. R. R. Manory, C. L. Li, C. Fountzoulas, J. D. Demaree, J. K. Hirvonen, and R. Nowak, in "Modification of Ceramics and Semiconductors by Ion Bombardment" (R. Nowak et al., Eds.) (special issue, *Mater. Sci. Eng.* A253, 319–327 (1998)).

295. R. R. Manory, A. J. Perry, D. Rafaja, and R. Nowak, *Surf. Coat. Technol.* 114, 137–142 (1999).

296 B. O. Johansson, J. E. Sundgren, and U. Helmersson, *J. Appl. Phys.* 58, 3112–3117 (1985).

297. D. R. Kumar, R. K. Kumar, and P. K. Philip, *Scripta Mater.* 44, 2713–2719 (2001).

298. H. C. Ha, H. M. Chan, and H. F. Nied, *Acta Mater.* 49, 2453–2461 (2001).

299. S. Nagao, K. Nordlund, and R. Nowak, *Phys. Rev. B* 73, 144113 (2006) .

300. B. Cappella and G. Dietler, *Surf. Sci. Rep.* 34, 1–104 (1999).

301. A. C. Fischer-Cripps, "Nanoindentation," New York: Springer Science+Business Media, 2004.

302. J. Malzbender, J. M. J. den Toonder, A. R. Balkenende, and G. de With, *Mater. Sci. Eng. R* 36, 47–103 (2002).

Author Queries

AQ1: Please provide Table 7.
AQ2: Please update Ref. [23].
AQ3: Please update Ref. [38].
AQ4: Please list the references mentioned in the last column of Tables 4 and 5.
AQ: Please provide © info for figure 1–4, 6–16, 20, 21, 27–30, and 37.